



TECHNISCHE
UNIVERSITÄT
WIEN
Vienna | Austria



Empa

Materials Science and Technology

Master Thesis

Microscale 2D and 3D photolithography of cellulose nanocrystal composites

carried out for the purpose of obtaining the degree of Master of Science (MSc or Dipl.-Ing. or DI),
submitted at TU Wien, Faculty of Mechanical and Industrial Engineering, by

Samuel Stelzl

Mat.Nr.: 01525803

Dorfstrasse 15, 2191 Atzelsdorf, Austria

under the supervision of

Univ.Prof. Dr.rer.nat. Aleksandr Ovsianikov

Institute of Materials Science and Technology, E 308

and

Laszlo Petho and Dr. Johann Jakob Schwiedrzik

Laboratory for Mechanics of Materials & Nanostructures

EMPA Thun, Switzerland

Vienna, May 2020

This work was carried out at EMPA – Swiss Federal Laboratories for Materials Science and Technology in the Laboratory for Mechanics of Materials & Nanostructures

I confirm, that going to press of this thesis needs the confirmation of the examination committee.

Affidavit

I declare in lieu of oath, that I wrote this thesis and performed the associated research myself, using only literature cited in this volume. If text passages from sources are used literally, they are marked as such.

I confirm that this work is original and has not been submitted elsewhere for any examination, nor is it currently under consideration for a thesis elsewhere.

City and Date

Signature

Acknowledgements

1 Table of Contents

Table of Contents	I
Abstract	IV
Kurzfassung	V
List of Figures	VI
List of Tables	X
List of Abbreviations and Symbols	XII
1 Introduction	1
1.1 Motivation	1
1.2 Hierarchically architected metamaterials	2
1.3 Photopolymerization	3
1.4 2D Photolithography	4
1.5 Exposure methods in photolithography	6
1.5.1 Direct laser writing	6
1.5.2 2D maskless projection lithography	7
1.5.3 Two-photon-lithography	7
1.6 SU-8 photoresist	9
1.7 IP-S photoresist	11
1.8 Cellulose nanocrystals	11
1.9 Micromechanics	13
2 Experimental procedure	15
2.1 Materials	16
2.2 General photolithography steps	17
2.2.1 Removal of the adsorbed water	17
2.2.2 Spin coating	17
2.2.3 Soft baking (SB)	18
2.2.4 Exposure	19
2.2.5 Post exposure baking (PEB)	20
2.2.6 Development	21
	I

2.2.7	Microscopy	21
2.2.8	Mechanical testing	22
2.3	Preparation of the cellulose nanocrystal (CNC)-photoresist-mixtures	23
2.3.1	SU-8/CNC/Acetone with 5.0 wt% CNC	23
2.3.2	SU-8/CNC/GBL with 4.5 wt% CNC	24
2.3.3	IP-S/CNC/GBL	25
2.3.4	IP-S/CNC/HEMA	26
2.4	SU-8 2D Lithography	27
2.4.1	Exposure with the direct laser writer	27
2.4.2	Exposure with the maskless projection system	28
2.5	SU-8/CNC composites 2D Lithography	29
2.5.1	SU-8/CNC/Acetone with 5.0 wt% CNC	30
2.5.2	SU-8/CNC/GBL with 4.5 wt% CNC	30
2.6	IP-S 2D Lithography	31
2.7	IP-S/CNC composites 2D Lithography	32
2.7.1	IP-S/CNC/GBL with 4.5 wt% CNC	32
2.7.2	IP-S/CNC/HEMA	33
2.8	SU-8 3D Lithography	33
2.9	SU-8/CNC composites 3D Lithography	35
2.10	IP-S 3D Lithography	36
2.11	IP-S/CNC composites 3D Lithography	36
2.11.1	IP-S/CNC/GBL with 4.5 wt% CNC	36
2.11.2	IP-S/CNC/GBL with 13.0 wt% CNC	37
2.11.3	IP-S/CNC/HEMA	38
3	Results and Discussion	40
3.1	SU-8 2D Lithography	40
3.2	SU-8/CNC composite 2D Lithography	45
3.3	IP-S 2D Lithography	46
3.4	IP-S/CNC composite 2D Lithography	48
3.5	SU-8 3D Lithography	49
3.6	SU-8/CNC composite 3D Lithography	52

3.7	IP-S 3D Lithography	55
3.8	IP-S/CNC composite 3D Lithography	62
3.8.1	IP-S/CNC/GBL with 4.5 wt% CNC	62
3.8.2	IP-S/CNC/GBL with 13.0 wt% CNC	70
3.8.3	IP-S/CNC/HEMA	73
3.9	General discussion	75
3.9.1	Process quality	75
3.9.2	Mechanical properties	76
3.9.3	Process parameters	83
4	Conclusions	84
5	References	86

Abstract

Photolithography is a key technique for modern technologies like microelectronics and micro electromechanical systems (MEMS). With the development of two-photon-lithography, a sub-micrometer resolution 3D printing method, an important new tool for Materials Scientists was created. In this thesis, IP-S and SU-8, two commercially available photoresists, were used as polymer matrices for cellulose nanocrystal reinforced composites. Due to the abundance of cellulose and the outstanding material properties of nanocellulose, these anisotropic particles are a promising reinforcement filler. 2D and 3D photolithography was performed with varying compositions to print different structures for micromechanical testing of the composites. The best results were achieved with an IP-S system, in which the nanocellulose was introduced with γ -butyrolactone. The impressive resolution in the lower one-digit micrometer range enabled the printing of cellular structures and tensile specimens for further mechanical investigation. It was found that the mechanical properties of this system increase remarkably with the CNC content and decrease with the laser power used for 3D printing.

Kurzfassung

Photolithographie ist eine der Schlüsseltechnologien in der Herstellung von Mikroelektronik und mikro elektromechanischen Systemen (MEMS) und hat dadurch maßgeblich zur Entwicklung unserer modernen Gesellschaft beigetragen. Durch die Entwicklung der Zwei-Photonen-Lithographie, die Auflösungen < 100 nm ermöglicht, wurde der Werkzeugkasten der Wissenschaft um ein wertvolles Gerät erweitert. Im Zuge dieser Diplomarbeit wurden zwei kommerziell erhältliche Photolacke (IP-S und SU-8) als Basiskomponente verwendet, die mit nanokristalliner Zellulose verstärkt wurden. Da Nanozellulose aus verschiedensten Zellulosequellen gewonnen werden kann und beeindruckende mechanische Eigenschaften aufweist, ist sie ein nachhaltig gewinnbares, vielversprechendes Füllmaterial. Mit den unterschiedlichen Mischungen aus Nanozellulose und Photolack wurde durch 2D und 3D Photolithographie verschiedenste Strukturen für mechanische Tests gedruckt. Dabei wurden die besten Resultate mit einer Mischung erzielt, die aus IP-S als Basismaterial besteht, in das mithilfe von γ -Butyrolacton Nanozellulose eingebracht wurde. Die beeindruckende Auflösung im unteren, einstelligen Mikrometerbereich ermöglichte das Drucken von komplexeren Architekturen wie Zugproben und zelluläre Strukturen, die zur weiteren Untersuchung des mechanischen Verhaltens verwendet wurden. Die Tests an diesem System ergaben, dass die mechanischen Eigenschaften mit dem Zellulosegehalt stark ansteigen, jedoch mit der Laserpower, die beim Drucken verwendet wird, abnehmen.

List of Figures

Figure 1: Ashby chart plotting density vs Young's modulus of different classes of materials; Chart created using CES EduPack 2019, ANSYS Granta © 2020 Granta Design	2
Figure 2: Mechanism of radical photopolymerization	3
Figure 3: UV-radiation induced creation of a free radical by benzophenone	4
Figure 4: Process flow for processing a negative tone photoresist	6
Figure 5: Sketch of the Nanoscribe Photonic Professional GT system (Nanoscribe) [30]	9
Figure 6: Chemical structure of the monomer SU-8	10
Figure 7: Molecular structure of cellulose	11
Figure 8: Summary of all CNC composites manufactured and processed in this thesis	16
Figure 9: Different spin coaters used in this thesis: a, SAWATEC SM-180-BT; b, POLOS MCD200	17
Figure 10: Spin coating recipes with different spinning speeds in the dispersing step	18
Figure 11: a, Hotplate used in this thesis: SAWATEC HP-401; b, - d, Soft baking recipes used in this thesis with different durations at 120 °C	19
Figure 12: Lithography systems used in this thesis: a, HEIDELBERG INSTRUMENTS μ PG 101; b, INTELLIGENT MICRO PATTERNING SF-100; c, Nanoscribe Photonic Professional GT system	20
Figure 13: Post exposure baking recipe for photoresists containing SU-8	21
Figure 14: In-situ micro-indenter (Alemnis) in a Hitachi TM3030 Plus SEM	22
Figure 15: Setup for tensile testing (Alemnis)	23
Figure 16: Pattern for the dose and resolution test for SU-8 on the direct laser writer, dimensions about 3930x2100 μ m	28
Figure 17: Pattern for the dose and resolution test for SU-8 on the maskless projection system, dimensions about 12.3x9.2 mm	29
Figure 18: Pattern for the 2D lithography with CNC-photoresist mixtures on the maskless projection system, dimensions about 12.3x9.2 mm	30
Figure 19: Pattern for the dose and resolution test for IP-S on the maskless projection system, dimensions about 12.3x9.2 mm	32
Figure 20: Spin coating recipe for the application of TI Prime Adhesion Promoter	34
Figure 21: SU-8 dose and resolution test with the maskless projection system, 7.3 s	40
	VI

Figure 22: Section of the dose and resolution test on the direct laser printer; section with printing parameters of 60 % laser power (about 2.2 mW/cm ²) and defocus +15	41
Figure 23: SEM images of the structures for mechanical testing, SU-8 2D photolithography; a, hexagon with 5 μm wall width; b, hexagon with 5 μm wall width, 45° tilted; c, honeycombs with 5 μm wall width; d, honeycombs with 5 μm wall width, 45° tilted; e, pillar with 13 μm diameter; f, pillar with 13 μm diameter, 45° tilted	42
Figure 24: Stress-strain-curves of the micro compressions of: a, pillars, b, hexagons, c, honeycombs	43
Figure 25: SU-8/CNC composite structures exposed with the maskless projection system	46
Figure 26: IP-S structures exposed with the maskless projection system, substrates: a, and b, glass wafer; c, silicon wafer	47
Figure 27: Structures made of IP-S/CNC/GBL with 4.5 wt% CNC exposed with the maskless projection system, substrates: a, and b, glass wafer; c, silicon wafer	49
Figure 28: SU-8 pillars with 13 μm in diameter and 40 μm in height printed with different laser power: a, 12 mW, b, 15 mW, c, 20 mW, d, 25.5 mW	50
Figure 29: Stress-strain-curves of SU-8 pillar compressions, pillars printed with different laser power	52
Figure 30: Pillars of SU-8/CNC/GBL mixture printed with 13 μm in diameter and 40 μm in height, printed with different laser power: a, 14 mW b, 20 mW; c, 23.5 mW	53
Figure 31: Stress-strain-curves of SU-8/CNC/GBL and neat SU-8 pillar compressions, pillars printed with different laser power	54
Figure 32: Formation of a diol out of an epoxy group and water	55
Figure 33: Hexagons printed with SU-8/CNC/GBL mixture with a wall thickness of 4 μm; a, top view; b, 45° tilted	55
Figure 34: IP-S pillars printed with 13 μm in diameter and 40 μm in height, printed with different laser power: a, 12.5 mW; b, 17.5 mW; c, 22.5 mW; d, 27.5 mW	56
Figure 35: Stress-strain-curves of IP-S pillar compressions, pillars printed with different laser power	57
Figure 36: IP-S cellular structures, a, and b, before compression, c, and d, after compression	59
Figure 37: Stress-strain-curve of the IP-S cellular structures	60
Figure 38: IP-S tensile samples, printed with different laser power: a, 15 mW, b, 30 mW	61
	VII

Figure 39: Stress-strain-curves of the IP-S tensile samples, printed with different laser power	62
Figure 40: Pillars of 13 μm in diameter and 40 μm in height, printed with the IP-S/CNC/GBL mixture with 4.5 wt% CNC with different laser power: a, 12.5 mW, b, 17.5 mW, c, 22.5 mW, d, 27.5 mW	63
Figure 41: Stress-strain-curves of the IP-S/CNC/GBL pillar compressions; 4.5 wt% CNC; printed with different laser power	64
Figure 42: Hexagons printed with the IP-S/CNC/GBL mixture with 4.5 wt% CNC; the height is about 40 μm , the true wall width is: a, and b, 2.7 μm ; c, and d, 7.0 μm ; printed with 25 mW laser power	65
Figure 43: Cellular structures printed with the IP-S/CNC/GBL mixture with 4.5 wt% CNC, a, and b, before compression, c, and d, after compression	66
Figure 44: Stress-strain-curve of the IP-S/CNC/GBL cellular structure, 4.5 wt% CNC	67
Figure 45: Tensile samples printed with the IP-S/CNC/GBL mixture with 4.5 wt% CNC and with different laser power: a, 15 mW; b, 20 mW; c, 25 mW, d, 30 mW	68
Figure 46: Stress-strain-curve of 4.5 wt% IP-S/CNC/GBL mixture tensile sample	69
Figure 47: Pillars of 13 μm in diameter and 40 μm in height, printed with the IP-S/CNC/GBL mixture with 13.0 wt% CNC with different laser power: a, 12.5 mW, b, 17.5 mW, c, 22.5 mW, d, 27.5 mW	70
Figure 48: Stress-strain-curves of IP-S/CNC/GBL pillar compressions; 13.0 wt% CNC; printed with different laser power	71
Figure 49: Hexagons printed with the IP-S/CNC/GBL mixture with 13.0 wt% CNC; the height is about 40 μm , the true wall width is: a, and b, 4.2 μm ; c, and d, 10.6 μm ; printed with 25 mW laser power	72
Figure 50: Tensile samples printed with the IP-S/CNC/GBL mixture with 13.0 wt% CNC and with different laser power: a, 15 mW; b, 20 mW; c, 25 mW, d, 30 mW	73
Figure 51: structures printed with the IP-S/CNC/HEMA mixture, true dimensions of the structures: a, and b, 15.5 μm in diameter, 24 μm in height; c, and d, wall thickness of 12.5 μm , height of 33 μm	74
Figure 52: Yield stresses of the different resists and mixtures gained by pillar compression, error bar is calculated for a confidence level of 95 %	78

Figure 53: Young's moduli of the different resists and mixtures gained by pillar compression, error bar is calculated for a confidence level of 95 %	78
Figure 54: Hardening moduli of the different resists and mixtures gained by pillar compression, error bar is calculated for a confidence level of 95 %	79
Figure 55: Stress-strain-curves of pillar compression of neat IP-S and the IP-S/CNC/GBL composites; a, neat IP-S; b, 4.5 wt% CNC; c, 13.0 wt% CNC	80
Figure 56: Dependency of the yield stress on laser power and CNC content by multiple linear regression	81
Figure 57: Dependency of the Young's modulus on laser power and CNC content by multiple linear regression	82

List of Tables

Table 1: Terminology to describe the different types of nanocellulose [49]	12
Table 2: Summary of the dimensions of all printed structures, in μm	15
Table 3: Materials, their purity and supplier used in this thesis	16
Table 4: Data of the determination of the CNC content in acetone	24
Table 5: Data of the determination of the CNC content in acetone after concentrating	24
Table 6: Data of the determination of the CNC content in GBL after solvent exchange	25
Table 7: Data of the determination of the CNC content in GBL after solvent exchange	26
Table 8: Parameters for the dose and resolution test for SU-8 on the direct laser writer	28
Table 9: Real dimensions of the SU-8 structures printed with the direct laser writer, measured on the SEM, in μm	43
Table 10: Data from the compression tests of the SU-8 structures, the dispersion is given for a confidence level of 95 %	45
Table 11: Dimensions and mechanical properties of the SU-8 micropillars printed with different laser power; the dispersion is given for a confidence level of 95 %	51
Table 12: Dimensions and mechanical properties of the SU-8/CNC/GBL micropillars printed with different laser power; the dispersion is given for a confidence level of 95 %	54
Table 13: Dimensions and mechanical properties of the IP-S micropillars printed with different laser power; the dispersion is given for a confidence level of 95 %	57
Table 14: Dimensions and mechanical properties of the IP-S cellular structures; the dispersion is given for a confidence level of 95 %	60
Table 15: Dimensions and mechanical properties of the IP-S tensile samples printed with different laser power	61
Table 16: Dimensions and mechanical properties of the IP-S/CNC micropillars with 4.5 wt% CNC printed with different laser power; the dispersion is given for a confidence level of 95 %	63
Table 17: Theoretical and true wall width of the hexagons in Figure 42	65
Table 18: Dimensions and mechanical properties of the IP-S/CNC/GBL cellular structures with 4.5 wt% CNC; the dispersion is given for a confidence level of 95 %	66
Table 19: Dimensions and mechanical properties of the IP-S/CNC tensile samples with 4.5 wt% CNC; the dispersion is given for a confidence level of 95 %	68
	X

Table 20: Dimensions and mechanical properties of the IP-S/CNC micropillars with 13.0 wt% CNC printed with different laser power; the dispersion is given for a confidence level of 95 %	71
Table 21: Theoretical and true wall width of the hexagons in Figure 49	72
Table 22: Results of the ANOVA for the dependency of the yield stress on the laser power and the CNC content	80
Table 23: Results of the ANOVA for the dependency of the Young's modulus on the laser power and the CNC content	81
Table 24: Summary of the laser powers, which the best results were obtained with	83

List of Abbreviations and Symbols

CNC	Cellulose nanocrystals
CNF	Cellulose nanofibrils
DLW	Direct laser writer
GBL.....	γ -Butyrolacton
HEMA.....	Hydroxyethylmethacrylat
IP-S.....	IP-S photoresist
MEMS	Microelectromechanical systems
MPS.....	Maskless projection system
PEB.....	Post exposure baking
PGMEA.....	1-methoxy-2-propanyl acetate (propylene glycol methyl ether acetate)
RCF.....	Relative centrifugal force
RPM	Revolutions per minute
SB.....	Soft baking
SEM.....	Scanning electron microscope
SU-8	SU-8 photoresist
τ	Relaxation time
ΔE	Energy
\hbar	Reduced Planck's constant

1 Introduction

In this chapter the motivation of this work is presented as well as an introduction on photolithography and two-photon lithography. Information on SU-8 and IP-S photoresist and on photopolymerization in general is given and furthermore, cellulose nanocrystals, metamaterials and micromechanics are discussed. The experimental procedure was performed in a Class 10.000/ISO 7 clean room, which is constant at 21.0 ± 1.0 °C and at 45 ± 5 % RH.

1.1 Motivation

Due to the permanent demand for improvement in mechanical robustness and reduction of manufacturing costs, new materials with structural hierarchy have been investigated intensively in recent years. And because of the great progress in additive manufacturing, these structures can be processed quite easily with sub-micron resolution[1]–[3].

Natural hierarchically structured materials like bones or wood are known to have a very high resilience against extreme mechanical environments. It seems that this robustness is caused by the mechanical network of these materials which contains multiple levels of hierarchy[4]–[6]. In larger dimensions, mankind has already been using this phenomenon for a long time. Some examples are the Eiffel Tower, construction cranes and building scaffolding. It was shown, that hierarchically architected materials have very impressive features, like low or negative coefficients of thermal expansion[7], [8], high stiffness-to-weight ratios[9]–[12] or negative Poisson`s ratio[13], [14].

Another method to modify the properties of materials is to add a filler. Due to its great mechanical properties and its abundancy, nanocellulose has attracted very much interest[15]–[17]. These small cellulose rods are obtained from different plant material like wood. Therefore, it is an abundant and renewable material. Another advantage of cellulose is the possibility to modify its properties by chemically modifying the cellulose molecules or by using different kinds of nanocellulose[18].

1.2 Hierarchically architected metamaterials

If one wants to select a material with certain properties for a certain application, the so called Ashby plots are a good choice to get an overview which materials could be possible. These plots display two properties of materials or classes of materials, e.g. density versus Young's modulus (Figure 1). One of the big goals in material's science is to fill the areas where no materials are yet, e.g. materials with a low density and a high Young's modulus.

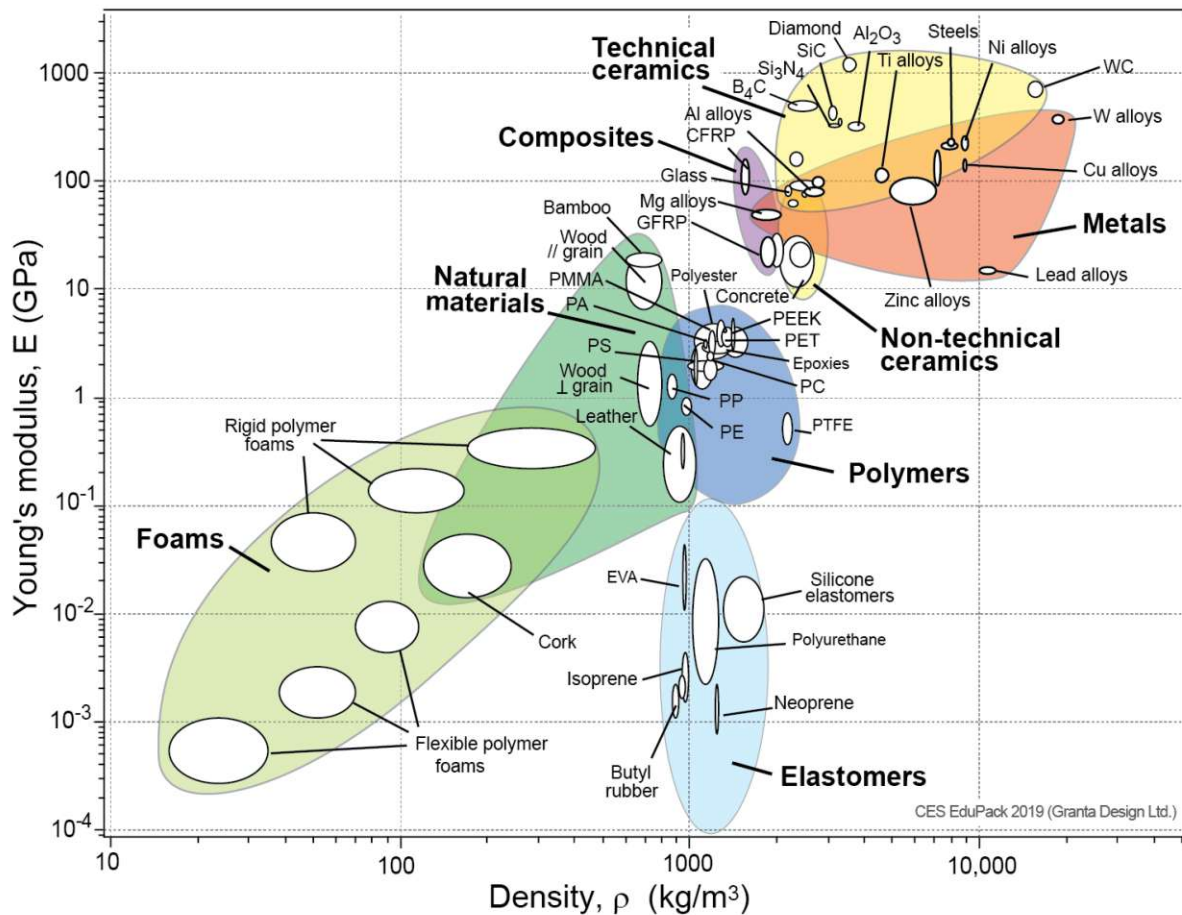


Figure 1: Ashby chart plotting density vs Young's modulus of different classes of materials;
Chart created using CES EduPack 2019, ANSYS Granta © 2020 Granta Design

One method of approaching these areas is the idea of creating materials with hierarchical levels. This kind of structure is found in many natural materials, like wood[6] and bone[5]. These materials are very resilient against extreme mechanical environments. Therefore, hierarchical materials have been investigated for many years and researchers have already gained a huge amount of knowledge about their behaviour, but there are still some aspects unknown[19].

The knowledge about structural hierarchy combined with modern techniques like simulations of materials behaviour and sub-micron resolution 3D printing resulted in many outstanding materials properties. Some of these impressive properties are a negative Poisson's ratio[14], high specific strength[9] and specific stiffness[20].

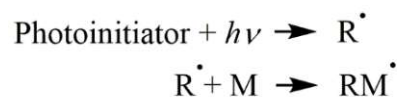
1.3 Photopolymerization

Photopolymerization is a kind of polymerization, which uses the absorption of radiation (photons) with wavelengths in the visible or UV spectrum to start the polymerization. Commonly a photoinitiator is necessary to start the chain reaction. The photoinitiator is a molecule, which absorbs the energy of the radiation and creates reactive species like free radicals, cations or anions, depending on the polymerization mechanism.

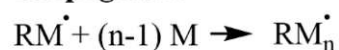
The process of photopolymerization explained by the example of a radical polymerization contains three main parts (Figure 2):

- **Initiation:** The photoinitiator absorbs radiation and creates a free radical, which reacts with a monomer molecule to another free radical.
- **Propagation:** This reactive species reacts with another monomer molecule and thereby creates a new free radical. This step is repeated again and again.
- **Termination:** If two radicals react with each other, the chain reaction is stopped (combination). The reaction is also stopped, if an atom (typically hydrogen) is transferred from one radical chain to another (disproportionation).

Initiation



Propagation



Termination

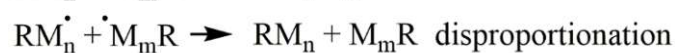


Figure 2: Mechanism of radical photopolymerization

To choose a suitable photoinitiator for a specific issue, not only the type of polymerization mechanism is determinative. One also has to consider the absorbance spectrum of the photoinitiators to ensure that the photoinitiator efficiently absorbs the radiation which is emitted by the photon source one wants to use for polymerization. A typical photoinitiator for radical photopolymerization and its creation of a free radical are shown in Figure 3.

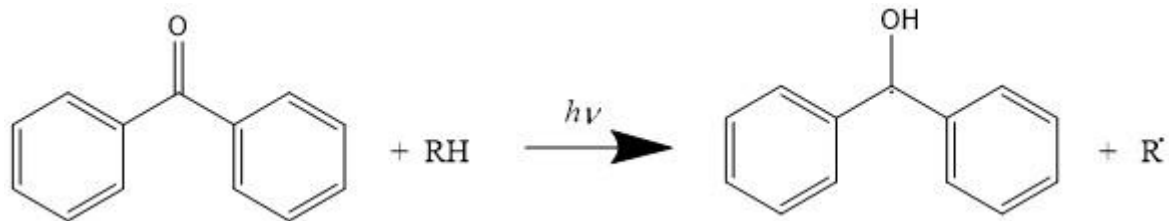


Figure 3: UV-radiation induced creation of a free radical by benzophenone

1.4 2D Photolithography

Photolithography is a process, which is used to pattern a photosensitive film on a substrate. It uses photons to transfer geometrical pattern to the photosensitive resist on the substrate. If a negative tone photoresist is used, like in this thesis, the exposed parts of the film polymerize and stay on the wafer and the unpolymerized parts can be dissolved in the development step (Figure 4). This pattern can be used, e.g. for introducing material[21] or to selectively etch the substrate at certain areas[22].

The basic process begins with the cleaning of the substrate. The substrate used in this thesis was either a single crystal silicon wafer in $\langle 1\ 0\ 0 \rangle$ orientation (100 mm in diameter and 500 μm in height) or a glass slide (30 mm in diameter and $170 \pm 10\ \mu\text{m}$ in height). This can be performed with different solvents and also with an oxygen plasma. The substrate is heated to about 150-160 $^{\circ}\text{C}$ for several minutes, to remove adsorbed water from the surface to improve the adhesion. After this, the wafer gets coated with the photoresist by spin coating. With the rotation speed the thickness of the film can be controlled. All the excess material is removed over the edges of the substrate by the centrifugal force. Thus, a quite homogeneous film is created. To further uniform the thickness and to evaporate the solvents of the photoresist, a prebaking or soft baking step has to be performed. As the common 2D photolithography resists are solids and are only dissolved for processing, the resist gets solid again in this step.

The temperature and duration of this step varies with the solvent and the amount of it in the resist[23].

After the soft baking, the resist is exposed to light, mostly UV light. In this step chemical changes occur, in which a photoinitiator reacts as a result of the interaction with the light. In dependence on which kind of resist it is, a negative or a positive photoresist, different reactions are happening. In the case of a negative tone resist the exposed parts will polymerize, in the case of a positive tone resist the exposed parts will react in a way, so that they get soluble in the developer. In 2D photolithography the exposure dose is adjusted by time, because the intensity is fixed. The thicker the photosensitive film is, the longer the exposure should last. Depending on the resist used, crosslinking can happen during the exposure. If crosslinking does not happen during the exposure, a post exposure baking step has to be performed. Thereby a high degree of polymerization is ensured.

The next step is the development, where the substrates are treated with a developer. The developer is a solvent, which dissolves the unpolymerized parts faster than the polymer. The developer also reacts with the polymerized part, e.g. swelling of the polymer. Therefore, the substrate should only stay as long as necessary in the developer. After the development, the substrates are rinsed with another solvent to stop the development step. Finally, a hard baking step is performed, depending on which photoresist is used. This process cures the polymer so that it gets more durable.

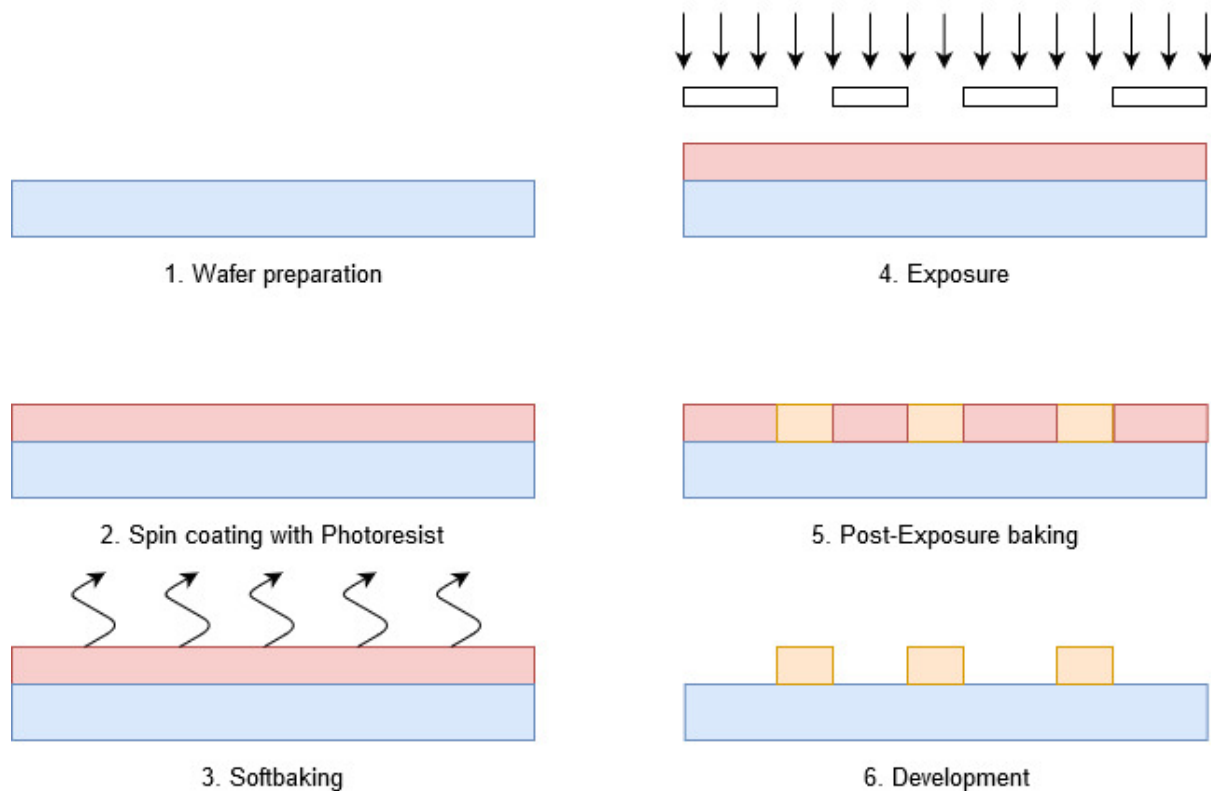


Figure 4: Process flow for processing a negative tone photoresist

1.5 Exposure methods in photolithography

There are many different methods to expose the photoresist. In this chapter the methods used in this thesis are elucidated.

1.5.1 Direct laser writing

Direct laser writing is a 2D maskless exposure method. In this method a laser head is scanning the wafer line by line. By turning the laser on and off, a pattern is transferred onto the substrate. In contrast to two-photon-polymerization[24] the energy of one photon emitted by these lasers is high enough to start a chemical reaction in the resist, which means, that the wavelength of these is in the near UV region.

One big advantage of this method is, that no photomask is needed. This is very interesting for research and for prototype processes, as the process of manufacturing the photomask and the alignment of it is eliminated. Another advantage is the resolution in the lower one-digit micrometre scale.

Disadvantages are e.g. the very sensitive optical parts and the relatively long duration of the patterning process, especially if large structures are printed. To print a 2x2 cm pillar array with 50x50 pillars, it can take up to far more than one hour, depending on the diameter of the pillars, the thickness of the resist and depending on which resist is used.

1.5.2 2D maskless projection lithography

2D maskless projection lithography is a very fast and versatile patterning method. This method uses MEMS mirrors to pattern the whole structure at the same time onto the substrate. The wavelength of the radiation in this method is in the same range as in the direct laser writing process, which means, that a single photon has enough energy to start a chemical reaction.

In this method, like in the direct laser writing process, no photomask is needed. Another advantage is that the exposure process is very fast, as the whole structure is patterned at the same time. The maximum size of the pattern is about 12.3x9.2 mm and its exposure takes from seconds to a few minutes, depending on the thickness of the resist and which resist is used, but independent from the exposed pattern.

The biggest disadvantage of this patterning method is the low resolution compared to the direct laser writing or the two-photon-lithography. This is a result of the fact that the MEMS mirrors cannot be produced as small as they would have to be to achieve resolutions in the sub-micrometre scale. The best resolution achieved with the machine used in this thesis was 35-40 μm .

1.5.3 Two-photon-lithography

Two-photon-lithography is a relatively new technique of 3D printing. The basic principle in this nanoscale lithography is the two-photon-absorption (TPA):

If a photon interacts with an electron, the electron is raised to a virtual excited state. This state only exists for a very short time and it relaxes after this time. As the energy of electrons can only attain discrete values, this virtual state is quantum mechanically forbidden. However, the lifetime of this virtual state is so short, that it does not violate the time-energy uncertainty relation (given in Eq. (1), τ is the lifetime of the excited state, ΔE the energy of the photon and \hbar is the reduced Planck's constant)[25]. If a second photon interacts with the same electron in this period of time, it can absorb its energy too, so that the electron absorbed the energy of two photons. As this time slot is extremely short, the photons almost have to interact at the

same time with the electron. To achieve such a high photon density a femtosecond (fs) laser has to be used. The common lasers used are in the near infrared spectrum, so that the energy of two photons with that radiation is equal in energy with a single UV photon, because most photoresists are made for UV lithography[26].

$$\tau\Delta E \sim \frac{\hbar}{2} \quad (1)$$

The needed photon density is so high, that it is only reached in the focal spot of the laser. This means, that the resolution of this lithography technique is around the dimensions of the focal spot [27], [28](down to 40 nm in lateral or axial feature size, depending on the lithography method[29]), which is much better than of common 2D lithography techniques. Another advantage of this process is, that a real 3D structure can be printed inside a film of monomer without altering the other material around the focal spot. However, two-photon-lithography is a quite slow method compared to other photolithography methods like mask printing. This means, that it is not very suitable for large structure fabrications or large scale productions.

With the Nanoscribe Photonic Professional GT system (Nanoscribe) used in this thesis, 2-photon-lithography can be performed in two different setups:

- Immersion Lithography (Figure 5, upper right side): In this setup the photosensitive material is on top of a transparent wafer, e.g. a glass slide. On the bottom side of the wafer, a drop of immersion oil is placed. Then the wafer is put into the 2-photon-lithography system, so that the objective dips into the oil. This means, that the laser beam goes through the oil and the glass before it reaches the photoresist. Therefore, the oil and the substrate must have almost the same refractive index, otherwise scattering effects can influence the resolution.

The advantage of this setup is, that the expensive objectives do not get in contact with the photoresist. Therefore, different photosensitive materials can be exposed, which should not get in contact with the objectives, e.g. corrosive or hardly soluble substances. One disadvantage is the decreased resolution compared to dip-in lithography, which is due to scattering effects, as the laser beam has to go through the oil and the glass before entering the photoresist. Another one is the limited printing

height. As the working distance of an objective is a constant, the maximum height can be deduced from the working distance and the thickness of the substrate.

- Dip-in Lithography (Figure 5, lower right side): In this setup, the photoresist is on the bottom side of the substrates, which does not have to be transparent in contrast to the substrates for immersion lithography. The substrate is put in the 2-photon-lithography system with the photoresist on the bottom. Then the objective dips into the photosensitive material.

The advantages of this setup are the outstanding resolution and the printing height, which can be up to several centimetres. The big disadvantage is the limitation in photoresists, as the objective dips into it. Therefore, it must not be harmful to the objective and it must be soluble in solvents which do not harm the objective.

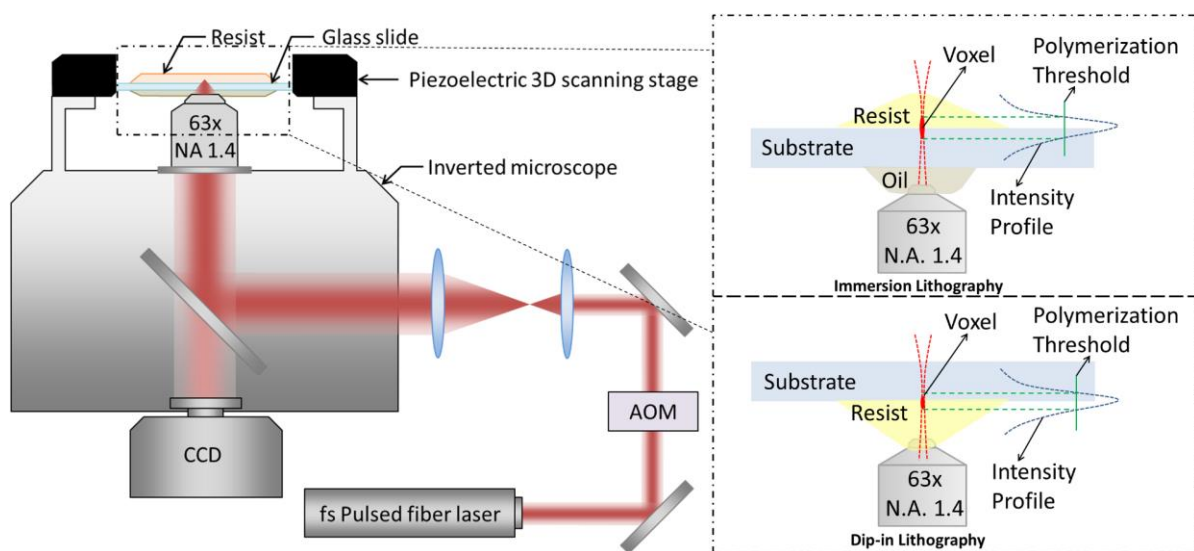


Figure 5: Sketch of the Nanoscribe Photonic Professional GT system (Nanoscribe) [30]

1.6 SU-8 photoresist

SU-8 is an epoxy-based, negative tone photoresist, which is sensitive to ultraviolet light [31]–[34], X-rays [35] and to high-energy particles like electrons [36]. Negative tone means, that the exposed parts of the resist polymerize and will not dissolve during development, whereas the unexposed parts will be removed. A typical developer for SU-8 is 1-methoxy-2-propanol acetate, short PGMEA. The SU-8 itself is a solid, for processing it is dissolved in solvents like γ -butyrolactone, short GBL. With the amount of GBL in the resist, the viscosity and thereby the

processability is controlled. The higher the viscosity is, the thicker are the films which can be created.

SU-8 is a molecule with four bisphenol-A-bisepoxyether groups (Figure 6) [37]. During exposition, in the exposed areas the photoinitiator becomes a strong Lewis acid, which starts a cationic polymerization [38]. To promote the polymerization, a curing step after the exposure is performed, which is called post exposure baking.

The absorbance of radiation is very low for radiation above 400 nm and increases drastically below 350 – 360 nm, which makes it transparent to visible light and very suitable for UV lithography [39]. Typical values for the Young's modulus of SU-8 are 2-3 GPa under bending [40] and 4 GPa in tensile testing [34], the ultimate strength is in the area of 119 – 132 MPa for different SU-8 photoresists [41]. As there are many different SU-8 photoresists commercially available, studies on mechanical and optical properties were not performed on all of them. The values shown above are the results of experiments with other SU-8 photoresists with different manufacturing protocols, which means that the properties of the SU-8 used in this thesis can differ.

With SU-8, a high aspect ratio, which is the ratio of height to width of the patterned structures, can be achieved [42]. If the process is optimized well, the structures are very straight and smooth, so that high pillars and deep holes can be produced. As SU-8 is an epoxy-based resin, it is comparatively stiff and chemically resistant. Due to these properties it is used structurally, like in MEMS [32]–[34], and also in larger scales, like in methanol fuel cells [43].

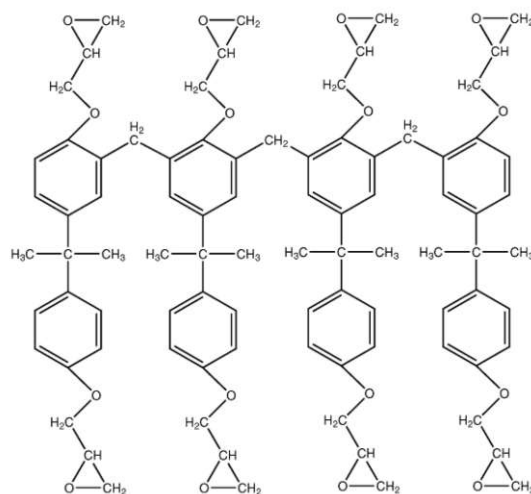


Figure 6: Chemical structure of the monomer SU-8

1.7 IP-S photoresist

Unfortunately, there is not much information available about IP-S. It is a methacrylate-based, negative tone photoresist, which is cured by free radical polymerization. IP-S is manufactured by Nanoscribe and is made specifically for two-photon-polymerization. A typical developer for IP-S is PGMEA, like for SU-8. Due to the change in refractive index of the IP-S during polymerization, it is possible to recognise the polymerization process during printing. The refractive index changes from 1.486 (liquid) to 1.515 (polymerized) at 589 nm and 20 °C. The Young's modulus is about 5 GPa, the 2-photon-polymerization transmittance is $\geq 95\%$ from 633 nm to 2.4 μm [44].

1.8 Cellulose nanocrystals

Cellulose is a fascinating biopolymer. It is the most abundant renewable polymer resource on earth today. It is a polysaccharide consisting of a linear chain of hundreds to thousands of β -1,4-connected glucose units (Figure 7). Cellulose is used in many different ways. Beside lignin it is the main components of wood, and cotton is almost pure cellulose. For many applications the cellulose has to be isolated and modified afterwards. Various kinds of cellulose derivatives are known and commonly used in different fields, e.g. carboxymethyl cellulose (E 466) as a thickening additive in the food industry, cellulose nitrate as an explosive or as an additive in glues, or cellulose acetate as foils or membranes. Cellulose is insoluble in almost all solvents, but if it is treated with acids or bases, the cellulose can be degraded.

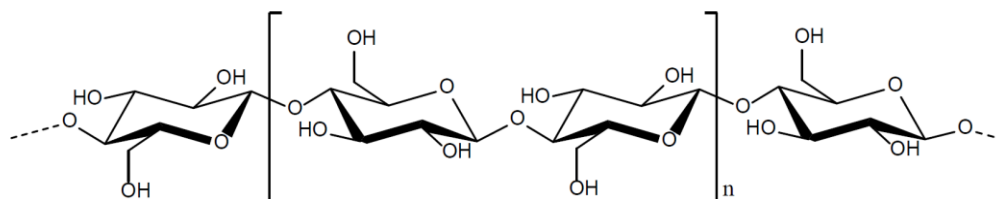


Figure 7: Molecular structure of cellulose

If cellulose is treated mechanically or chemically, two different types of nano-scaled fibers can be obtained: small and stiff cellulose nanocrystals (CNC) and long and flexible cellulose nanofibrils (CNF). There has already been a lot of research on both CNC and CNF, and a lot of different applications have been found, e.g. as mechanical reinforcements in

nanocomposites [45]–[47] like in this thesis, or drug delivery systems [48]. The terminology to describe the different types of nanocellulose is shown in Table 1.

Table 1: Terminology to describe the different types of nanocellulose [49]

Type of Nanocellulose	Diameter	Length	Production
Cellulose nanofibrils	5-60 nm	Several μm	Chemical or enzymatic pretreatment; mechanical treatment
Cellulose Nanocrystals	5-70 nm	100-250 nm (from plant cellulose); 100 nm-several μm (from cellulose of algae, bacteria and tunicates)	Acid hydrolysis

The nanocellulose itself has outstanding properties. The elastic modulus is about 150 GPa [50],[51] and the tensile strength about 10 GPa [50]. However, these properties are for single particles and should be seen as the theoretical upper limit and thus far away from the values gained when applying nanocellulose in materials. According to Karabiyik et al. [52] the refractory index is 1.51. The transmittance of nanocellulose is very high and it increases from more than 90 % at 600 nm to 93.2 % at 900 nm [53].

In material science, nanocellulose is a very promising reinforcement filler. It was shown that the mechanical properties of different polymers increase dramatically, if nanocellulose is added [45]–[47]. As an example, Wang et al. [54] chemically modified the CNC surface with 2-dodecanyl succinic anhydride to obtain hydrophobic CNC, which were mixed with an epoxy resin. The result was an increase in tensile strength by 82 %, the Young's modulus increased by 21 % and the strain at break by 198 % with an addition of only 3.5 wt% of these modified CNC.

One of the major challenges in reinforcing polymer composites with cellulose nanocrystals is to disperse the particles homogeneously. As it is with other nanoparticles, the surface energy of nanocellulose is very high and so they tend to agglomerate[55]. These agglomerates have to be broken up to ensure a good quality of particle dispersion. One method to improve the

homogeneity is to introduce other functional groups to the surface of the cellulose nanocrystals. This has already been done with 2-dodecenylsuccinic acid anhydride[54], succinic anhydride[56], polyethylene oxide[57], 4-phenylbutyl isocyanate[58], maleic anhydride[59] and many more.

1.9 Micromechanics

Mechanical properties of structures in the micrometre scale cannot simply be extrapolated from the properties of samples in larger dimensions. One reason for that is that the mechanics of bulk samples are greatly dependent on their own microstructure, and normally the dimensions of these samples are much larger than these microstructural features like grains. Another reason is that the mechanical behaviour of materials is controlled by certain fundamental length scales. An example of this is the fracture initiation of brittle materials at defects with a critical size leading to a specimen size dependent fracture strength. If the size of the tested samples is smaller than the dimensions of these small features, the mechanical properties fundamentally change[60]. Therefore, the dimensions of the tested samples have to be in the same length scale as the parts in which the material is used.

As there is a lot of progress in nanotechnology and manufacturing of very small devices like MEMS, micromechanical testing gets more and more important. The most common methods of micromechanical testing are nanoindentation, micropillar compression and micro tensile testing. As the testing samples are very small, these measurements are often performed as in-situ tests in a scanning electron microscope[61]–[63].

- **Nanoindentation:** Nanoindentation was the first characterization method for materials properties on the sub-micron scale and is the base for micropillar compression and micro tensile testing. In Nanoindentation, a tip with defined geometry, most commonly a diamond Berkovich tip, is penetrated into the material[64]. During this process, load and indenter displacement are recorded. According to Oliver and Pharr [65], with this load-displacement-curve the hardness and the elastic modulus can be determined.
- **Micropillar compression:** This method of micromechanical testing was first performed by Uchic et al.[66]. Their goal was to investigate the external size effects in single






crystal in the absence of grain boundaries. Therefore, they manufactured pillars using a focused ion beam (FIB) microscope, which were attached to the bulk sample at their bottom. For micropillar compression, the sharp indenter tip is replaced with a flat punch indenter tip, which leads to a conventional uniaxial compression. With the stress-strain-curves of these compression tests, the yield stress and the elastic modulus of the material can be determined.

- Micro tensile testing: Compared to the micromechanical testing methods described above, micro tensile testing is more complicated to realize and can be challenging[67], as sample preparation and alignment are very difficult. Although researchers have already published solutions to different questions[68]–[72], there is still no standardized method to perform micro tensile testing. Recently, Casari et al.[73] took another step towards a commonly usable setup, as they manufactured a self-aligning micro tensile setup. Thereby, a gripper, which was at the end of a compliant needle, was used. The geometry of the gripper and the specimen were calculated to align themselves in the very first part of the test. The manufacturing of the gripper and the specimen was performed by reactive ion etching (Si gripper) and FIB milling (nc-Ni gripper and specimen).

2 Experimental procedure

This chapter elucidates the experimental procedure, starting with the preparation of the cellulose nanocrystal-photoresist-mixtures and the preparation of the wafers. Details on the 2D photolithography, which was performed by direct laser writing and maskless projection lithography, and on the 3D photolithography, which was performed by two-photon-lithography, are given. With the different photoresist mixtures, different kinds of structures were printed. The dimensions of these are summarized in Table 2.

Table 2: Summary of the dimensions of all printed structures, in μm

Pillars 									
Height	40								
Diameter	13	20			26				
Aspect ratio	3	2			1.5				
Hexagons 									
Outer diameter	50								
Height	40								
Wall width	0.5	1.0	2.0	3.0	4.0	5.0	7.5	10.0	
Honeycombs 									
Outer diameter of each hexagon	50								
Height	40								
Wall width	5.0		7.5			10.0			
Cellular structures 									
Thickness of strut	4								
Dimensions of unit cell	30x30x30								
Number of cells	3x3x3								
Tensile testing samples 									
Dimensions of gauge section	4x8x20								

2.1 Materials

All the materials used in this thesis are listed in Table 3 including the supplier and the purity, if known.

Table 3: Materials, their purity and supplier used in this thesis

Material	Supplier	Purity
SU-8 GM 1075 photoresist	Gersteltec	N/A
IP-S photoresist	Nanoscribe	N/A
1-methoxy-2-propanol acetate (PGMEA)	Microchemicals	VLSI
Isopropanol (development step)	Microchemicals	ULSI
Isopropanol (solvent exchange step)	Thommen Furler	99 %
Acetone	Microchemicals	ULSI
2-Hydroxyethyl methacrylate (HEMA)	Sigma-Aldrich	98 %
Cellulose nanocrystals (CNC)	Celluforce	N/A
γ -butyrolactone (GBL)	Sigma-Aldrich	$\geq 99\%$
Irgacure 819	BASF	N/A
TI Prime Adhesion Promoter	Microchemicals	N/A
Single crystal silicon wafers in $\langle 100 \rangle$ orientation	Microchemicals	N/A
Borosilicate glass wafers (30 mm in diameter, 0.17 mm thick)	Thermo Fisher Scientific	N/A

In Figure 8, all composites manufactured and processed in this thesis are summarized.

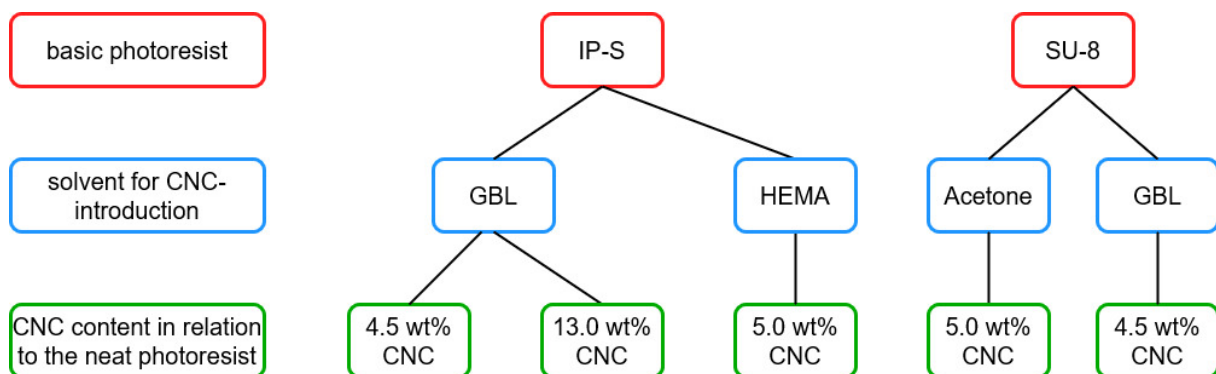


Figure 8: Summary of all CNC composites manufactured and processed in this thesis

2.2 General photolithography steps

In this section the general photolithography process steps performed in this thesis are explained. Not all of these steps were performed with all of the mixtures. In the sections of the respective mixtures is mentioned which of the steps were performed for processing them.

2.2.1 Removal of the adsorbed water

To ensure a good adhesion of the photoresist to the wafers the adsorbed water on the surface had to be removed. Therefore, the wafers were put onto a piece of paper on a hotplate at 160 °C for at least 20 min.

2.2.2 Spin coating

To generate a uniform film of photoresist, a spin coating step was performed. The wafers were put onto the chuck of the spin coater (SAWATEC SM-180-BT for neat SU-8, POLOS MCD200 for other photoresist, Figure 9) and the photoresist was dispersed in the middle of the wafer. Different spin coating recipes were performed (Figure 10).

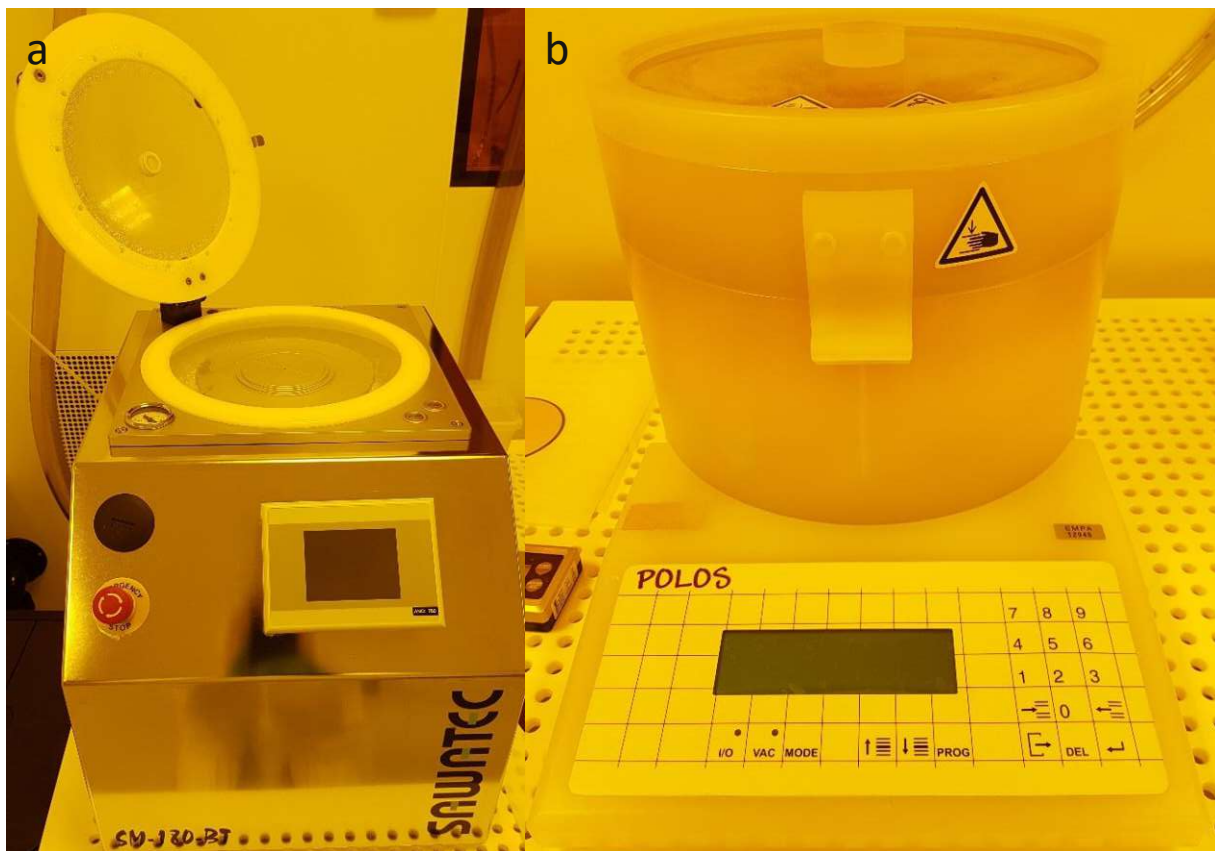


Figure 9: Different spin coaters used in this thesis: a, SAWATEC SM-180-BT; b, POLOS MCD200

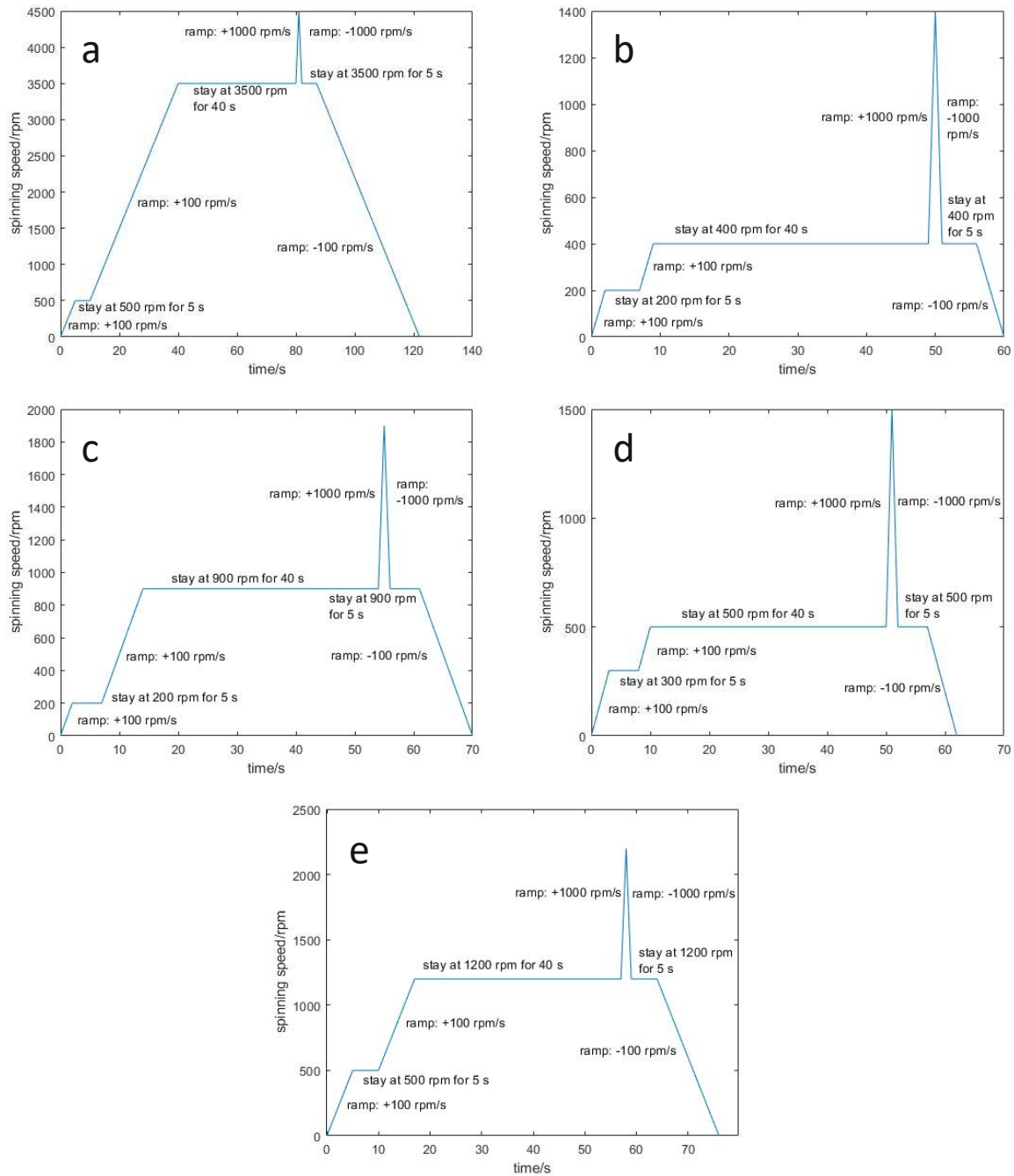


Figure 10: Spin coating recipes with different spinning speeds in the dispersing step

2.2.3 Soft baking (SB)

The most photoresists used in this thesis contained some solvent which had to be removed before exposure. Therefore, a soft baking step was performed. The wafer with the photoresist film was put onto a piece of paper on a hotplate (SAWATEC HP-401, Figure 11 a,). The recipes used in this thesis are shown in Figure 11 b, - d,.

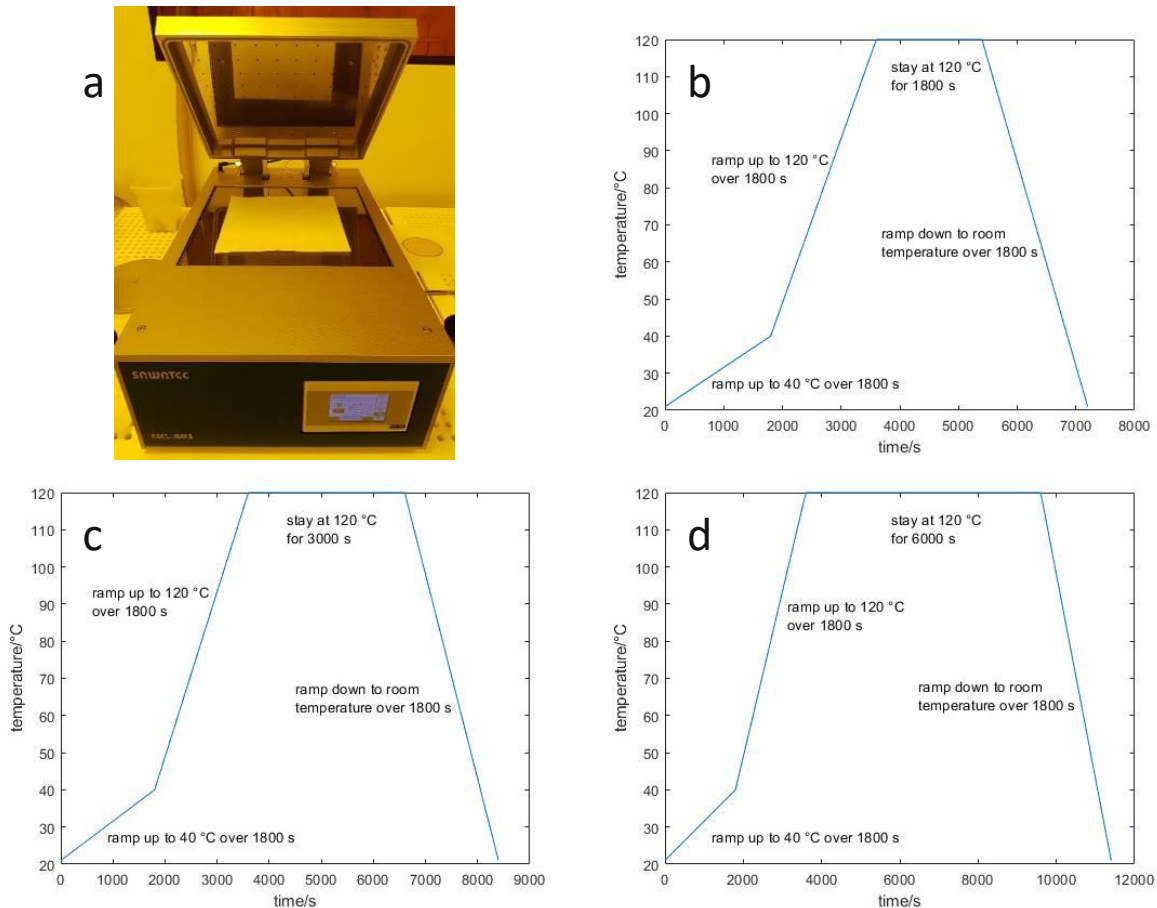


Figure 11: a, Hotplate used in this thesis: SAWATEC HP-401; b, - d, Soft baking recipes used in this thesis with different durations at 120 °C

2.2.4 Exposure

2.2.4.1 2D Lithography: Exposure to UV-radiation

Two different types of machines were used for exposure to UV-radiation. The direct laser writer DLW (HEIDELBERG INSTRUMENTS μ PG 101, Figure 12 a) has a better resolution than the maskless projection system MPS (INTELLIGENT MICRO PATTERNING SF-100, Figure 12 b), but the printing process takes much more time at the DLW and the optical parts are much more sensitive compared to the MPS. For this reason, the MPS was chosen for trying to process the new polymers and once the process was optimised for this machine, the DLW was used to print structures with higher resolution. Another advantage of the MPS is, that with this method both liquid and solid resist can be exposed.

2.2.4.2 3D Lithography: 2-Photon-Lithography

The exposure was performed on a Nanoscribe Photonic Professional GT system (Figure 12 c) in oil-immersion mode (Figure 5, upper right side). The objective used was the 25x NA0.8

objective from Nanoscribe. The scanning speed was set to 10 mm/s. The laser intensity of this system is $3.09 - 3.98 \cdot 10^{-7} \text{ J/cm}^2$ with a wavelength of 780 nm and a pulse duration of 120 fs.

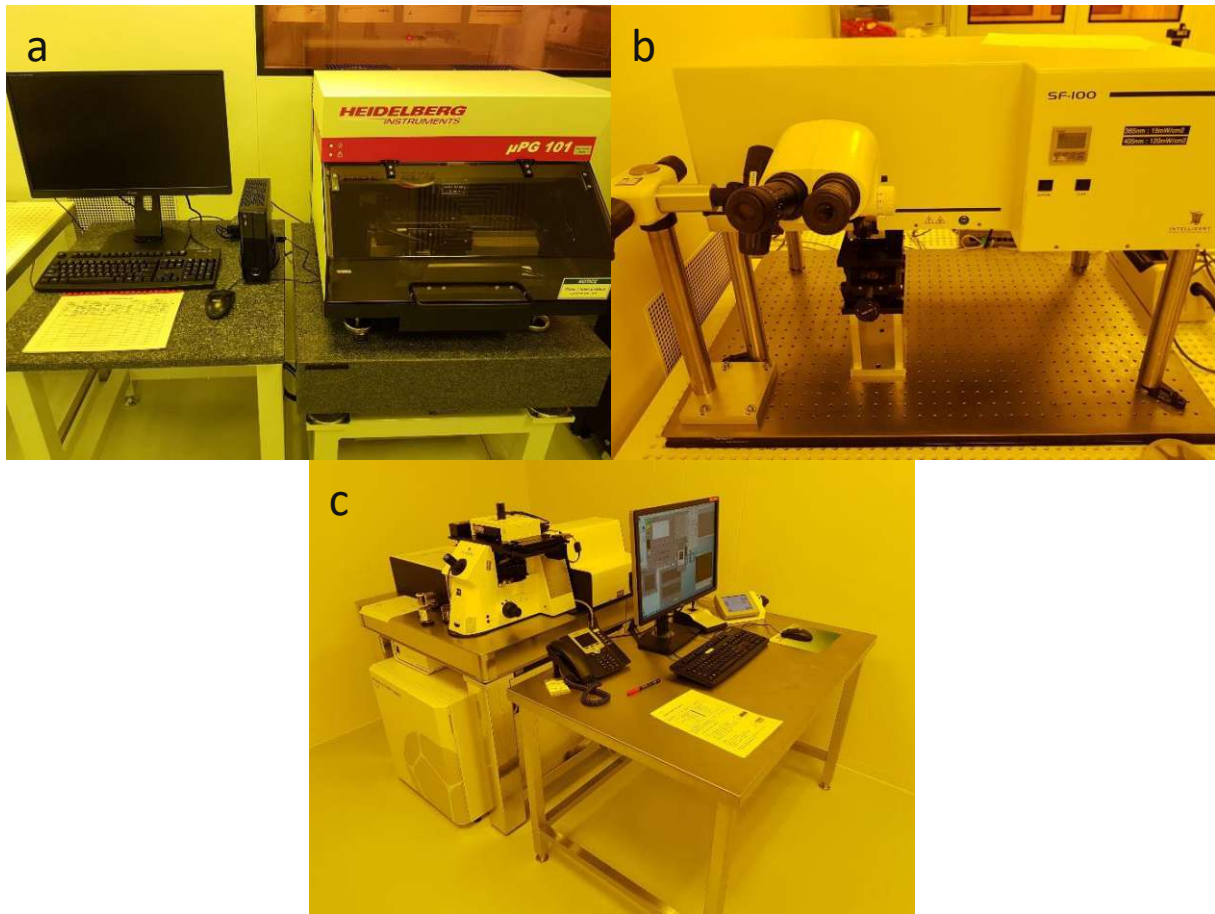


Figure 12: Lithography systems used in this thesis: a, HEIDELBERG INSTRUMENTS μ PG 101; b, INTELLIGENT MICRO PATTERNING SF-100; c, Nanoscribe Photonic Professional GT system

2.2.5 Post exposure baking (PEB)

During the post exposure baking step, the polymerization of the resist happens, as mentioned in chapter 1.6. This step was performed by putting the wafers onto a piece of paper on a hotplate (SAWATEC HP-401, Figure 11 a,). The temperature profile shown in Figure 13 was used.

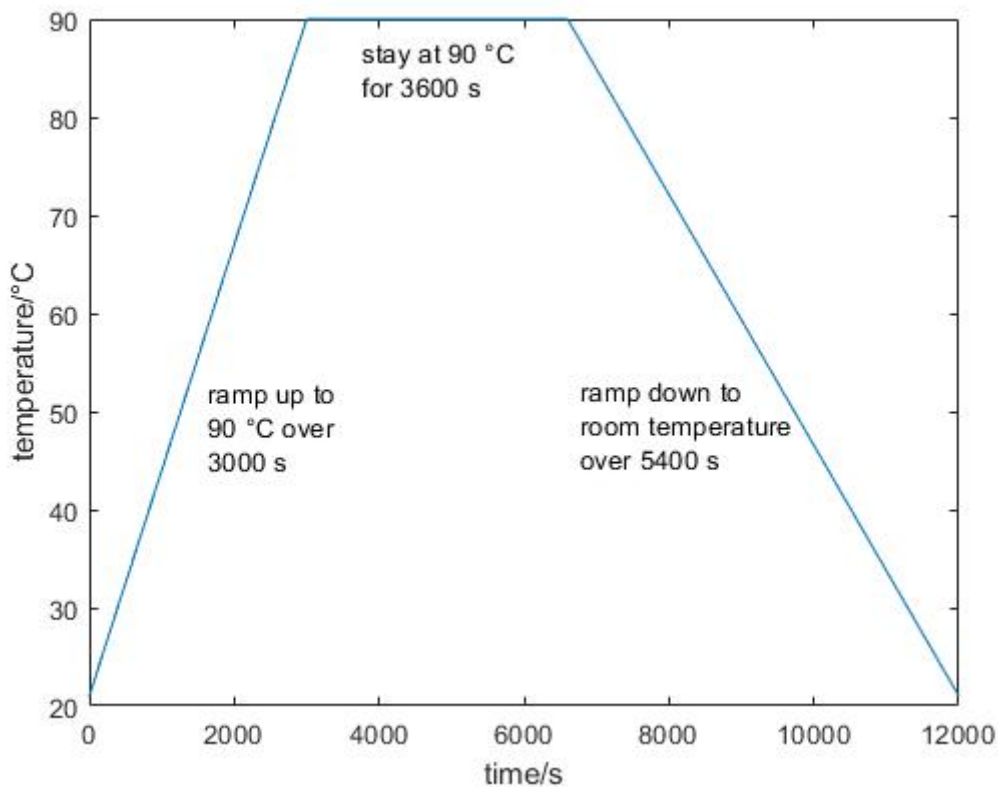


Figure 13: Post exposure baking recipe for photoresists containing SU-8

2.2.6 Development

To dissolve the unpolymerized parts of the photoresist the wafers were put either face down or in vertical position into a sample holder which was put into 1-Methoxy-2-propanyl acetate, short PGMEA. This step took from 3 minutes for the neat photoresist to 55 min for the IP-S/CNC/GBL with 13 wt% CNC. Directly afterwards the holder with the wafer was put in isopropanol to stop the development process. This step took 50 s for neat SU-8 on silicon wafers and 5 s for all the other experiments.

2.2.7 Microscopy

The samples were examined with an optical microscope (BRESSER Science MTL 201) and a scanning electron microscope SEM (PHILIPS XL30 ESEM-FEG). The acceleration voltage was set to 5 kV for the sputtered samples, for the unsputtered samples it was set to 0.8 and 1.0 kV, respectively.

2.2.8 Mechanical testing

The micro-compression testing was performed on an in-situ micro-indenter (Alemnis) in a Hitachi TM3030 Plus Desktop-SEM (Figure 14) to investigate the influence of the shape of the structures, the laser power, and the amount of CNC on the mechanical properties.

For the compression a diamond flat punch with a diameter of $150\ \mu\text{m}$ was used. A strain rate of $10^{-3}\ \text{s}^{-1}$ was chosen. The load-displacement-curves from the micropillar compression tests were transformed in stress-strain-curves. The yield stress was determined with a strain offset of 2 %. The Young's modulus was determined by finding the linear slope during elastic deformation, the hardening modulus by finding the linear slope during plastic deformation. For the determination of the peak strength of the cellular structures, the sum of the cross sections of the vertical struts in the uppermost layer was converted in an equivalent pillar diameter.

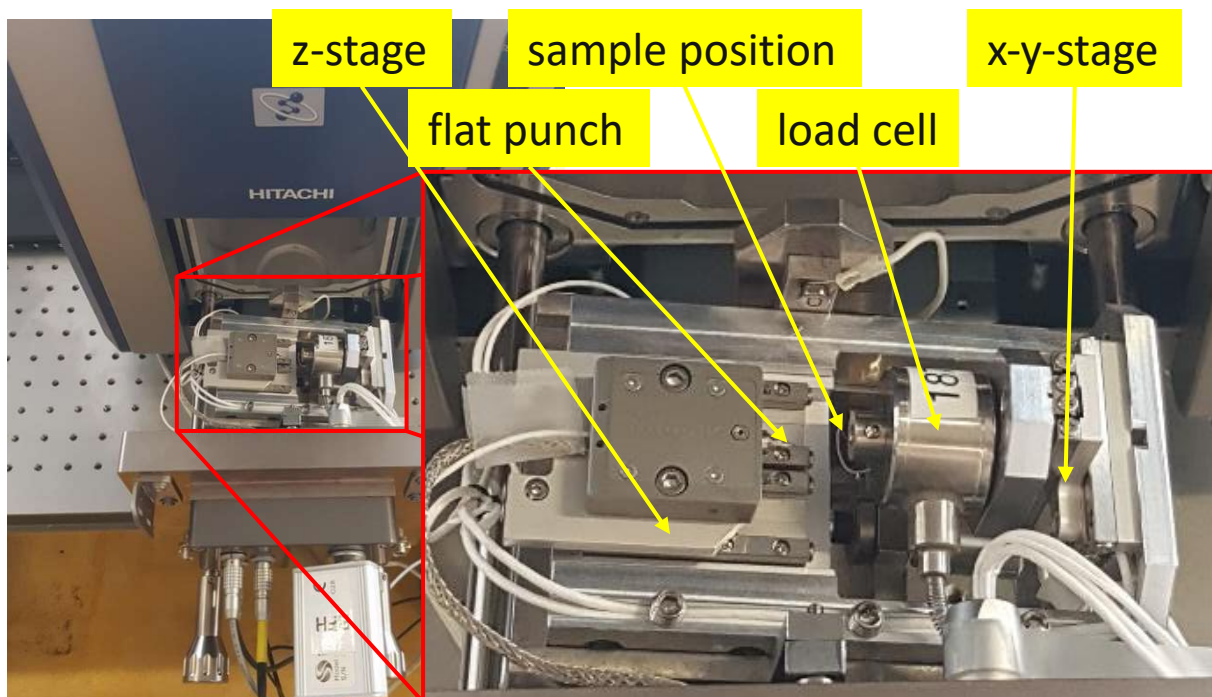


Figure 14: In-situ micro-indenter (Alemnis) in a Hitachi TM3030 Plus SEM

Tensile tests on the 3D printed specimens were conducted using the setup shown in Figure 15. The setup consisted of a micro-indenter equipped with a Silicon (Si) tensile gripper, which allowed to grip and pull the specimens in displacement control. The Si gripper was designed to be laterally compliant thus allowing self-alignment with the specimens in case of small misalignments [73]. A high magnification (28x) optical system was employed to visualize and

align both gripper and the specimens before testing. Specimens were tested at a strain rate of $1.5 \cdot 10^{-3} \text{ s}^{-1}$. Although the mechanical setup originally featured a hydration chamber to control relative humidity to mimic specific environmental conditions, here relative humidity was not imposed.

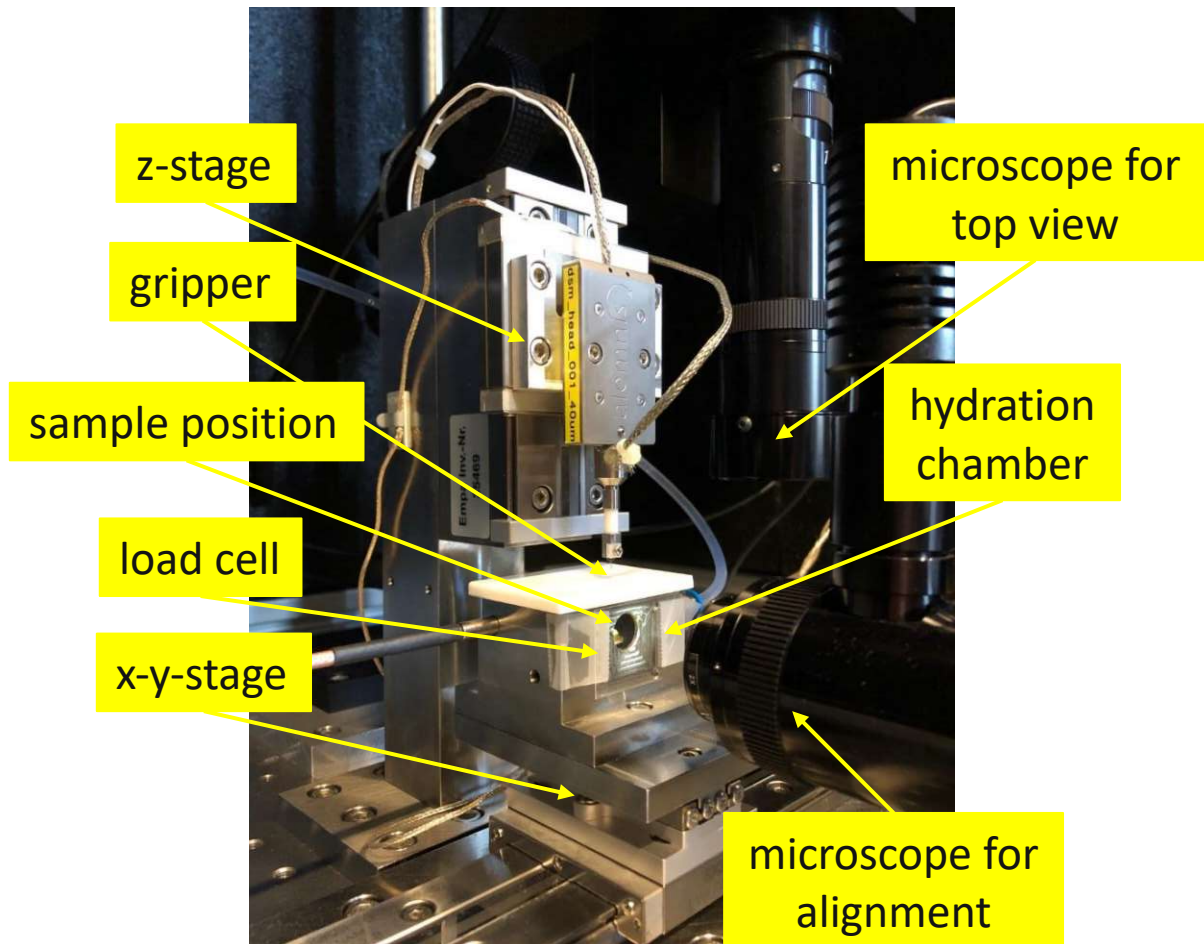


Figure 15: Setup for tensile testing (Alemnis)

2.3 Preparation of the cellulose nanocrystal (CNC)-photoresist-mixtures

2.3.1 SU-8/CNC/Acetone with 5.0 wt% CNC

A CNC-acetone suspension with unknown amount of CNC was sonicated for 5 min with magnetic stirring. To determine the exact amount of CNC in acetone, a certain amount of the suspension was put into tared aluminium bowls, which were placed in a compartment dryer at $60 \text{ }^\circ\text{C}$ for 2 h. The data of the determination are shown in Table 4.

Table 4: Data of the determination of the CNC content in acetone

Number of determination	1	2	3
$m_{\text{suspension}}$ in g	1.0100	1.0540	1.0560
$m_{\text{dry CNC}}$ in g	$2.9 \cdot 10^{-3}$	$2.8 \cdot 10^{-3}$	$3.1 \cdot 10^{-3}$
wt-% of CNC in acetone	0.287	0.266	0.294
average wt-% of CNC in acetone	0.282		

To concentrate the CNC in acetone, the suspension was poured into a tared round bottom evaporating flask and some of the acetone was evaporated by rotary evaporation. The flask was scaled again and the concentration of CNC in acetone was calculated to be 6.26 wt% (Table 5).

Table 5: Data of the determination of the CNC content in acetone after concentrating

$m_{\text{suspension}}$ in g	$m_{\text{suspension after evaporation}}$ in g	wt-% of CNC in acetone
619.58	27.93	6.26

12.00 g of the concentration suspension were mixed with 14.25 g SU-8 with a speed mixer (DAC 150.1 FVZ) at 2000 RPM, 2400 RPM and 3500 RPM for 5 min respectively to get a final concentration of 5.0 wt% CNC in SU-8, if the acetone was not in the mixture.

2.3.2 SU-8/CNC/GBL with 4.5 wt% CNC

150.50 g of a CNC-water gel with 20 wt% CNC were mixed with 400 g isopropanol. The mixture was homogenised with an ULTRA-TURRAX (T25) for 5 min at 13.000 RPM. Then the suspension was centrifuged at 7.277 RCF for 15 min at 5 °C (Sorvall RC 3BP). The supernatant fluid was disposed. This solvent exchange process of adding 400 g isopropanol, homogenising, centrifuging and disposing the supernatant fluid was performed two more times.

Another solvent exchange was performed from isopropanol to γ -butyrolactone (GBL). 30 g CNC-isopropanol gel were mixed with 60 g GBL and homogenised with an ULTRA-TURRAX at 13.000 RPM for 5 min. The suspension was centrifuged twice at 4.863 RCF (Hettich Rotina 380) for 5 min each. The supernatant fluid was disposed and 29.1 g GBL were added to the mixture.

It was homogenised again at 13.000 RPM for 5 min and centrifuged at 10.000 RCF for 10 min (Eppendorf Centrifuge 5810). The supernatant fluid was disposed. To determine the exact amount of CNC in the residue, three aluminium bowls were filled with a certain amount of CNC-GBL gel and putting into a compartment dryer for 12 h. The data is shown in Table 6.

Table 6: Data of the determination of the CNC content in GBL after solvent exchange

Number of determination	1	2	3
$m_{\text{suspension}}$ in g	0.2348	0.2467	0.2347
$m_{\text{dry CNC}}$ in g	$28.7 \cdot 10^{-3}$	$30.1 \cdot 10^{-3}$	$28.7 \cdot 10^{-3}$
wt-% of CNC in GBL	12.2	12.2	12.2
average wt-% of CNC in GBL	12.2		

12 g of the CNC-GBL gel were diluted with 19.2 g GBL and 10 g of this dilution were mixed with 10 g of SU-8, so that the amount of CNC in relation to the neat SU-8 after evaporating the GBL in a soft baking step is 4.5 wt%. The mixture was speed mixed at 3.500 RPM for 5 min.

2.3.3 IP-S/CNC/GBL

Mixtures of IP-S and CNC in GBL were produced with two different amounts of CNC. The following concentrations were chosen: 4.5 and 13.0 wt%.

2.3.3.1 IP-S/CNC/GBL with 4.5 wt% CNC

For manufacturing the mixture with 4.5 wt% CNC, the CNC-GBL dilution from chapter 2.3.2 was used. 5 g of the dilution were mixed with 5 g IP-S, which resulted in a CNC concentration of 4.5 wt% in relation to the neat IP-S after evaporating the GBL in a soft baking step. The mixture was speed mixed at 3.500 RPM for 5 min.

2.3.3.2 IP-S/CNC/GBL with 13.0 wt% CNC

As starting material, the CNC-isopropanol gel from chapter 2.3.2 was used. 30 g CNC-isopropanol gel was mixed with 65 g GBL and homogenised with an ULTRA-TURRAX at 13.000 RPM for 5 min. The suspension was centrifuged at 4.863 RCF for 10 min. The supernatant fluid was disposed. The residue (36.62 g) was mixed with 58.4 g GBL and homogenised at 13.000 RPM for 5 min. The suspension was centrifuged at 10.000 RCF for

10 min and the supernatant fluid was disposed. The process of homogenisation, centrifugation and disposal of the supernatant fluid was performed again with 60.9 g GBL. The residue was diluted with 43.2 g GBL and speed mixed (DAC 600 VAC) with a ceramic ball at 1.000 RPM, 1.500 RPM, 2.000 RPM and 2.350 RPM for 2 min each. The amount of CNC in the dilution was determined by filling two aluminium bowls with a certain amount of CNC-GBL gel and putting them in a compartment dryer at 60 °C for 20 h. The data is shown in Table 7.

Table 7: Data of the determination of the CNC content in GBL after solvent exchange

Number of determination	1	2
$m_{\text{suspension}}$ in g	1.2425	2.2125
$m_{\text{dry CNC}}$ in g	$73.8 \cdot 10^{-3}$	$130.9 \cdot 10^{-3}$
wt-% of CNC in GBL	5.94	5.92
average _{wt-% of CNC in GBL}	5.93	

17.19 g of the dilution were mixed with 6.85 g IP-S and speed mixed at 3.500 RPM for 3 min. This results in a mixture with 13.0 wt% CNC in relation to the neat IP-S after evaporating the GBL in a soft baking step.

2.3.4 IP-S/CNC/HEMA

10 g of a CNC/water-gel (20 wt% CNC) was diluted with 30 g water. The mixture was speed mixed (DAC 150.1 FVZ) at 2.000 RPM, 2.400 RPM and 3.500 RPM for 5 min respectively. The suspension was mixed with 19 g of hydroxyethylmethacrylate, short HEMA, and speed mixed at 3.500 RPM for 5 min. Then, the mixture was poured into a tared round bottom evaporating flask to evaporate the water by rotary evaporation. This process was done until the weight of the flask was constant and all the water was evaporated. The final concentration of CNC in the CNC/HEMA-gel was 9.5 wt%. 10.52 g of the gel was mixed with 9.40 g IP-S with a speed mixer with a ceramic ball at 1.400 rpm, 2.000 rpm and 2.400 rpm for 5 min each. After removing the ceramic ball, the mixture was speed mixed again at 3500 rpm for 5 min. Then 10 g of this mixture were speed mixed with 0.15 g Irgacure 819 photoinitiator at 1.500 and 2.500 rpm for 3 min and at 3.500 rpm for 2 min.

2.4 SU-8 2D Lithography

The experimental part with the SU-8 photoresist was performed with silicon single crystal wafers in $\langle 1\ 0\ 0 \rangle$ orientation. The experiments contained the following steps, which were performed as described in chapter 2.2 General photolithography steps, while in this section only deviations to the general protocol are mentioned:

- 2.2.1 Removal of the adsorbed water
- 2.2.2 Spin coating (Figure 10 a,)
- 2.2.3 Soft baking (SB) (Figure 11 b,)
- 2.2.4 Exposure

2.4.1 Exposure with the direct laser writer

To achieve the best results, the optimum parameters for exposure had to be determined. Therefore, a dose and resolution test was performed. The pattern and the parameters for the attenuator and the defocus are shown in Table 8 and Figure 16. The intensity was set to 12 mW/cm^2 and a filter was placed in the optical path. As the filter blocks about 70 % of the UV-intensity, the maximum intensity was about 3.6 mW/cm^2 , but as the manufacturer of the machine had no validated values for this filter, these values could differ slightly. The attenuation of the UV radiation could be seen as linear in this range.

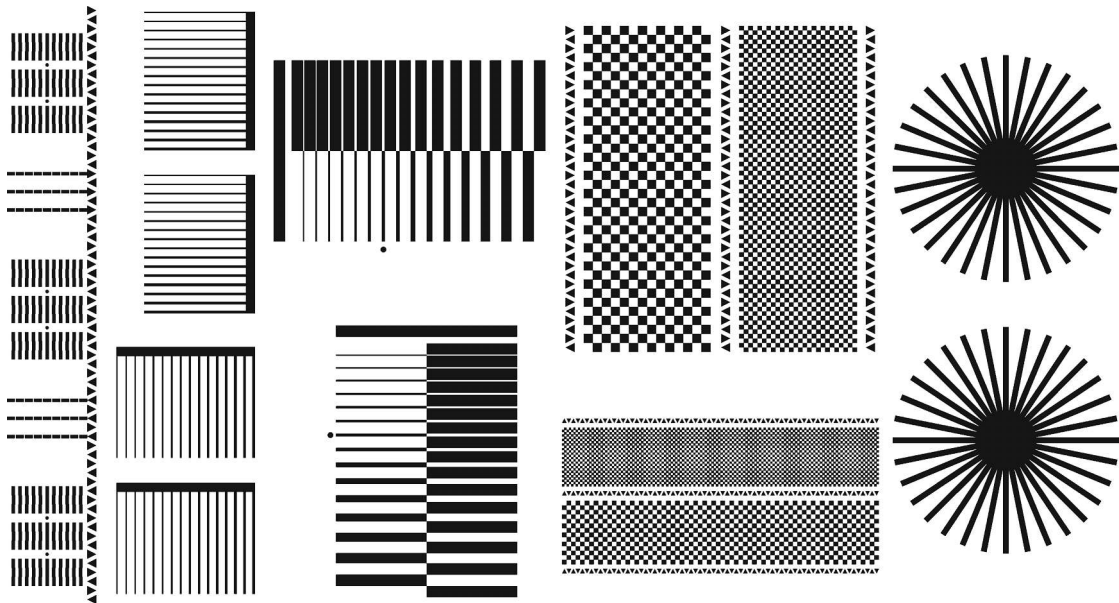
Afterwards, structures for mechanical testing were printed with the optimum parameters. An array with 51×51 structures of each type and a distance of $200\ \mu\text{m}$ between the centres of each structure was chosen. The following structures were printed:

- Pillars with a diameter of $13\ \mu\text{m}$, $20\ \mu\text{m}$ and $26\ \mu\text{m}$
- Hexagons with wall widths of $5.0\ \mu\text{m}$, $7.5\ \mu\text{m}$ and $10.0\ \mu\text{m}$
- Honeycombs with wall widths of $5.0\ \mu\text{m}$, $7.5\ \mu\text{m}$ and $10.0\ \mu\text{m}$

The further dimensions of these structures like height are listed in Table 2.

Table 8: Parameters for the dose and resolution test for SU-8 on the direct laser writer

	Gap between the fields	Number of fields	Starting value	Step size
x-axis (defocus)	2000 μm	6	0	+3
y-axis (attenuator)	2000 μm	13	10 %	5 %

Figure 16: Pattern for the dose and resolution test for SU-8 on the direct laser writer, dimensions about 3930x2100 μm

2.4.2 Exposure with the maskless projection system

Like for the direct laser writer, a dose and resolution test had to be performed with the maskless projection system. The pattern for the dose and resolution test is shown in Figure 17. The intensity of the 365 nm radiation was 26.5 mW/cm² and the intensity of the 405 nm radiation was 181 mW/cm². The exposure time was set to 6.5, 7.0, 7.3, 7.5, 7.8, 8.1 and 8.5 s.

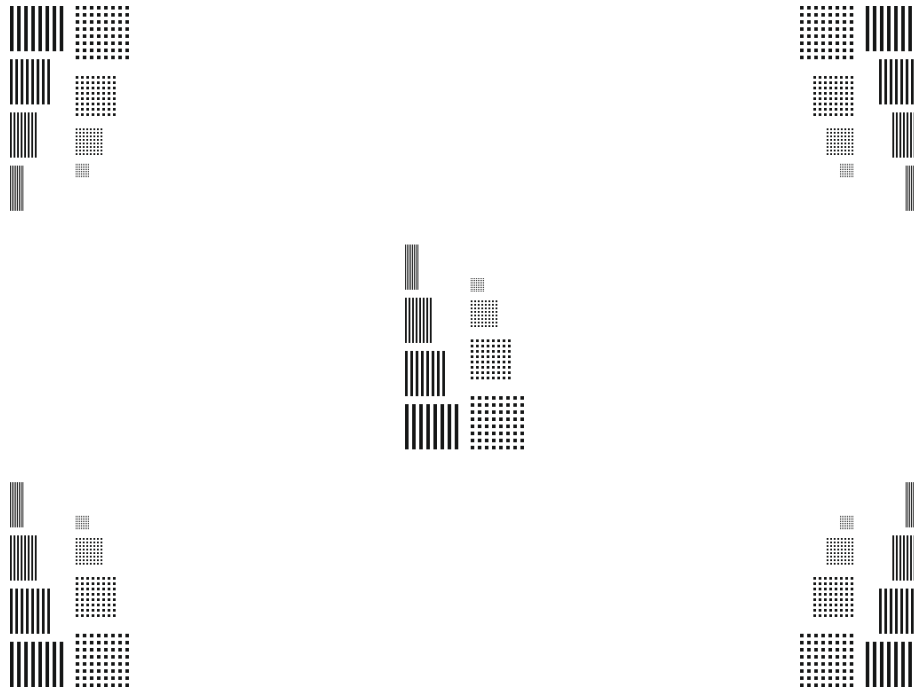


Figure 17: Pattern for the dose and resolution test for SU-8 on the maskless projection system, dimensions about 12.3x9.2 mm

- 2.2.5 Post exposure baking (PEB)
- 2.2.6 Development

The wafer was put face down into PGMEA. The development times were 3 minutes in PGMEA and directly afterwards 50 s in isopropanol to stop the development process.

- 2.2.7 Microscopy

For the SEM the samples were sputtered with 4 nm of gold at a sputter rate of 0.05 nm/s. This was performed with a Leica EM ACE600.

- 2.2.8 Mechanical testing

2.5 SU-8/CNC composites 2D Lithography

As for the experiments with neat SU-8, silicon single crystal wafers in $\langle 1\ 0\ 0 \rangle$ orientation were used.

2.5.1 SU-8/CNC/Acetone with 5.0 wt% CNC

Different spin coating protocols were tried (Figure 10 b, d, and e), but all of them failed. The mixture did not wet the surface of the wafer, it was just spun from the wafer. As a result, no more experiments with this mixture were performed.

2.5.2 SU-8/CNC/GBL with 4.5 wt% CNC

The lithography process with this mixture contained the following steps, which were performed as described in chapter 2.2 General photolithography steps, while in this section only deviations to the general protocol are mentioned:

- 2.2.1 Removal of the adsorbed water
- 2.2.2 Spin coating (Figure 10 b,)
- 2.2.3 Soft baking (SB) (Figure 11 b,)
- 2.2.4 Exposure

The exposure was only performed with the maskless projection system with exposure times between 30 and 50 s. The pattern is shown in Figure 18. The intensity of the 365 nm radiation was 26.5 mW/cm² and the intensity of the 405 nm radiation was 181 mW/cm².

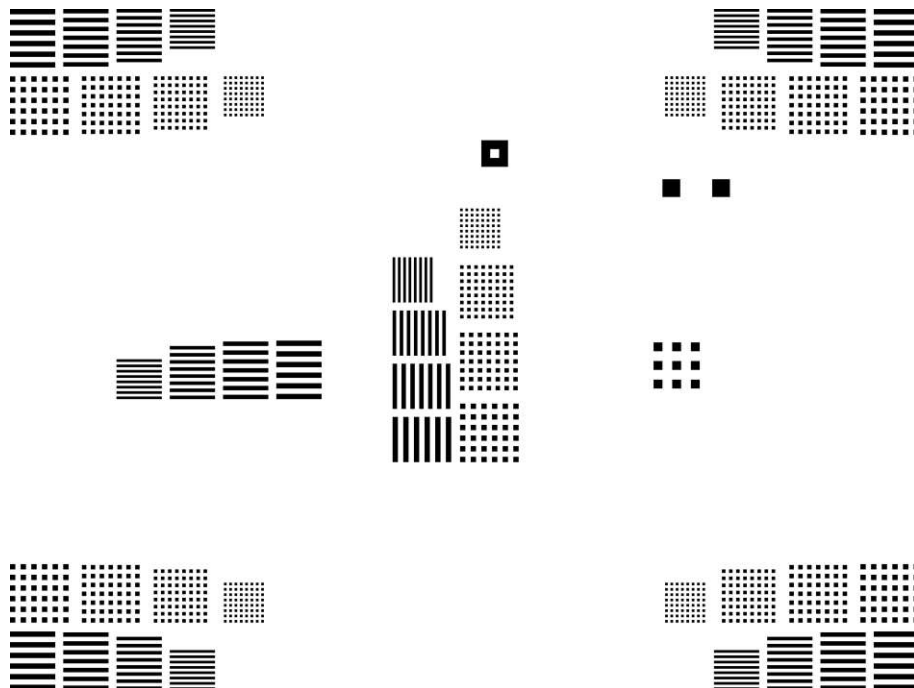


Figure 18: Pattern for the 2D lithography with CNC-photoresist mixtures on the maskless projection system, dimensions about 12.3x9.2 mm

- 2.2.5 Post exposure baking (PEB)
- 2.2.6 Development

The development was performed by putting the wafer in vertical position into PGMEA with magnetic stirring, so that the flow was directly against the surface of the wafer. After 10 min, the wafer was ultra-sonicated in PGMEA for 30 s, then it was put in isopropanol for 45 s.

- 2.2.7 Microscopy

2.6 IP-S 2D Lithography

The experimental procedure of the Nanoscribe IP-S photoresist was performed with different wafers (glass wafers and silicon single crystal wafers in $\langle 100 \rangle$ orientation). The experiments contained the following steps, which were performed as described in chapter 2.2 General photolithography steps, while in this section only deviations to the general protocol are mentioned:

- 2.2.1 Removal of the adsorbed water
- 2.2.2 Spin coating (Figure 10 c,)
- 2.2.3 Soft baking (SB) (Figure 11 b,)

As it is not known if the soft baking step has any influence on the IP-S 2D lithography, this step was not performed with all of the wafers.

- 2.2.4 Exposure

The exposure was only performed with the maskless projection system, the pattern is shown in Figure 19. The intensity of the 365 nm radiation was 26.5 mW/cm^2 and the intensity of the 405 nm radiation was 181 mW/cm^2 . Different durations of exposure from 30 to 130 s were performed.

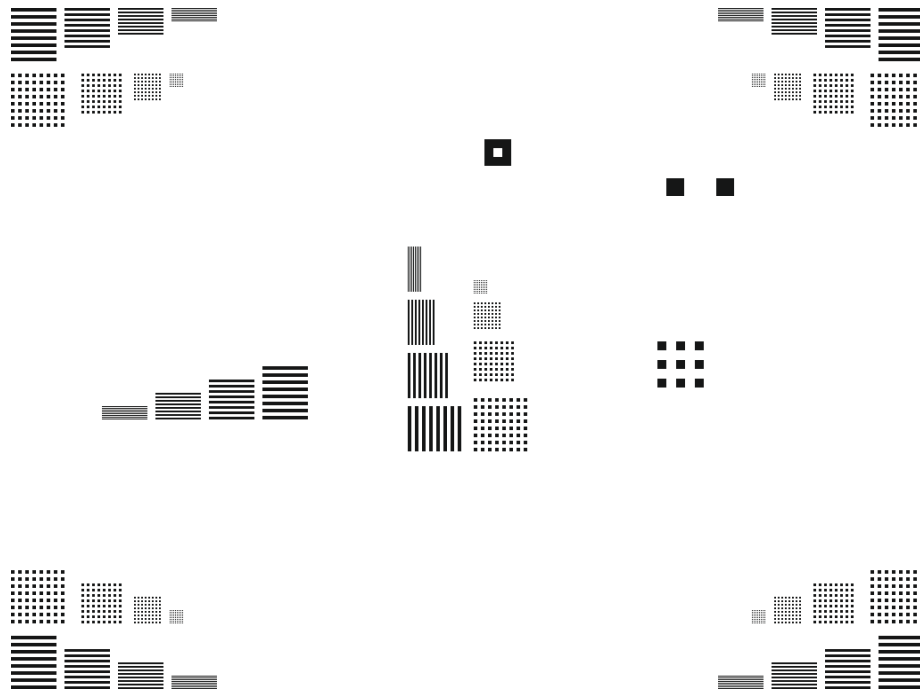


Figure 19: Pattern for the dose and resolution test for IP-S on the maskless projection system, dimensions about 12.3x9.2 mm

- 2.2.6 Development

In this step different sample holders (wafer in vertical position and wafer face down) were used and different durations for PGMEA and isopropanol were done.

- 2.2.7 Microscopy

2.7 IP-S/CNC composites 2D Lithography

For the experiments with the IP-S/CNC mixtures, silicon single crystal wafers in $\langle 1\ 0\ 0 \rangle$ orientation and glass slides were used.

2.7.1 IP-S/CNC/GBL with 4.5 wt% CNC

The lithography process of this mixture contained the following steps, which were performed as described in chapter 2.2 General photolithography steps, while in this section only deviations to the general protocol are mentioned:

- 2.2.1 Removal of the adsorbed water
- 2.2.2 Spin coating (Figure 10 d,)
- 2.2.3 Soft baking (SB) (Figure 11 b,)

- 2.2.4 Exposure

The exposure was only performed with the maskless projection system, the pattern is shown in Figure 19. The intensity of the 365 nm radiation was 26.5 mW/cm² and the intensity of the 405 nm radiation was 181 mW/cm². The exposure time was set to 80 s.

- 2.2.6 Development

The silicon wafer was put face down in PGMEA for 5 min, the glass wafer was put in vertical position into PGMEA for 8 min. Then both of them were rinsed with PGMEA and put in a beaker with isopropanol for 20 s.

- 2.2.7 Microscopy

2.7.2 IP-S/CNC/HEMA

The steps performed with the IP-S/CNC/HEMA mixture contained the following steps, which were performed as described in chapter 2.2 General photolithography steps, while in this section only deviations to the general protocol are mentioned:

- 2.2.1 Removal of the adsorbed water
- 2.2.2 Spin coating

As the mixture was gel-like, it was not possible to spin coat it. Different spin coating recipes were tried (see Figure 10 b, d, and e,), but the mixture did not spread over the wafer. Clumps of the mixture were just spun from the wafer.

2.8 SU-8 3D Lithography

The process was performed with glass slides as substrates containing the following steps, which were performed as described in chapter 2.2 General photolithography steps, while in this section only deviations to the general protocol are mentioned:

- 2.2.1 Removal of the adsorbed water

After this step, some TI Prime Adhesion Promoter (Microchemicals) was dispersed in the middle of the wafer through spin coating (POLOS MCD200). The recipe is shown in Figure 20.

Then the wafer was put on a hotplate at 120 °C for 2 min. Then a drop of SU-8 was dripped on the glass slide with a pipette.

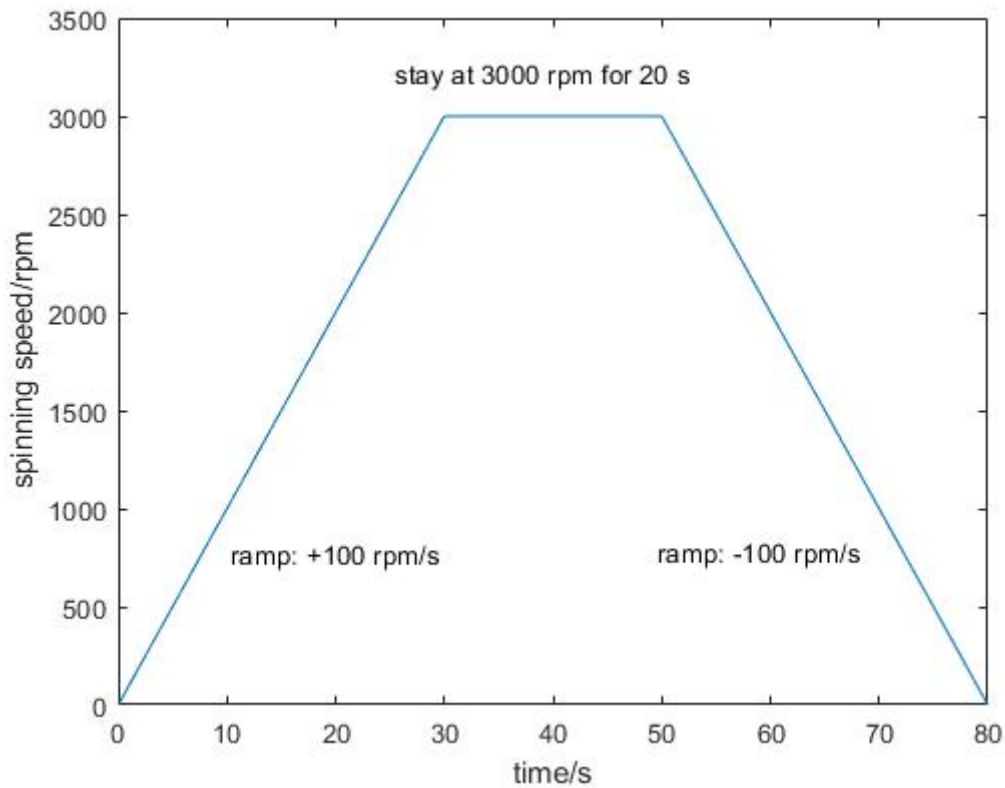


Figure 20: Spin coating recipe for the application of TI Prime Adhesion Promoter

- 2.2.3 Soft baking (SB) (Figure 11 c,)

The soft baking was performed twice, as the photoresist was still soft after the first run.

- 2.2.4 Exposure

An array of pillars with 13 μm in diameter and 40 μm in height was printed with different laser powers from 12 to 25.5 mW.

- 2.2.5 Post exposure baking (PEB)
- 2.2.6 Development

The wafer was put face down into PGMEA for 26 min. Then the wafer was put in isopropanol for 5 s.

- 2.2.7 Microscopy
- 2.2.8 Mechanical testing

2.9 SU-8/CNC composites 3D Lithography

The 3D printing was only performed with the SU-8/CNC/GBL mixture containing the following steps, which were performed as described in chapter 2.2 General photolithography steps, while in this section only deviations to the general protocol are mentioned:

- 2.2.1 Removal of the adsorbed water

Directly after this step, some TI Prime Adhesion Promoter (Microchemicals) was dispersed in the middle of the wafer through spin coating (POLOS MCD200). The recipe is shown in Figure 20. Then the wafer was put on a hotplate at 120 °C for 2 min. Then a few drops of the SU-8/CNC/GBL mixture were dripped on the glass slide with a pipette.

- 2.2.3 Soft baking (SB) (Figure 11 c,)

The soft baking was performed twice, as the photoresist was still soft after the first run.

- 2.2.4 Exposure

An array of pillars with 13 μm in diameter was printed with different laser powers from 14 to 23.5 mW. Furthermore, hexagons with wall widths from 0.5 μm to 5.0 μm were printed with 15 mW laser power to investigate the best resolution achievable. The other dimensions of the structures are listed in Table 2.

- 2.2.5 Post exposure baking (PEB)
- 2.2.6 Development

The wafer was put in vertical position into PGMEA for 10 min with magnetic stirring, so that the flow was directly against the surface of the wafer. Then the glass slide was rinsed with PGMEA by applying some pressure with a squeeze bottle to wash away the cellulose, which did not dissolve in PGMEA. This was repeated three times. Then the wafer was put in isopropanol for 5 s.

- 2.2.7 Microscopy

- 2.2.8 Mechanical testing

2.10 IP-S 3D Lithography

All the experiments were performed using glass slides as substrates. After rinsing the wafer with isopropanol and dripping a drop of IP-S on the glass slide, the process contained the following steps, which were performed as described in chapter 2.2 General photolithography steps, while in this section only deviations to the general protocol are mentioned:

- 2.2.4 Exposure

An array of pillars with 13 μm in diameter and 40 μm in height were printed with laser powers from 12.5 to 27.5 mW. Cellular structures were printed with 4 μm thick struts and a laser power of 15 mW. Samples for tensile testing with a gauge section of 4x8x20 μm with different laser powers from 15 to 30 mW. The other dimensions of the printed structures are shown in Table 2.

- 2.2.6 Development

The wafer was put in vertical position into PGMEA for 10 min and directly afterwards in isopropanol for 10 min.

- 2.2.7 Microscopy

The images of the tensile samples were taken on a Hitachi S4800.

- 2.2.8 Mechanical testing

2.11 IP-S/CNC composites 3D Lithography

All the experiments were performed using glass slides as substrates.

2.11.1 IP-S/CNC/GBL with 4.5 wt% CNC

The lithography process of this mixture was performed containing the following steps, which were performed as described in chapter 2.2 General photolithography steps, while in this section only deviations to the general protocol are mentioned:

- 2.2.1 Removal of the adsorbed water

After this step, some drops of the mixture were dripped on the wafer.

- 2.2.3 Soft baking (SB) (Figure 11 c, for pillars, hexagons and tensile samples; Figure 11 d, for cellular structures)

This step was performed twice for the pillars, the hexagons and the tensile samples, as there was still some GBL in the resist.

- 2.2.4 Exposure

An array of pillars with 13 μm in diameter was printed with laser powers from 15.5 to 27.5 mW. Furthermore, hexagons with wall widths from 0.5 to 5.0 μm were printed with a laser power of 25 mW to investigate the best resolution achievable. Cellular structures were printed with 4 μm thick struts with a laser power of 15 mW and tensile samples with a gauge section of 4x8x20 μm were printed with different laser power from 15 to 30 mW. The further dimensions of the structures were listed in Table 2.

- 2.2.6 Development

The wafer was put into PGMEA in vertical position. The magnetic stirring caused a flow, which was directly against the surface of the wafer. This step was done until the unpolymerized parts detached. This took about 40 min. Then the wafer was rinsed with PGMEA and put in isopropanol for 5 s.

- 2.2.7 Microscopy
- 2.2.8 Mechanical testing

2.11.2 IP-S/CNC/GBL with 13.0 wt% CNC

The experiments with the IP-S/CNC/GBL mixture with 13.0 wt% CNC were performed according to the following steps, which were performed as described in chapter 2.2 General photolithography steps, while in this section only deviations to the general protocol are mentioned:

- 2.2.1 Removal of the adsorbed water

After this step, some drops of the mixture were dripped on the wafer.

- 2.2.3 Soft baking (SB) (Figure 11 c,)

- 2.2.4 Exposure

A pillar array with 13 μm in diameter of each pillar was printed with laser powers from 12.5 to 27.5 mW. Furthermore, hexagons with wall widths from 0.5 to 5.0 μm were printed with a laser power of 25 mW to investigate the best resolution achievable. Samples for tensile testing were printed with a gauge section of 4x8x20 μm with different laser power from 15 to 30 mW. The other dimensions of the structures were listed in Table 2.

- 2.2.6 Development

The wafer was put into PGMEA in vertical position. The magnetic stirring caused a flow, which was directly against the surface of the wafer. This step was done until the unpolymerized parts detached. This took about 55 min. Then the wafer was rinsed with PGMEA and put in isopropanol for 5 s.

- 2.2.7 Microscopy

The images of the pillars were taken on a Hitachi TM3030 Plus.

- 2.2.8 Mechanical testing

2.11.3 IP-S/CNC/HEMA

The experiments with the IP-S/CNC/HEMA mixture with 5.0 wt% CNC were performed following the steps, which were performed as described in chapter 2.2 General photolithography steps, while in this section only deviations to the general protocol are mentioned:

- 2.2.1 Removal of the adsorbed water

After this step, some of the mixture was dripped on the wafer.

- 2.2.4 Exposure

A pillar array with 13 μm in diameter of each pillar was printed with laser powers from 15 to 32.5 mW. Furthermore, hexagons with wall widths from 0.5 to 5.0 μm were printed with a laser power of 25 mW to investigate the best resolution achievable. The other dimensions of the structures were listed in Table 2.

- 2.2.6 Development

The wafer was put into PGMEA in vertical position. The magnetic stirring caused a flow, which was directly against the surface of the wafer. This took about 5 min. Then the wafer was rinsed with PGMEA and put in isopropanol for 5 s.

- 2.2.7 Microscopy

3 Results and Discussion

In this chapter the results of the different lithography processes are given as well as the SEM images of the printed structures are discussed. The results of the micro compression are discussed too.

3.1 SU-8 2D Lithography

As SU-8 is a commonly used photoresist for 2D photolithography, the process worked very well. For the maskless projection system the optimal duration of exposure with an intensity of 26.5 mW/cm^2 (365 nm radiation) was 7.3 s. Figure 21 shows the microscopy image of this wafer. The squares shown in this image are 4x4 pixels and 3x3 pixels, the lines are 4 and 3 pixels, the size of 1 pixel is about $12 \mu\text{m}$. The gap between each of the structures should be equal in dimensions as the squares and lines. For lower durations an undercut of the structures was recognizable due to insufficient polymerization, for longer durations a footing was recognizable, which is caused by reflection of the UV light at the surface of the silicon wafer. As the manufacturer of this machine only guarantees the 4x4 pixels as the best resolution achievable, no more tests to improve the resolution were performed.

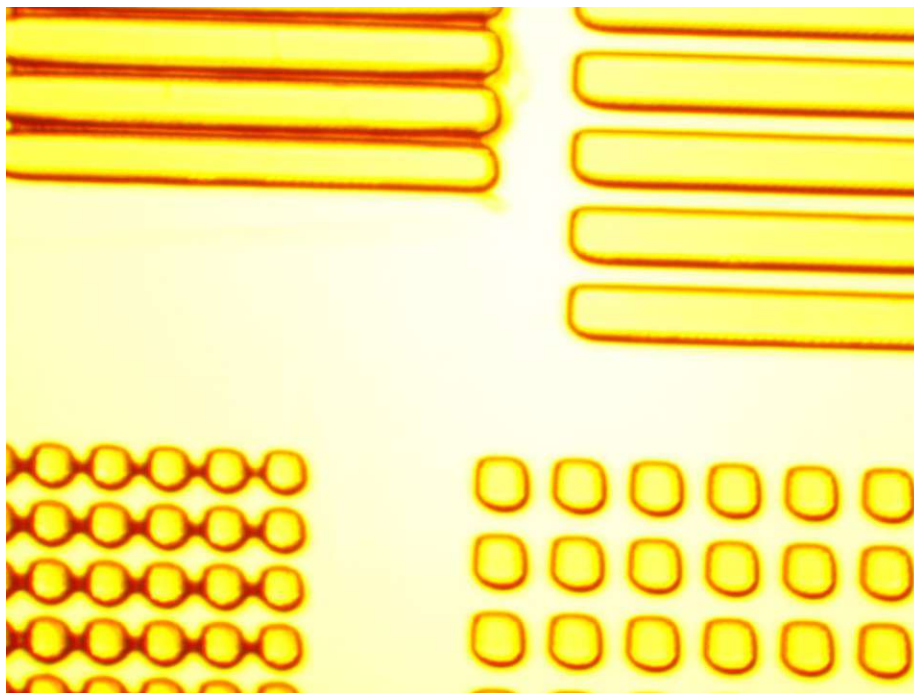


Figure 21: SU-8 dose and resolution test with the maskless projection system, 7.3 s

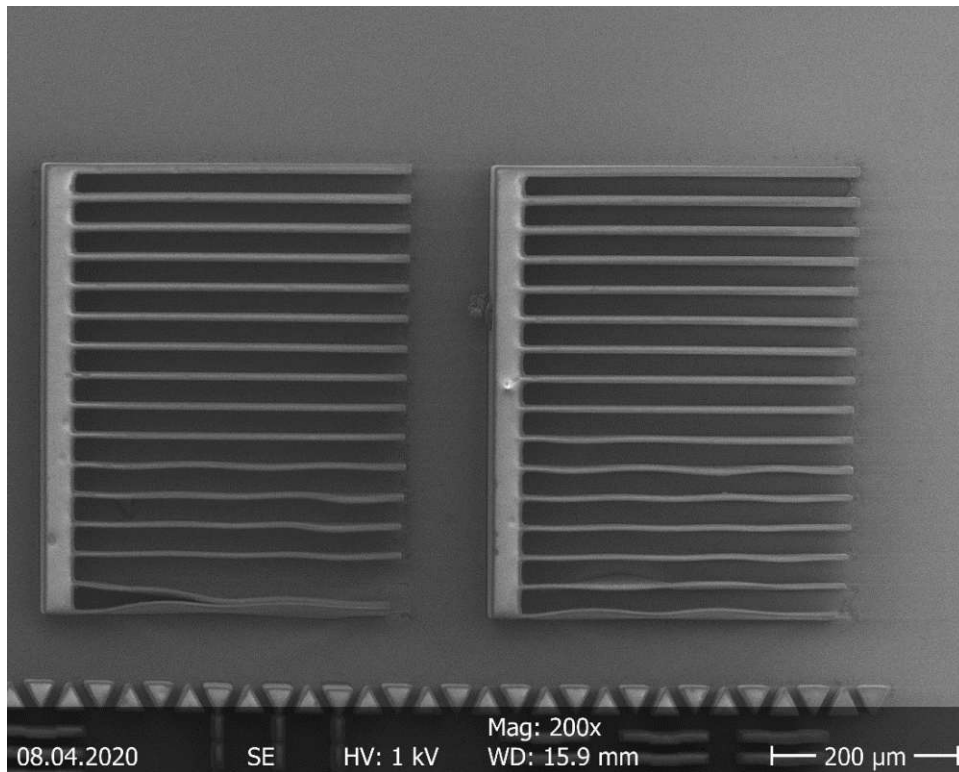


Figure 22: Section of the dose and resolution test on the direct laser printer; section with printing parameters of 60 % laser power (about 2.2 mW/cm^2) and defocus +15

The dose and resolution test for the direct laser writer showed, that the best parameter are 60 % laser power (about 2.2 mW/cm^2) and a defocus of +15 (Figure 22). This section shows lines with different thickness from 4 to 10 μm . The structures are about 40 μm in height, the thinnest lines, which are straight and good shaped, are 6.4 μm . In general, the sidewalls of the structures are straight and the development worked very well, as there is no unpolymerized resist left on the wafer. For the pattern with lower laser power the polymerization was not sufficient, which was recognizable as they were rinsed away during development. For the pattern with a lower defocus, the shape of the pattern showed non-parallel walls. The thickness of the walls was smaller for the top than for the bottom, as the focal spot of the laser gets closer to the wafer with decreasing defocus.

With the parameters of the dose test (60 % laser power and +15 defocus), the structures for mechanical testing were printed. Figure 23 shows SEM images of the thinnest structures of each type. As one can see, the walls are well shaped and there is only a little footing. The development of the structures worked very well, because there is no residue of the unpolymerized SU-8 on the wafer inside or outside of the structures.

The exact height and diameter of the structures were measured on the SEM. The values of the top surface area of the hexagons and honeycombs were converted into equivalent areas of circles, which were used to calculate equivalent pillar diameters for the processing of the load-displacement-curves. The measured and calculated dimensions are shown in Table 9, the mechanical properties are shown in Table 10.

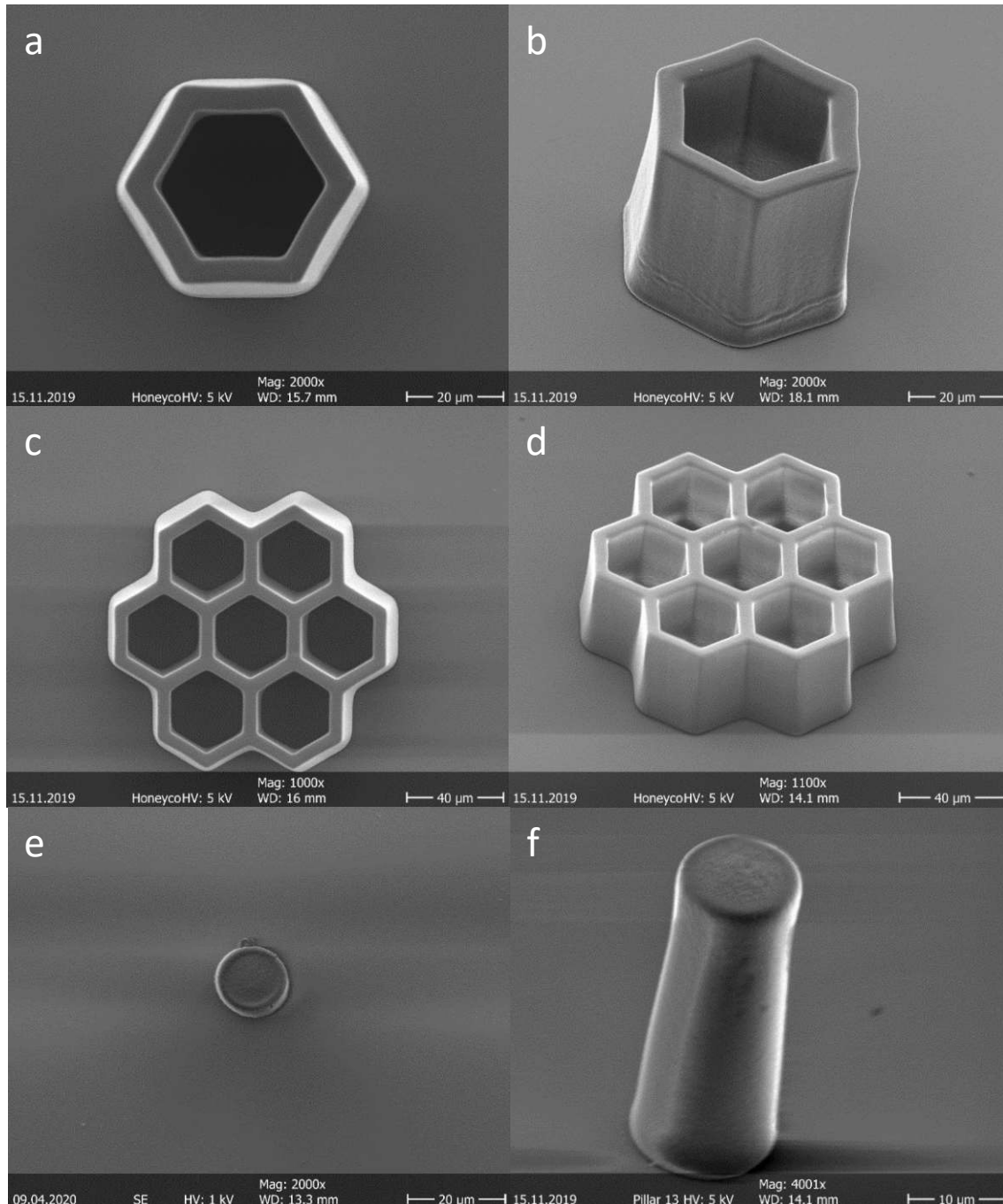


Figure 23: SEM images of the structures for mechanical testing, SU-8 2D photolithography; a, hexagon with 5 μm wall width; b, hexagon with 5 μm wall width, 45° tilted; c, honeycombs with 5 μm wall width; d, honeycombs with 5 μm wall width, 45° tilted; e, pillar with 13 μm diameter; f, pillar with 13 μm diameter, 45° tilted

Table 9: Real dimensions of the SU-8 structures printed with the direct laser writer, measured on the SEM, in μm

Diameter of pillar	12.7	19.3	25.8
Height of pillar	39.3	41.7	41.9
Wall thickness of hexagon	5.07	7.49	9.50
Height of hexagon	43.0	42.0	44.1
Equivalent pillar diameter	29.2	34.4	37.6
Wall thickness of honeycomb	5.08	7.90	10.6
Height of honeycomb	41.4	40.8	40.8
Equivalent pillar diameter	65.4	78.5	87.4

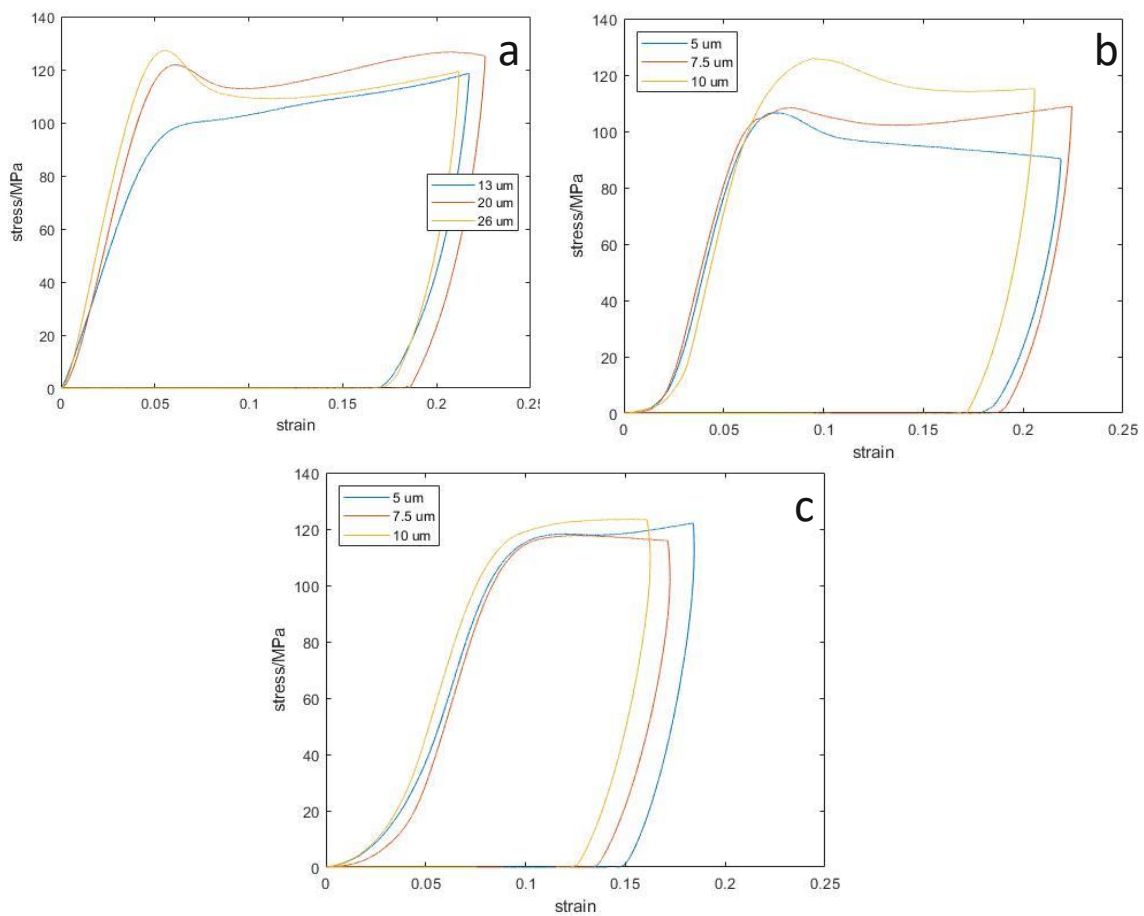


Figure 24: Stress-strain-curves of the micro compressions of: a, pillars, b, hexagons, c, honeycombs

The real diameters and thicknesses of the structures differ up to 6 % from the dimensions they should have. The height of the structures should be the same for all structures, but it is varying from one type of structures to the others (up to 12 % difference). This is caused by the spin coating process. The radial forces during the spin coating differ from the middle of the wafer to the edge of it. This causes a gradient of resist thickness from the middle to the edge of the wafer. As all structures were printed on the same wafer and some of the structures were in the middle of the wafer and other more to the edge of it, meaning that the height of the structures varies with the location on the wafer.

The stress-strain-curves (Figure 24) show typical elastic deformation in the beginning, which transitions to plastic deformation. The curves of the hexagons and honeycombs show a non-linear region at small strains, which is due to a not perfectly flat top surface of the structures and due to misalignment between the top plane of the structures and the flat punch indenter tip.

The mechanical properties of each kind of structure do not scatter very much which can be recognised on the low confidence interval of the extracted parameters. The deviations for the 12.7 μm pillar are the highest, which can be caused by the high aspect ratio of this pillar. A slight tilt of the pillar or a not perfect round shape of it can lead to buckling of the pillar, which leads to higher deviations in mechanical properties.

The yield stress and the Young's modulus are increasing with the thickness of the structures, which can be explained by the fact, that the development solvents PGMEA and isopropanol also attack the polymerized parts, but much less than the unpolymerized. This would explain, why the thinner structures, which have a higher ratio of surface to volume, have worse mechanical properties compared to the thicker ones. Another reason for the differences in mechanical properties could be based on the calculation of the top surface of the hexagons and honeycombs. As the corners of the structures are not perfect shaped, there is a small difference compared to the calculated top surface area, which supposes perfect shaped edges.

Table 10: Data from the compression tests of the SU-8 structures, the dispersion is given for a confidence level of 95 %

	Diameter (Pillar) / wall width (hexagons, honeycombs), μm	Yield stress, MPa	Young's modulus, GPa	Number of samples
Pillars	12.7	110 ± 11	2.43 ± 0.50	8
	19.3	120 ± 2	2.95 ± 0.15	8
	25.8	124 ± 3	3.23 ± 0.15	8
Hexagons	5.07	105 ± 5	2.67 ± 0.24	8
	7.49	108 ± 3	2.76 ± 0.08	8
	9.50	123 ± 2	2.92 ± 0.11	8
Honeycombs	5.08	116 ± 6	2.18 ± 0.21	8
	7.90	117 ± 4	2.31 ± 0.16	8
	10.6	119 ± 2	2.34 ± 0.09	8

3.2 SU-8/CNC composite 2D Lithography

For the maskless projection system the best resolution was achieved with 35 s of exposure. The best development was achieved by putting the wafer into PGMEA in vertical position with magnetic stirring, so that the flow was against the surface of the wafer. As there was still some residue on the wafer, it was sonicated in PGMEA for 30 s. During this step almost all unpolymerized parts detached. Unfortunately, some of the structures detached too.

The maximum resolution was 5x5 pixel, which is equal to 98x98 μm (Figure 25, upper left). The resolution was worse than with neat SU-8, which is caused by radiation scattering effects by the cellulose. The surface of the structures is not flat. A possible reason for this could be, that the solvent evaporated unevenly. Another reason could be that the CNC was not well dispersed in the resist and formed agglomerates, which could lead to inhomogeneous surfaces. The height of the structures was measured on the SEM and is between 70 and 80 μm . There is also a slight undercut recognisable, which is strange. There is no change in the refractive index during exposure, as the resist is already solid before exposure. The scattering of the light would lead into footing and not into an undercut. One possible reason for this

undercut could be that the intensity of the UV-radiation is attenuated the whole way down to the surface of the wafer, so that it is not high enough for sufficient polymerization of the bottom edges of the structures. But as this phenomenon also occurred at longer exposure durations, this reason can be excluded.

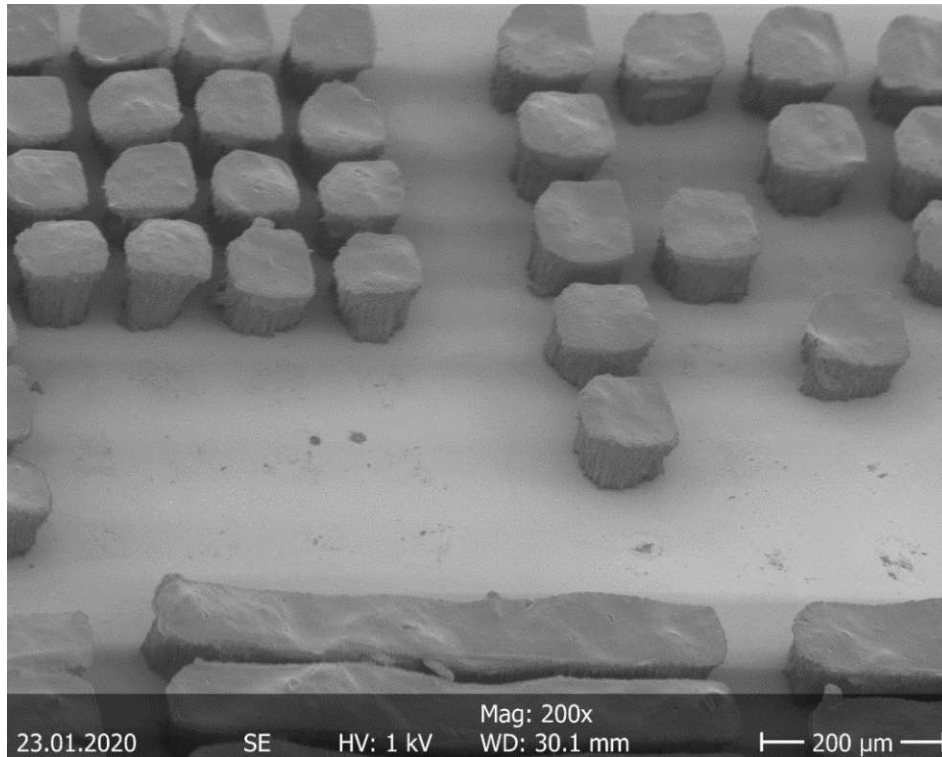


Figure 25: SU-8/CNC composite structures exposed with the maskless projection system

3.3 IP-S 2D Lithography

As the IP-S photoresist is not recommended for 2D lithography, the results are very poor. Due to the change in refractive index during polymerization, the radiation is deflected and a huge undercut occurs. As a result, the smaller structures buckled sideways. This is shown in Figure 26. There is a connection recognisable between the lines, which is likely caused by the interferences of the incoming beam and the beam, which is reflected on the surface of the wafer. These interferences also caused the standing waves, which can be seen at the side walls of the lines. The reason of this phenomenon is probably a smaller UV-absorption coefficient of IP-S in comparison to SU-8, which does not show this phenomenon. The best duration of exposure was 50 s. If the duration was longer, the structures detached from the wafer. If the duration was shorter, the resist was too soft and the pattern detached during development.

The height of the structures was measured on a SEM and was about 95 μm . The dimensions of the pillars in Figure 26 a, and c, are 90x83 μm .

It was observed, that the soft baking had no negative effect on the process. The results were quite contrary to this assumption. Without soft baking more of the structures detached during development. As the other steps of the process were the same for the samples with and without soft baking, this difference must be caused by the soft baking. But as the composition of IP-S is not known, the reasons for this cannot be identified.

There was no big difference recognisable with using different substrate materials (Figure 26 a, and b, glass wafer; c, silicon wafer).

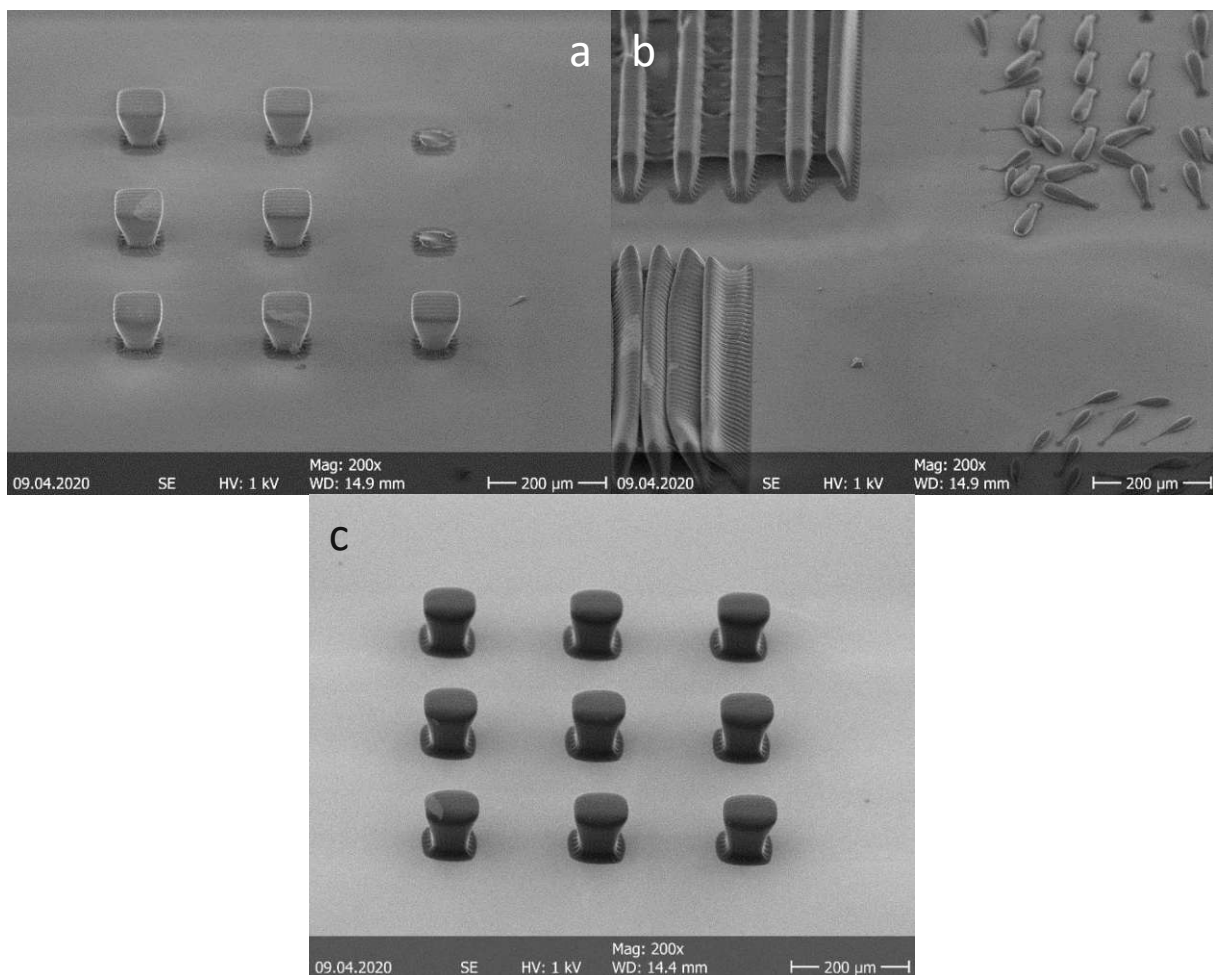


Figure 26: IP-S structures exposed with the maskless projection system, substrates: a, and b, glass wafer; c, silicon wafer

3.4 IP-S/CNC composite 2D Lithography

All results and discussions in this chapter are from the experiments with the IP-S/CNC/GBL mixture with 4.5 wt% CNC.

In general, the shape of the structures in Figure 27 is worse than for the SU-8/CNC/GBL mixture. The surface of the pillars is very rough and the square shape is only recognizable at the very top. The resolution of the pattern is comparable with the resolution of neat IP-S. The phenomenon of an undercut due to the change of refractive index like with neat IP-S can be observed too, but not that distinct. These pillars are the ones with the best resolution achieved and are $105 \times 105 \mu\text{m}$. The height of the pattern is $90 - 95 \mu\text{m}$. The only recognisable difference between the glass wafer (Figure 27 a, and b,) and the silicon wafer (Figure 27 c,) is the worse development step with the silicon wafer. The best development was achieved by putting the wafers in vertical position into PMGEA, while magnetic stirring caused a flow directly against the surface of the wafer.

As the main purpose of this experiment was the investigation, if this mixture is printable at all, no further process development was done.

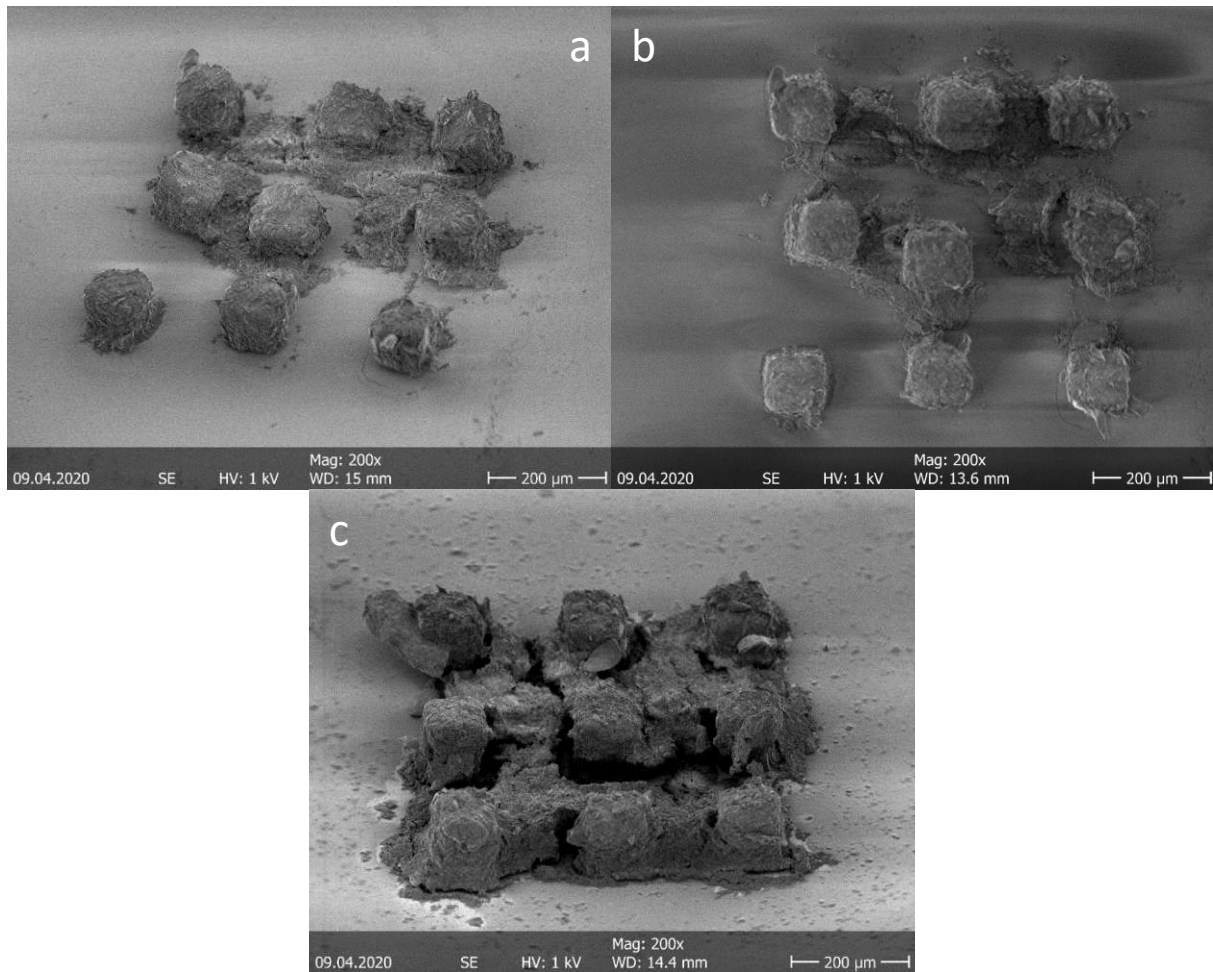


Figure 27: Structures made of IP-S/CNC/GBL with 4.5 wt% CNC exposed with the maskless projection system, substrates: a, and b, glass wafer; c, silicon wafer

3.5 SU-8 3D Lithography

As SU-8 is used for two-photon-polymerization too, the expectations on the shape of the pillars were quite high. The first experiments of 3D lithography with neat SU-8 were done without adhesion promoter, but during the development all structures detached. With the TI Prime Adhesion Promoter, the pillars did not detach during development.

Figure 28 shows pillars printed with different laser power. The exact dimensions of the pillars were measured on a SEM and are shown in Table 11. The data gained from mechanical testing is shown in Table 11 too.

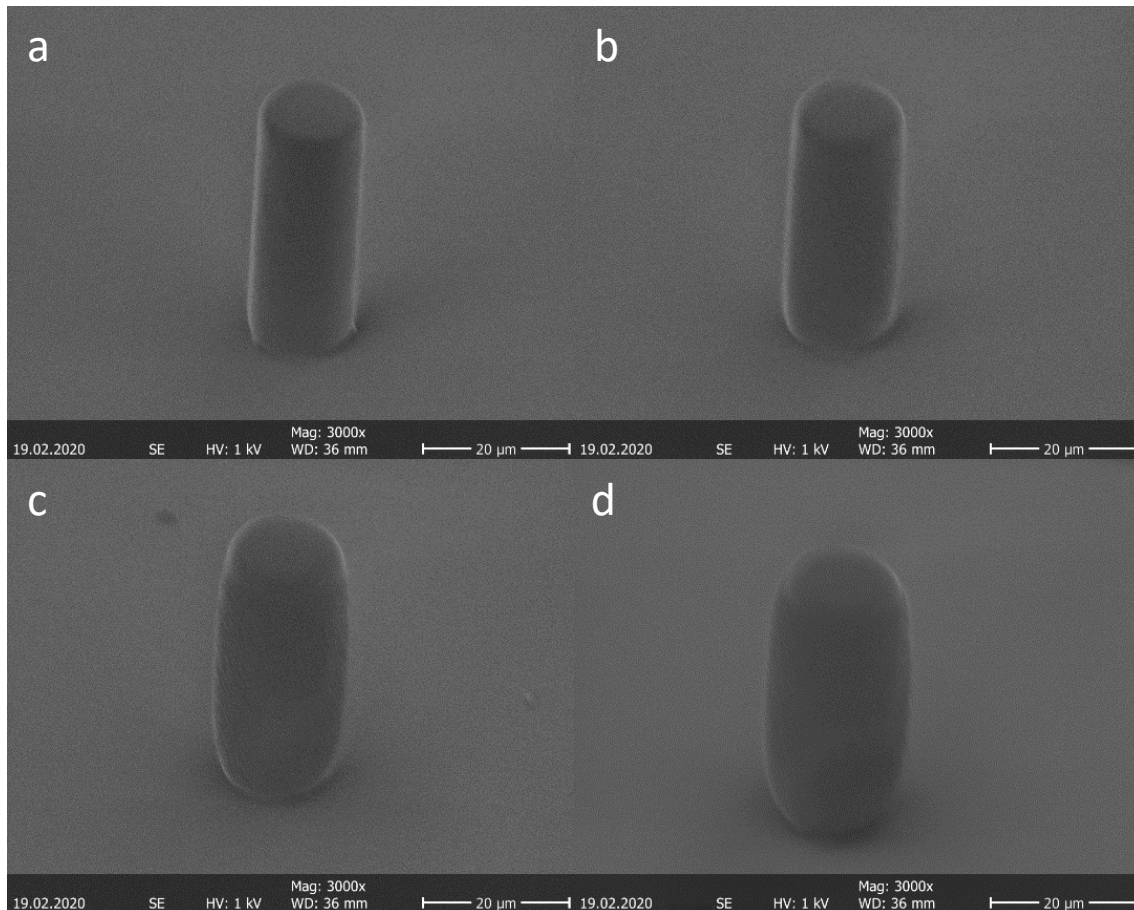


Figure 28: SU-8 pillars with 13 μm in diameter and 40 μm in height printed with different laser power: a, 12 mW, b, 15 mW, c, 20 mW, d, 25.5 mW

As it was for SU-8 2D lithography, the development worked very well, the dimensions differ up to 17 % in diameter and up to 6 % in height from the theoretical values. With increasing laser power, the shape of the pillars changed from straight sidewalls to more convex formed side walls. As the SU-8 is already solid before printing, it cannot be caused by a change in the diffraction index. In general, the diameter of the pillars rises with the laser power, which can be explained by an increase of the voxel size of the focal spot. The convex form of the pillars is most likely caused by overexposure. As the voxel size of the focal spot increases with the laser power, the overlapping volume of the scanning laser beam is increasing too. This leads to more and more laser power in the middle section of the pillar compared to the top and the bottom of it resulting in the convex shape.

The stress-strain-curves look typically for polymers (Figure 29). At the beginning elastic deformation happens, which is followed by plastic deformation. As the confidence intervals of the mechanical properties are very low, the properties of the different pillars are very

similar and the process can be seen as reproducible. The results of the micropillar compressions show, that the yield stress is quite independent on the laser power from 14 to 20 mW, but it increases by 10 % from 20 to 23.5 mW laser power. One reason for this could be a higher degree of cross-linking in the polymer with a higher laser power. The yield stress of the pillar printed with 23.5 mW laser power is also similar to the yield stress of the pillars printed by 2D photolithography (chapter 3.1 SU-8 2D Lithography). Another reason for the increasing of the yield stress with the laser power can be an error in the measurement of the pillar diameters due to the convex shape of them. The Young's modulus also changes with the laser power, but there is no trend recognisable. The Young's modulus of these pillars is lower than the Young's modulus of the pillars printed by 2D photolithography.

Table 11: Dimensions and mechanical properties of the SU-8 micropillars printed with different laser power; the dispersion is given for a confidence level of 95 %

Laser power, mW	Diameter, μm	Height, μm	Yield stress, MPa	Young's modulus, GPa	Number of samples
14	14.4	39.4	99.3 ± 3.3	2.07 ± 0.24	8
20	15.3	40.5	99.8 ± 1.7	1.91 ± 0.07	8
23.5	15.2	42.3	110 ± 5	2.15 ± 0.12	8

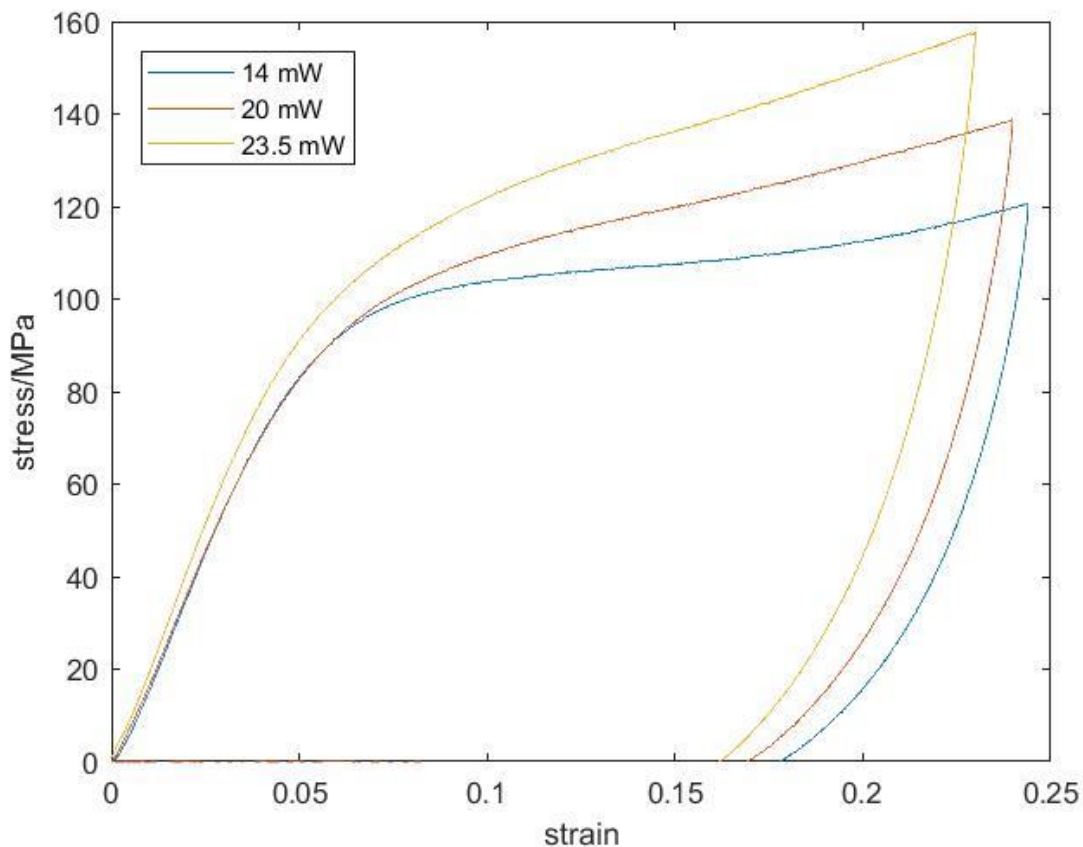


Figure 29: Stress-strain-curves of SU-8 pillar compressions, pillars printed with different laser power

3.6 SU-8/CNC composite 3D Lithography

The first experiments with the SU-8/CNC composite were done without adhesion promoter, but during development all the structures detached. With TI Prime Adhesion Promoter, this did not happen that much, but still about 40 % of the pillars detached.

Pillars printed with different laser power are shown in Figure 30. The development did not work perfect, as there is still some residue on the wafer and on the surface of the pillars. This can be explained by the insolubility of cellulose in the developing agent. Unlike the shape of the neat SU-8 pillars, the shape of the SU-8/CNC pillars did not change with the laser power. The real dimensions of the pillars were measured on a SEM and are shown in Table 12 as well as the mechanical properties. The stress-strain-curves of neat SU-8 and the SU-8/CNC composite pillar compressions are shown in Figure 31.

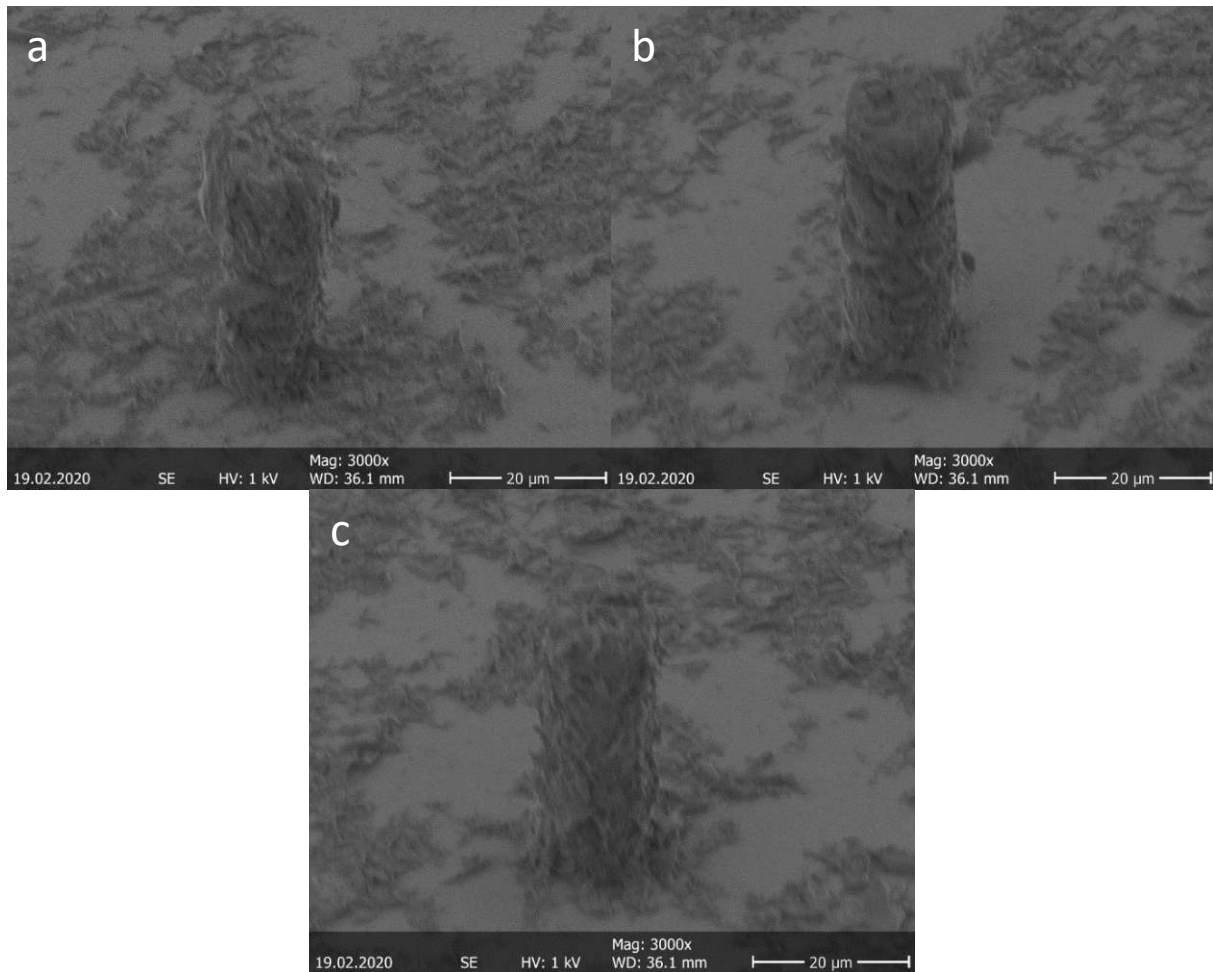


Figure 30: Pillars of SU-8/CNC/GBL mixture printed with 13 μm in diameter and 40 μm in height, printed with different laser power: a, 14 mW b, 20 mW; c, 23.5 mW

The dimensions of the pillars increase slightly with the laser power, which is the same with neat SU-8 and could be caused by the increasing voxel size of the focal spot. The real dimensions differ up to 14 % in diameter and up to 3 % in height. There is also a trend of increasing mechanical properties with the laser power, which is similar to neat SU-8 and could be caused by a higher degree of polymerization.

If yield stress and Young's modulus of neat SU-8 and of the SU-8/CNC composite are compared, one can see that both decreased drastically by adding CNC to SU-8, which seems to be curious at first view. A possible reason for this decrease in mechanical properties could be the introduction of water into the mixture before polymerization. If an epoxy resin gets in contact with water, it reacts to a diol (Figure 32). This would lead to a decrease in epoxy groups and in further consequence to a decrease of cross-linking, as there are less functional groups left, which can polymerize. As the CNC source was a gel of CNC in water, it could be possible,

that the solvent exchange steps were not sufficient and not all of the water was exchanged. Another reason could be, that there was some water in the GBL. The purity of GBL used in this thesis was $\geq 99\%$, but as GBL is hygroscopic, there is a possibility that the GBL absorbed water from the air during processing the mixtures. To ensure this assumption, the experiment would have to be done with a water-free CNC source, with water-free GBL and under conditions, which minimize the possibility of absorbing water.

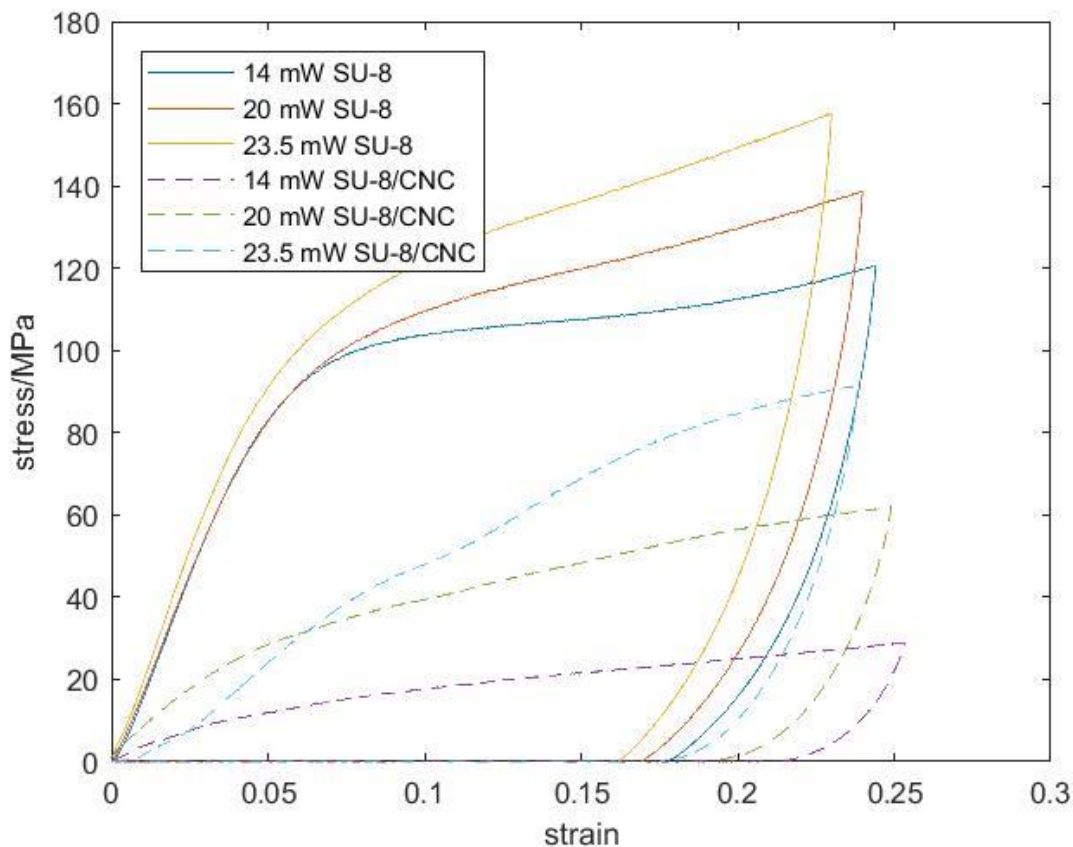


Figure 31: Stress-strain-curves of SU-8/CNC/GBL and neat SU-8 pillar compressions, pillars printed with different laser power

Table 12: Dimensions and mechanical properties of the SU-8/CNC/GBL micropillars printed with different laser power; the dispersion is given for a confidence level of 95 %

Laser power, mW	Diameter, μm	Height, μm	Yield stress, MPa	Young's modulus, MPa	Number of samples
14	13.7	38.9	14.8 ± 7.0	316 ± 235	4
20	13.9	39.6	42.7 ± 26.9	744 ± 655	5
23.5	14.8	40.9	69.5 ± 19.6	930 ± 478	8

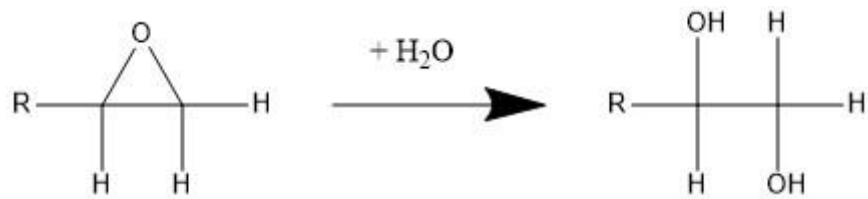


Figure 32: Formation of a diol out of an epoxy group and water

Figure 33 shows a hexagon in two different perspectives. The shape of the hexagon is clearly recognizable, but the development did not work properly, which was the same with the pillars. There is still some residue on the sidewalls and on the wafer inside and outside of the hexagon. The thickness of the wall was printed with 4 μm , the true thickness is 12 μm . This increase is likely due to the increase of the voxel size of the focal spot, which is caused by radiation scattering on the CNC. Hexagons with thinner walls were printed too, but their shape was not recognizable or they were rinsed away during development.

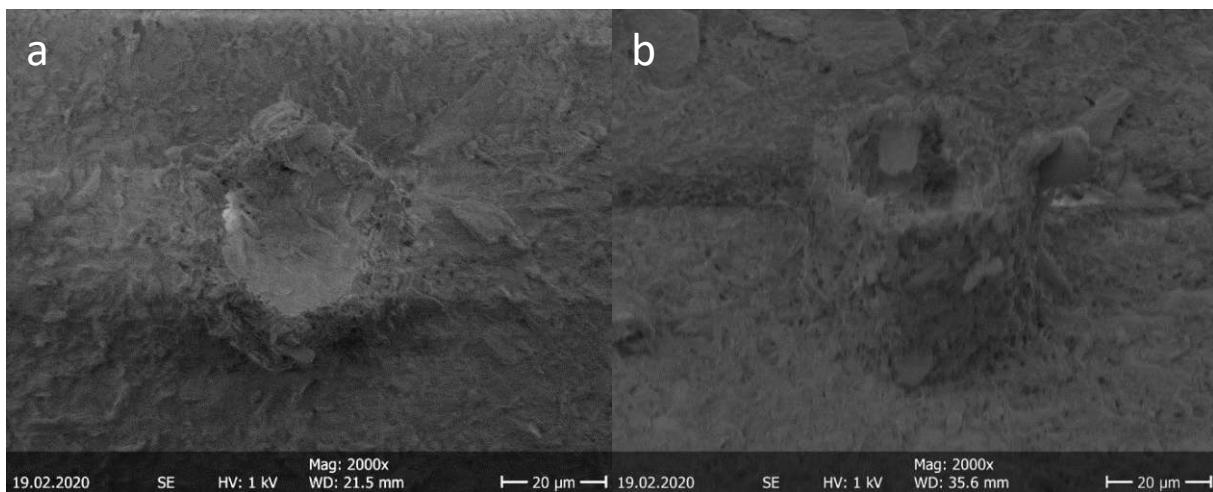


Figure 33: Hexagons printed with SU-8/CNC/GBL mixture with a wall thickness of 4 μm ;
a, top view; b, 45° tilted

3.7 IP-S 3D Lithography

As IP-S is particularly made for two-photon-polymerization, the process worked very well. The adhesion to the glass wafers was sufficient, so that the structures did not detach during development.

The shape of the pillars (Figure 34) is straight and no unpolymerized resist is left on the wafer or on the structures. On the surface of the pillars some texture is recognizable, which is caused by the laser, which is scanning the surface during printing. The exact dimensions of the pillars are measured on a SEM and shown in Table 13 as well as the mechanical properties.

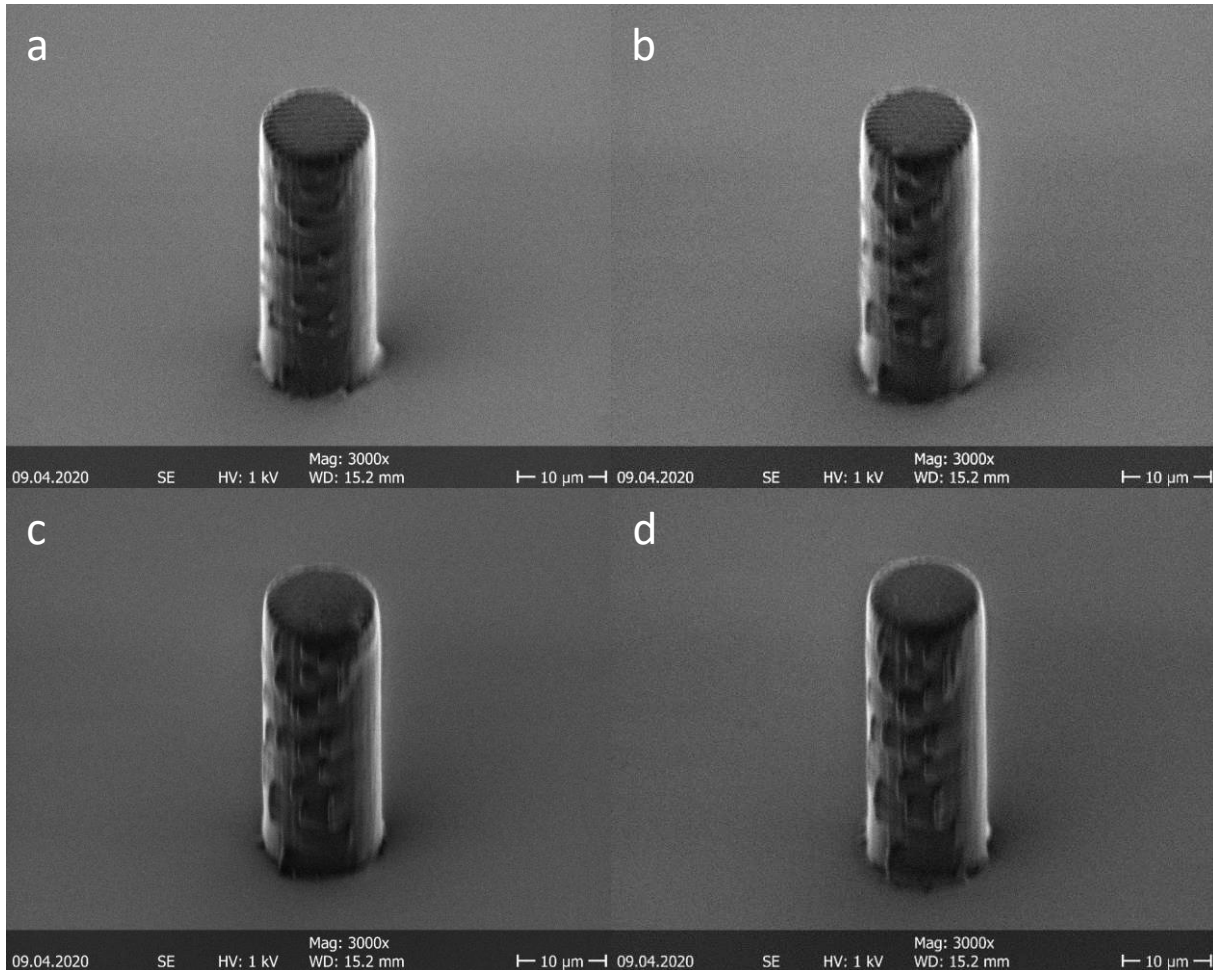


Figure 34: IP-S pillars printed with 13 μm in diameter and 40 μm in height, printed with different laser power: a, 12.5 mW; b, 17.5 mW; c, 22.5 mW; d, 27.5 mW

As one can see, the dimensions of the pillars increase with the laser power, which can be caused by an increase of the voxel size of the focal spot due to radiation scattering. The real dimensions differ up to 5 % in diameter and up to 4 % in height from the theoretical values. The shape of the pillars does not change with the laser power, as it was with neat SU-8 (Figure 28). The stress-strain-curves look typical for polymers (Figure 35). The elastic deformation in the beginning transitions into plastic deformation with strain hardening of the material.

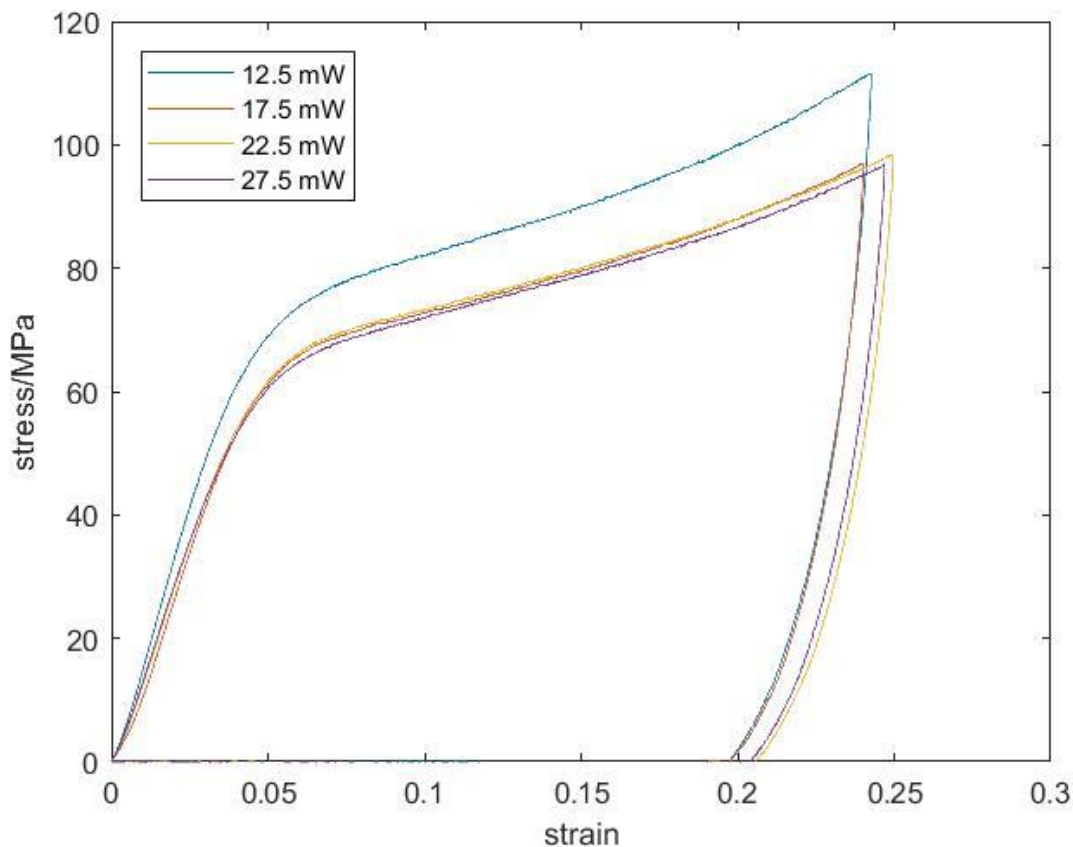


Figure 35: Stress-strain-curves of IP-S pillar compressions, pillars printed with different laser power

Table 13: Dimensions and mechanical properties of the IP-S micropillars printed with different laser power; the dispersion is given for a confidence level of 95 %

Laser power, mW	Diameter, μm	Height, μm	Yield stress, MPa	Young's modulus, GPa	Hardening modulus, MPa	Number of samples
12.5	12.8	38.5	80.6 ± 1.4	1.87 ± 0.41	155 ± 32	10
17.5	13.3	38.9	70.6 ± 7.2	1.55 ± 0.19	135 ± 44	5
22.5	13.6	38.6	70.4 ± 6.7	1.56 ± 0.14	139 ± 31	5
27.5	13.7	39.0	68.4 ± 6.7	1.57 ± 0.20	143 ± 36	5

The confidence intervals of yield stress and Young's modulus are relatively low, which means that the properties of the pillars are quite similar. The Yield stress decreases with the laser power, while the Young's modulus does not change significantly. Due to the high deviation of the Young's modulus for the 12.5 mW laser power pillars no certain conclusion about a trend

can be drawn. The hardening modulus does not change significantly with the laser power too. A possible reason for the decrease in yield stress could be a higher amount of initiator molecules, which get activated by the radiation. This would lead to a higher amount of polymer chains with a lower molecular weight and degree of polymerization (DP). This would explain the decrease in mechanical properties, as these are dependent on the DP [74]. If the curves of the 17.5 mW laser power and higher are compared, they are almost equal. This suggests that with 17.5 mW laser power all of the photoinitiator molecules have already been activated and thus no further decrease in mechanical properties with increasing laser power is recognizable.

Figure 36 a, and b, shows images of cellular structures. The struts are well shaped, but the top surface is not completely flat. The development worked very well, as there is no residue left inside the structure or outside on the wafer. Figure 36 c, and d, shows the structure after compression. The true dimensions of the structures and of the struts, as well as the data of the compression tests, are shown in Table 14, where the peak strength is related to the sum of the cross sections of the vertical pillars in the most upper layer. An exemplary stress-strain-curve is shown in Figure 37, which shows a linear elastic deformation part, followed by post-yield softening due to plastic buckling. [12], [75]

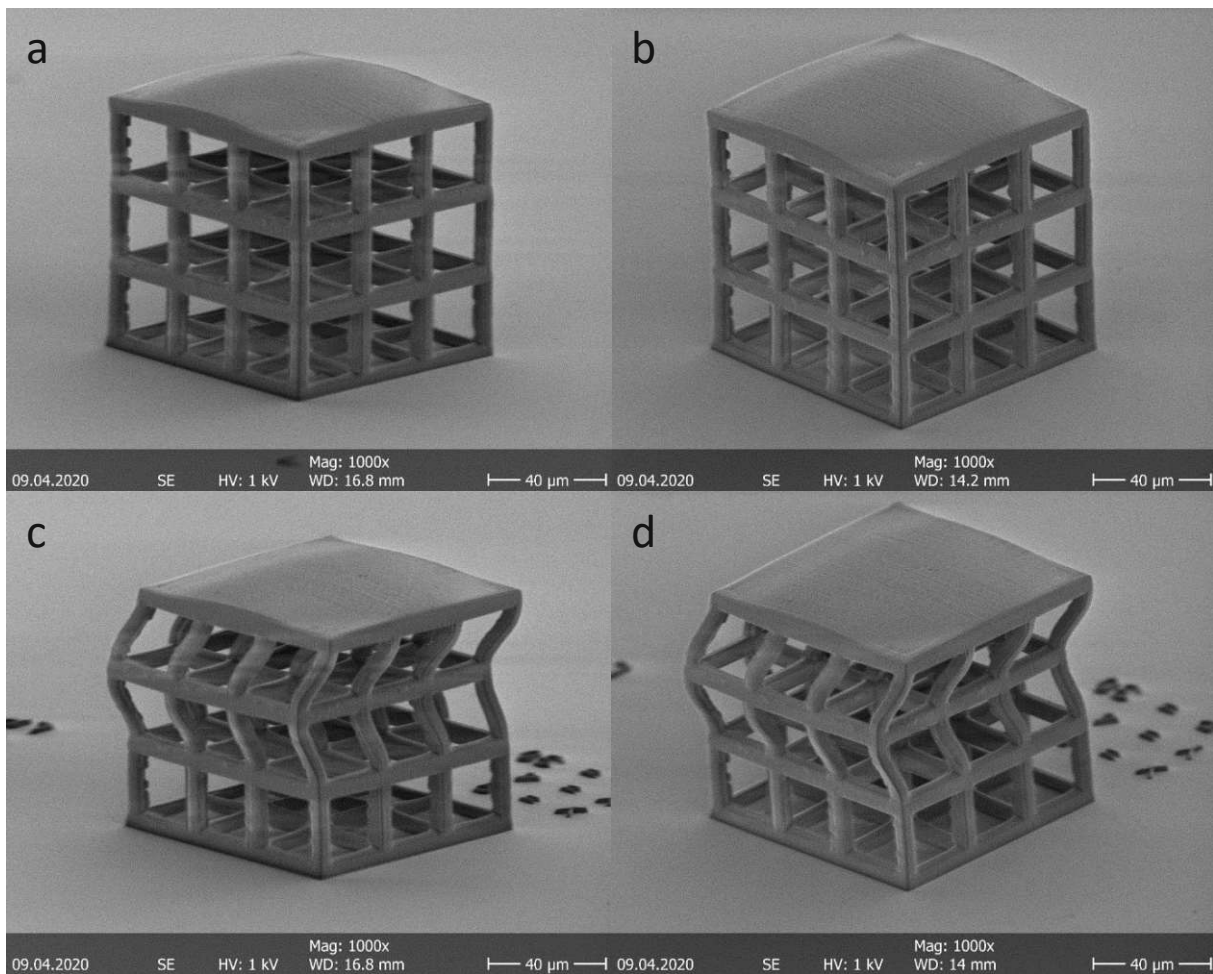


Figure 36: IP-S cellular structures, a, and b, before compression, c, and d, after compression

The deformation of the cellular structure occurred only in the top and the middle layer of cells. The deformation mechanism of the struts is plastic buckling, there is no brittle behaviour recognizable. If the peak strength of the cellular structures is compared with the yield stress from the pillar compression, the values are very similar and are in the confidence interval. The peak strength confidence interval of the cellular structures is higher than for the pillars. This can be explained by the relatively thin struts, where the same absolute deviation in thickness has a greater influence, as the properties of the whole cellular structure get weaker, if only a few struts get weaker.

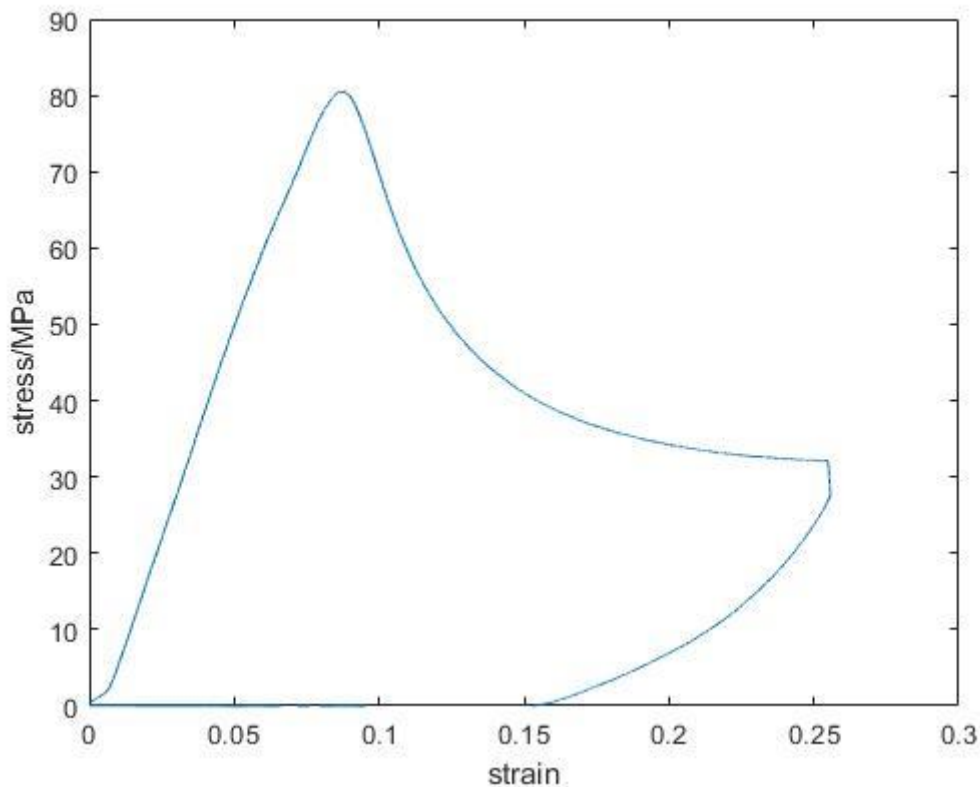


Figure 37: Stress-strain-curve of the IP-S cellular structures

Table 14: Dimensions and mechanical properties of the IP-S cellular structures; the dispersion is given for a confidence level of 95 %

Laser power, mW	Strut thickness, μm	Dimensions of the structure, μm	Peak strength, MPa	Number of samples
15	4.5	92	79.6 ± 13.7	8

Figure 38 shows tensile samples printed with different laser power. The shape of the samples is very good, the development worked very well. At the left tensile sample, which was printed with 15 mW laser power, the texture of the laser, which scanned the geometry during printing, is recognizable. The exact dimensions of the gauge section were measured on a SEM and shown in Table 15 as well as the mechanical properties. The stress-strain-curves are shown in Figure 39.

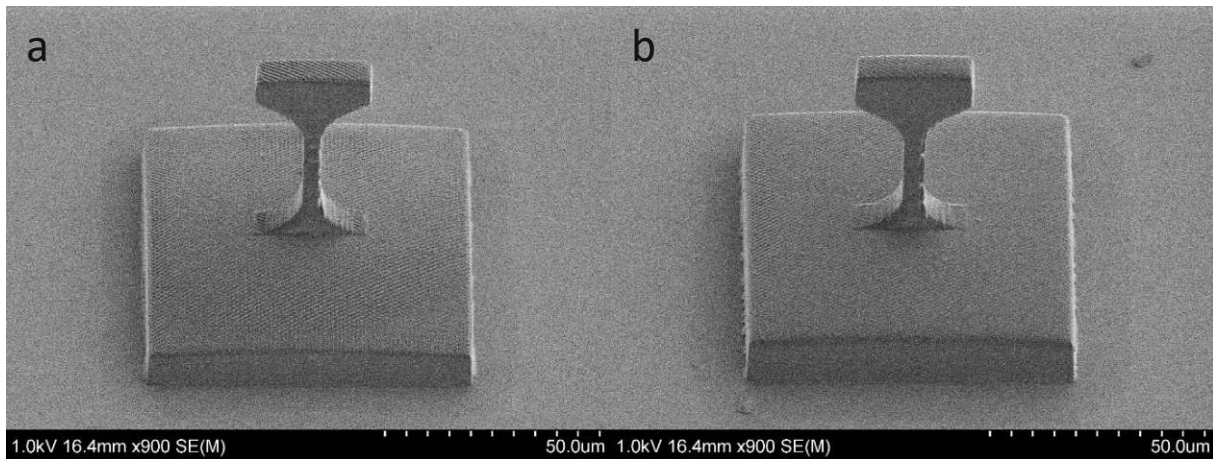


Figure 38: IP-S tensile samples, printed with different laser power: a, 15 mW, b, 30 mW

As it was with the pillars, the dimensions of the gauge section increased with the laser power and differ up to 25 % in cross section from the theoretical value. Yield stress and elastic modulus seem to increase with laser power, but as only one test for 15 mW laser power and two tests for each of the other two laser powers were performed, the values have to be treated with caution. And due to the SARS-CoV-2 pandemic in 2020, which happened during the time this thesis was carried out, no more samples could be tested.

Table 15: Dimensions and mechanical properties of the IP-S tensile samples printed with different laser power

Laser power, mW	Dimensions of gauge section, μm	Yield stress, MPa	Young's modulus, GPa	Number of samples
15	4.20x8.20	64.8	2.32	1
25	4.30x8.30	68.1	2.46	2
30	4.70x8.50	74.0	2.61	2

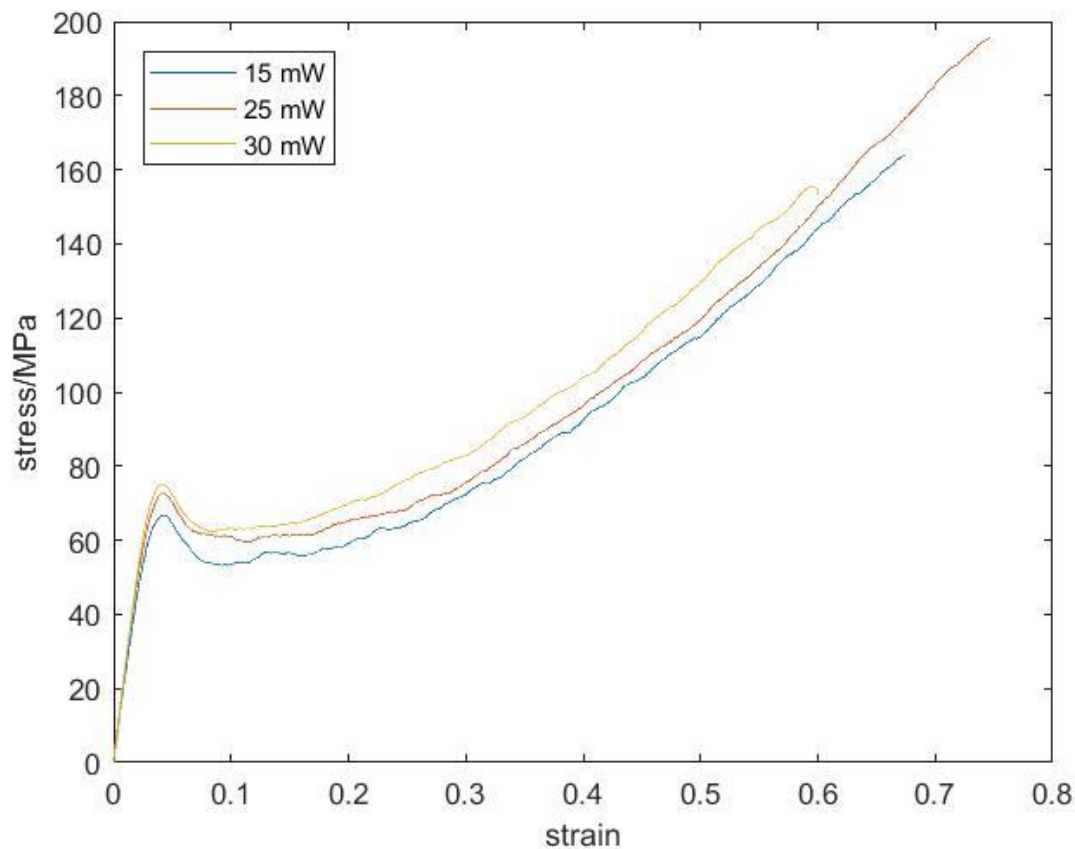


Figure 39: Stress-strain-curves of the IP-S tensile samples, printed with different laser power

3.8 IP-S/CNC composite 3D Lithography

3.8.1 IP-S/CNC/GBL with 4.5 wt% CNC

The pillars printed with this mixture are shown in Figure 40. They are well shaped and the development worked well, as there is almost no residue left on the wafer or on the pillars. The shape of the pillars does not change with the laser power, but the dimensions slightly increase with the laser power. The true dimensions of the pillars are measured on a SEM and summarized in Table 16. The mechanical properties are shown in Table 16 too.

The real dimensions of the pillars do not differ a lot from the dimensions they should have. They differ up to 5 % in diameter and up to 3 % in height, which is very similar as for neat IP-S. The stress-strain-curves (Figure 41) show typical elastic deformation in the beginning, which transitions in plastic deformation with a strain hardening of the material. The yield stresses

do not scatter very much which can be recognised on the quite low deviations, but the deviations of the Young's moduli and the hardening moduli are quite high.

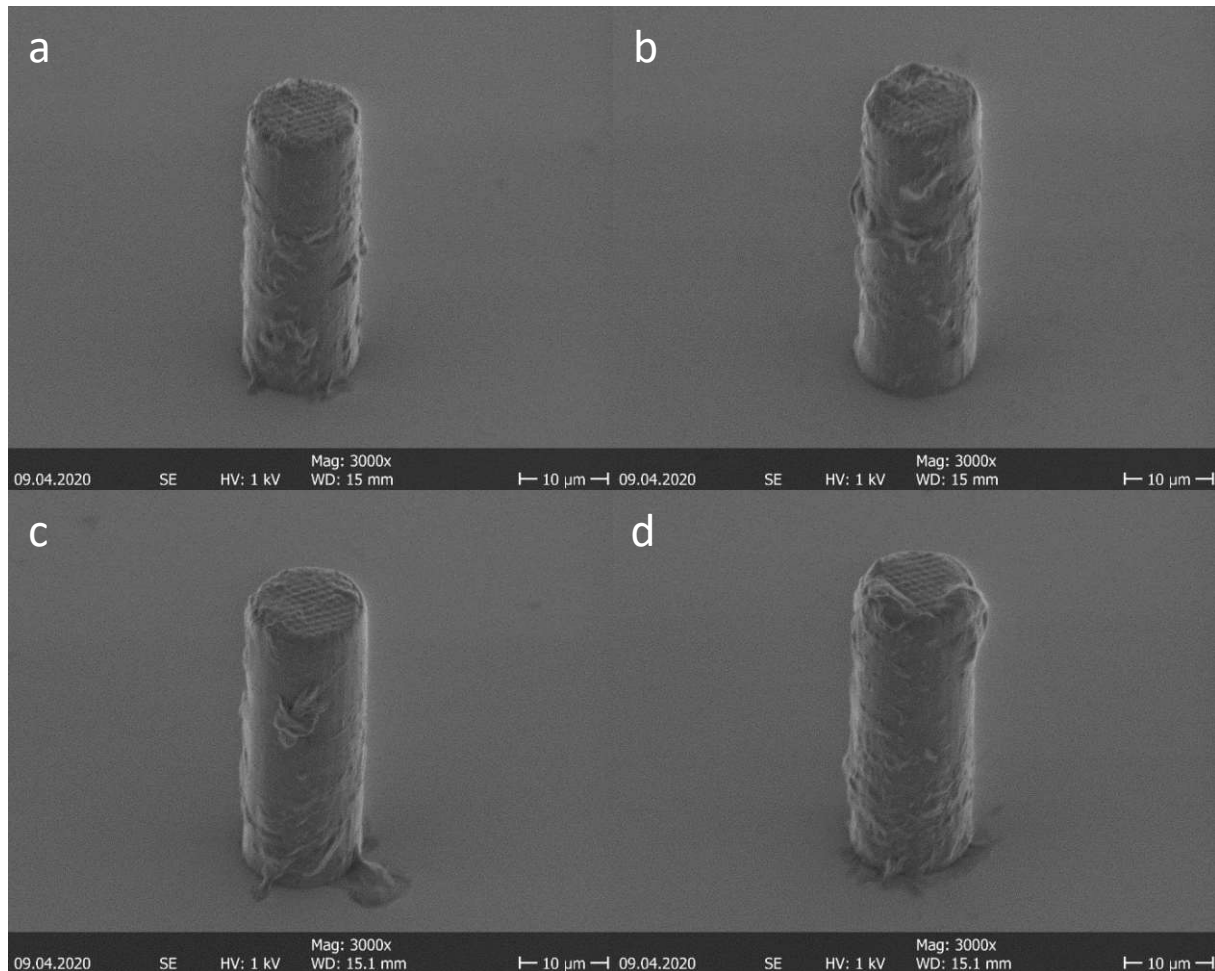


Figure 40: Pillars of 13 μm in diameter and 40 μm in height, printed with the IP-S/CNC/GBL mixture with 4.5 wt% CNC with different laser power: a, 12.5 mW, b, 17.5 mW, c, 22.5 mW, d, 27.5 mW

Table 16: Dimensions and mechanical properties of the IP-S/CNC micropillars with 4.5 wt% CNC printed with different laser power; the dispersion is given for a confidence level of 95 %

Laser power, mW	Diameter, μm	Height, μm	Yield stress, MPa	Young's modulus, GPa	Hardening modulus, MPa	Number of samples
12.5	13.0	38.8	109 ± 15	2.12 ± 0.95	245 ± 213	7
17.5	13.5	39.6	106 ± 18	2.21 ± 0.92	214 ± 78	9
22.5	13.4	40.1	105 ± 23	1.92 ± 1.49	336 ± 516	6
27.5	13.6	41.0	101 ± 19	2.12 ± 0.95	208 ± 173	8

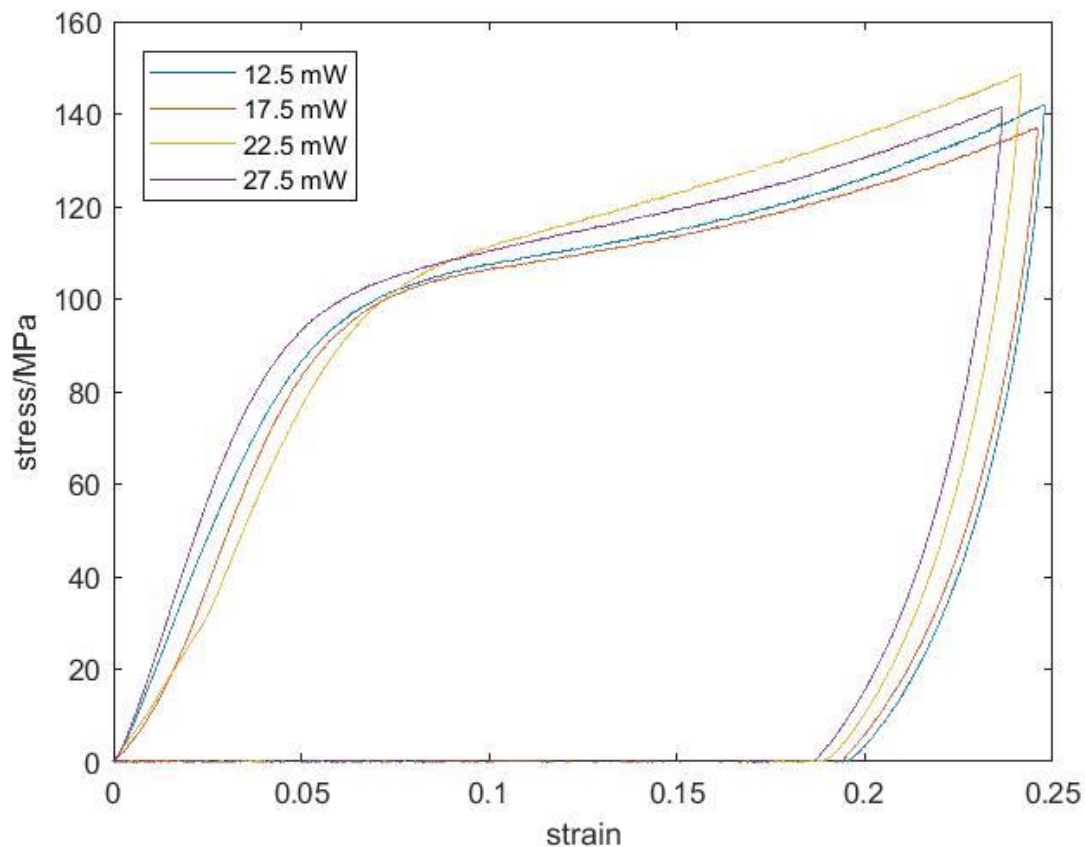


Figure 41: Stress-strain-curves of the IP-S/CNC/GBL pillar compressions; 4.5 wt% CNC; printed with different laser power

Figure 42 shows two hexagons in different perspectives. Their shape is good and the edges are sharp. The development worked well, as there is almost no residue left inside or outside of the hexagons on the wafer and on the side walls. The theoretical and the true dimensions of them are summarized in Table 17. As the theoretical wall thickness of the upper hexagon was only $0.5 \mu\text{m}$, which is only 1 laser beam, this is the best resolution achievable with this mixture for 25 mW laser power.

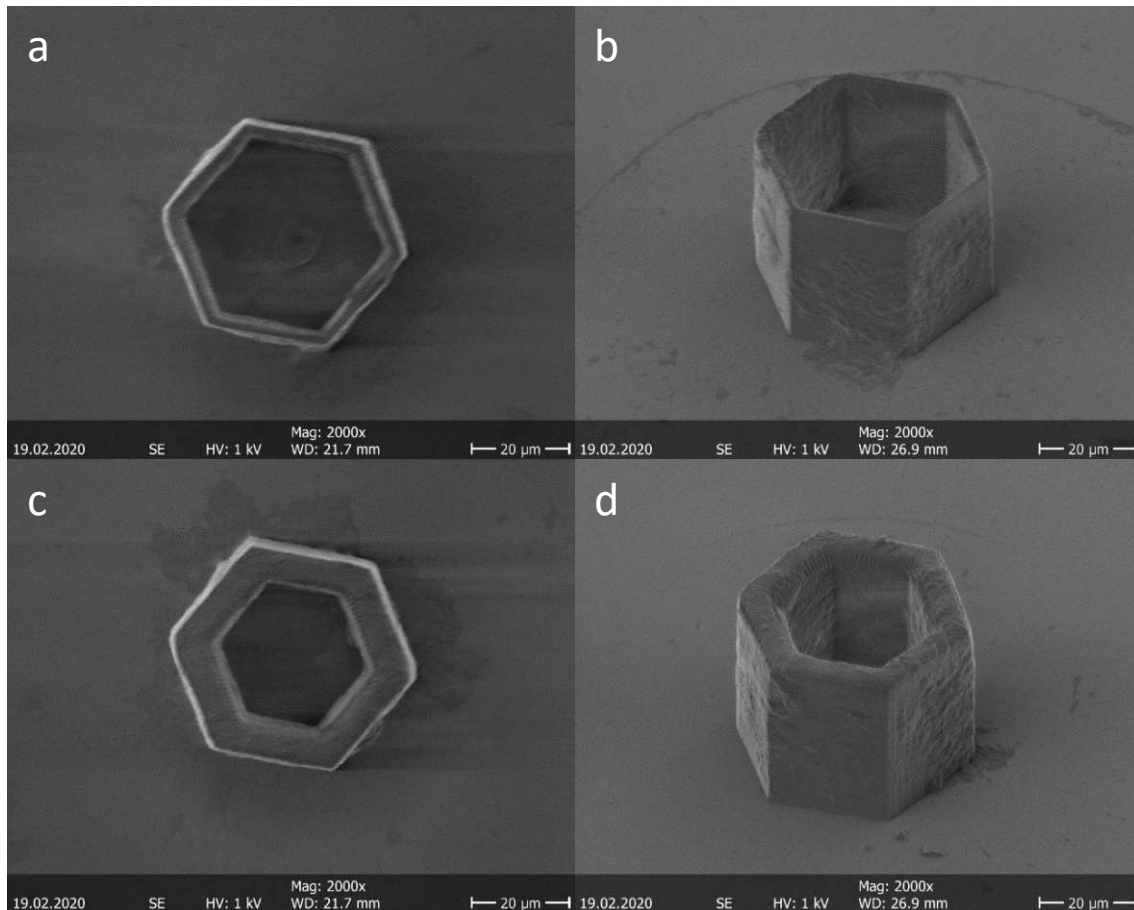


Figure 42: Hexagons printed with the IP-S/CNC/GBL mixture with 4.5 wt% CNC; the height is about 40 μm , the true wall width is: a, and b, 2.7 μm ; c, and d, 7.0 μm ; printed with 25 mW laser power

Table 17: Theoretical and true wall width of the hexagons in Figure 42

	Figure 42 a, and b,	Figure 42 c, and d,
Theoretical wall width	0.5	5.0
True wall width	2.7	7.0

The cellular structures are shown in Figure 43 (a, and b, before compression, c, and d, after compression). The shape of the structure is good, but the development worked not perfect, as there is still some residue left on the wafer and on the struts. Nevertheless, the structure is recognizable and the most of the unpolymerized parts were dissolved. The true dimensions of the structures and the struts were measured on a SEM and are summarized together with the peak strength in Table 18, which is related to the sum of the cross sections of the vertical pillars in the most upper layer. As the strut thickness of the structures decreases from the

bottom cells to the top cells, the calculations were performed for the lower strut thickness, which was the 5.25 μm in the upper cell layer. Figure 44 shows an exemplary stress-strain-curve.

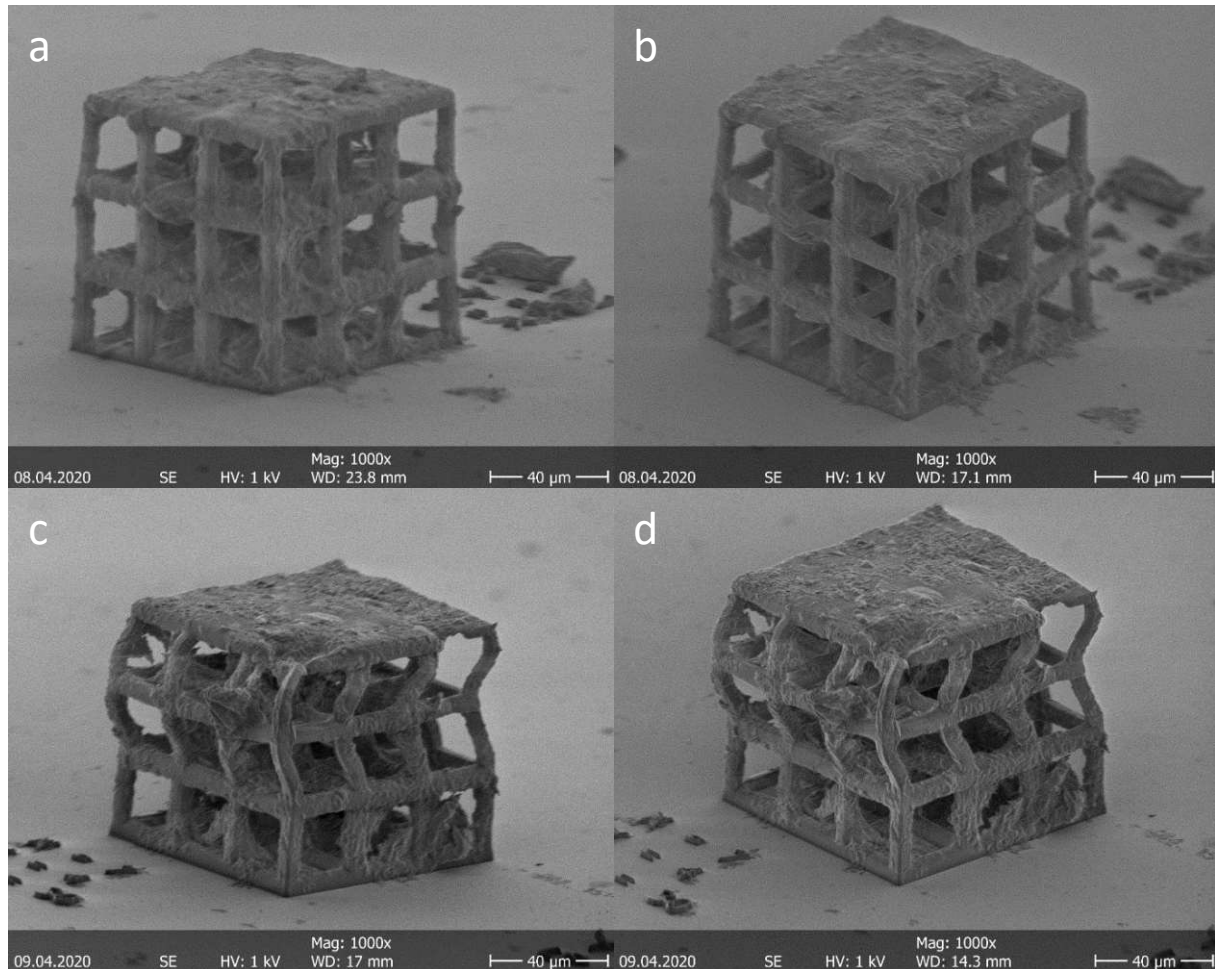


Figure 43: Cellular structures printed with the IP-S/CNC/GBL mixture with 4.5 wt% CNC, a, and b, before compression, c, and d, after compression

Table 18: Dimensions and mechanical properties of the IP-S/CNC/GBL cellular structures with 4.5 wt% CNC; the dispersion is given for a confidence level of 95 %

Laser power, mW	Top strut thickness, μm	Dimensions of the structure, μm	Peak strength, MPa	Number of samples
15	5.25	94	103 \pm 17	7

The deformation of the cellular structure occurred only in the top and the middle layer of cells, which is the same for cellular structures printed with neat IP-S. The deformation mechanism of the struts is plastic buckling, which is caused by post-yield softening[12], [75], there is no

brittle behaviour recognizable, which means that the material does not get more brittle by adding CNC. If the peak strength of the cellular structures is compared with the yield stress from the pillar compression, the values are very similar and are in the confidence interval, which militates for a uniform process. The peak strength confidence interval of the cellular structures is higher than for the pillars. This can be explained by the relatively thin struts, where the same absolute deviation in thickness has a greater influence, as the properties of the whole cellular structure get weaker, if only a few struts get weaker.

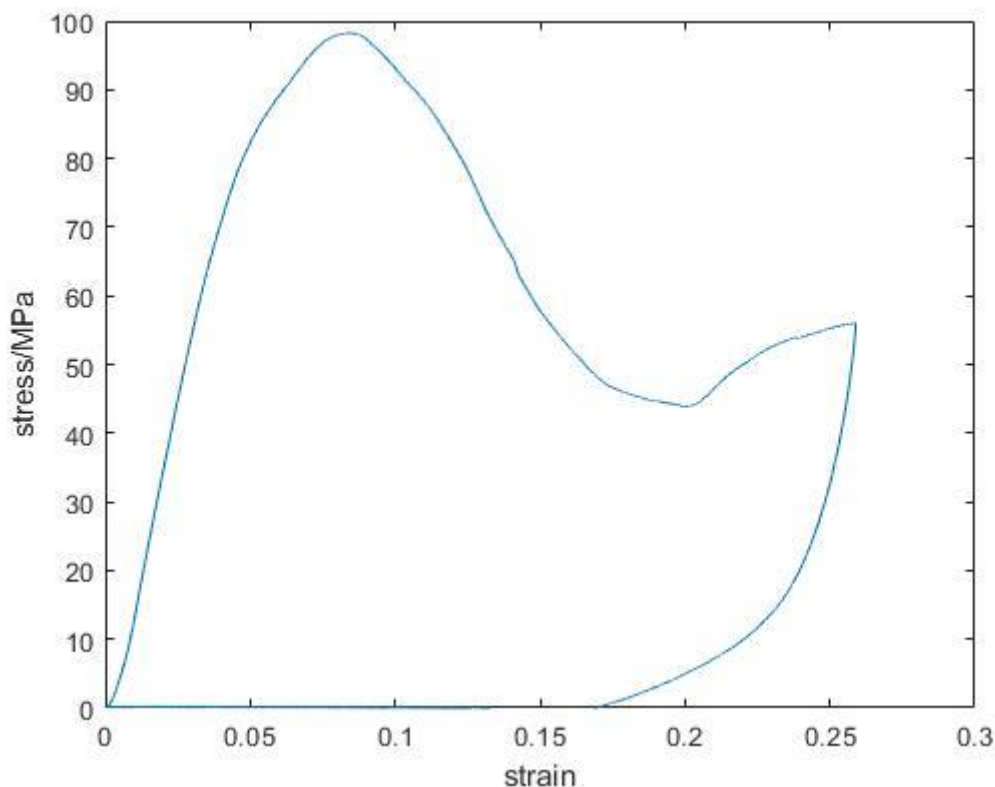


Figure 44: Stress-strain-curve of the IP-S/CNC/GBL cellular structure, 4.5 wt% CNC

Figure 45 shows tensile samples printed with different laser power. The shape of the samples is good, the development worked quite well. There is only a little bit of residue on the wafer and on the structure left. The exact dimensions of the gauge section were measured on a SEM and shown in Table 19 as well as the mechanical properties. The cross section of the gauge section differs 70 % from the theoretical value, which seems to be very much, but as the theoretical dimensions are only $4 \times 8 \mu\text{m}$ in cross section, the absolute difference is not very high. An exemplary stress-strain-curve is shown in Figure 46.

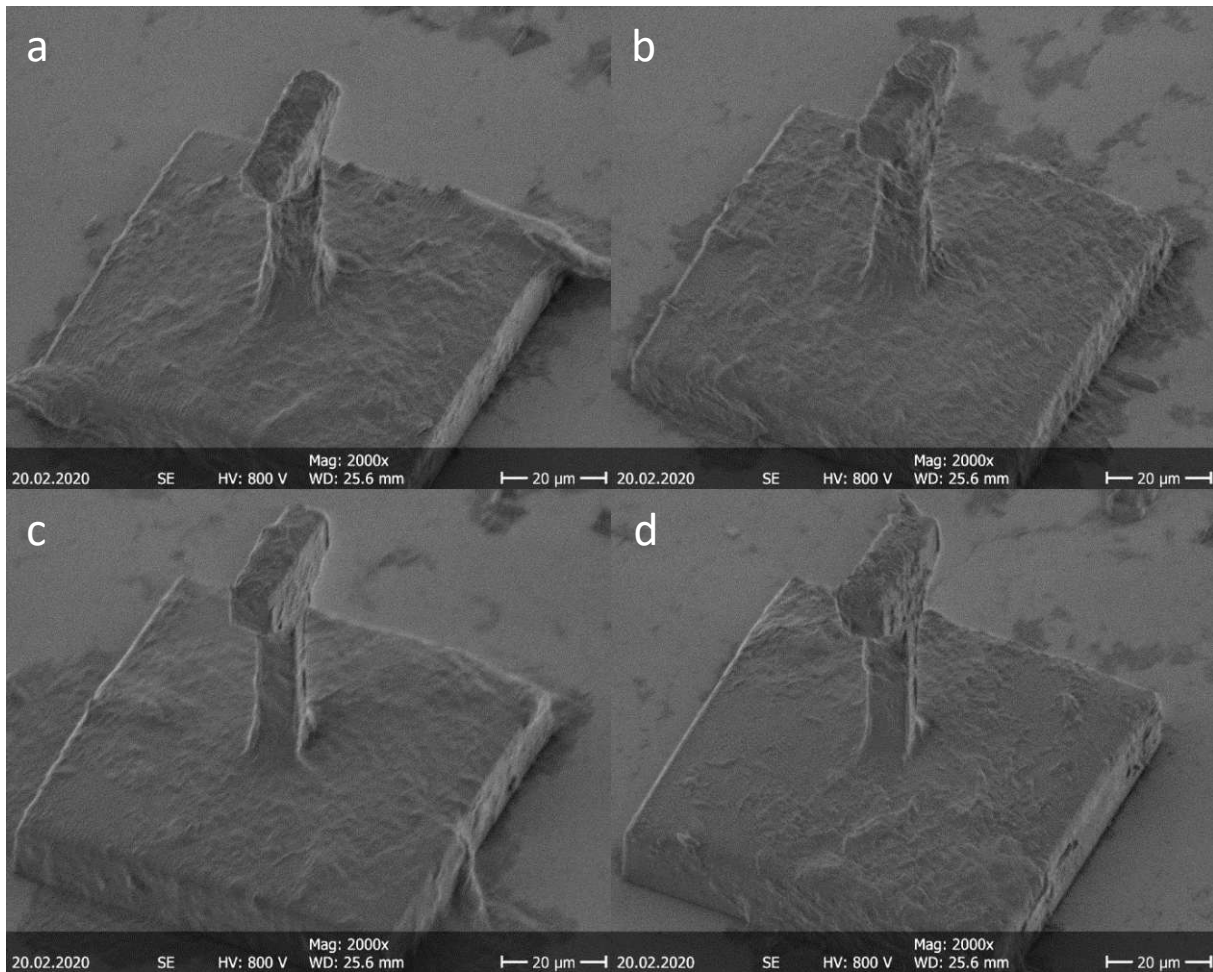


Figure 45: Tensile samples printed with the IP-S/CNC/GBL mixture with 4.5 wt% CNC and with different laser power: a, 15 mW; b, 20 mW; c, 25 mW, d, 30 mW

Table 19: Dimensions and mechanical properties of the IP-S/CNC tensile samples with 4.5 wt% CNC; the dispersion is given for a confidence level of 95 %

Laser power, mW	Dimensions of gauge section, μm	Yield stress, MPa	Peak stress, MPa	Young's modulus, GPa	Number of samples
15	5.75x9.48	58.9 ± 23.8	68.3 ± 22.6	2.92 ± 1.23	5

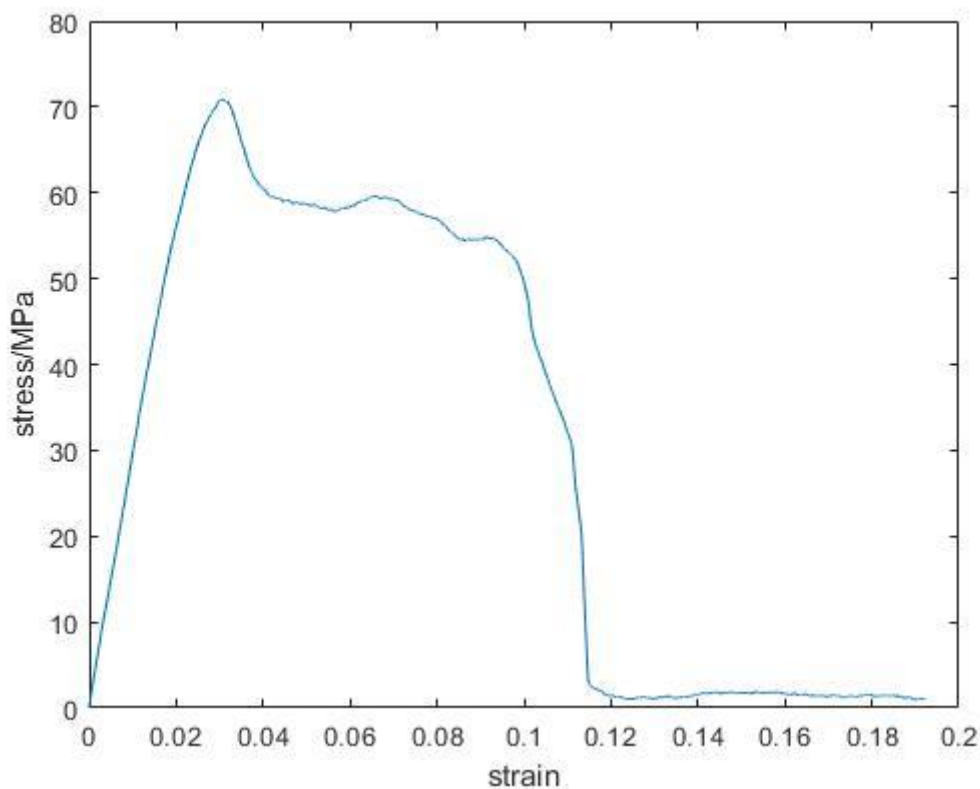


Figure 46: Stress-strain-curve of 4.5 wt% IP-S/CNC/GBL mixture tensile sample

Compared to properties gained from micropillar compression, the yield stress seems to be lower for the tensile samples. A possible reason for this could be the fact, that the CNC are oriented randomly in the material. This means that there can be some cellulose nanocrystals in horizontal orientation in the gauge section and as there is no chemical bonding between the CNC and the matrix, these crystals could be crack initiating. Another reason could be that the material is not perfectly homogeneous. In tensile testing, the weakest point is crack initiating, which means that if there is a section without CNC, the tensile properties of this sample are almost the same as for neat IP-S. This is confirmed by the fact that the peak strength of the composite tensile samples is in the same range as the yield stress of neat IP-S. The Young's modulus seems to be higher for tensile testing, but as these confidence intervals are very high, this conclusion has to be treated with caution. As only samples printed with 15 mW laser power were tested, there is no information on the influence of the laser power on the mechanical properties in tensile testing. And due to the SARS-CoV-2 pandemic in 2020, which happened during the time this thesis was carried out, no more samples could be tested.

3.8.2 IP-S/CNC/GBL with 13.0 wt% CNC

Figure 47 shows pillars printed with different laser power. The shape of the pillars is good. The development worked not perfect, as there is still some residue on the wafer and on the surfaces of the pillars. On the pillars some rod-shaped features can be recognized. These can be explained by the tendency of CNC to agglomerate. And as cellulose is hardly soluble, these features were not dissolved during the development step. The shape of the pillars does not change with the laser power, but the dimensions increase, which can be caused by the increase of the voxel size of the focal spot. The true dimensions of the pillars are measured on a SEM and are shown in Table 20. The mechanical properties are summarized in Table 20 too.

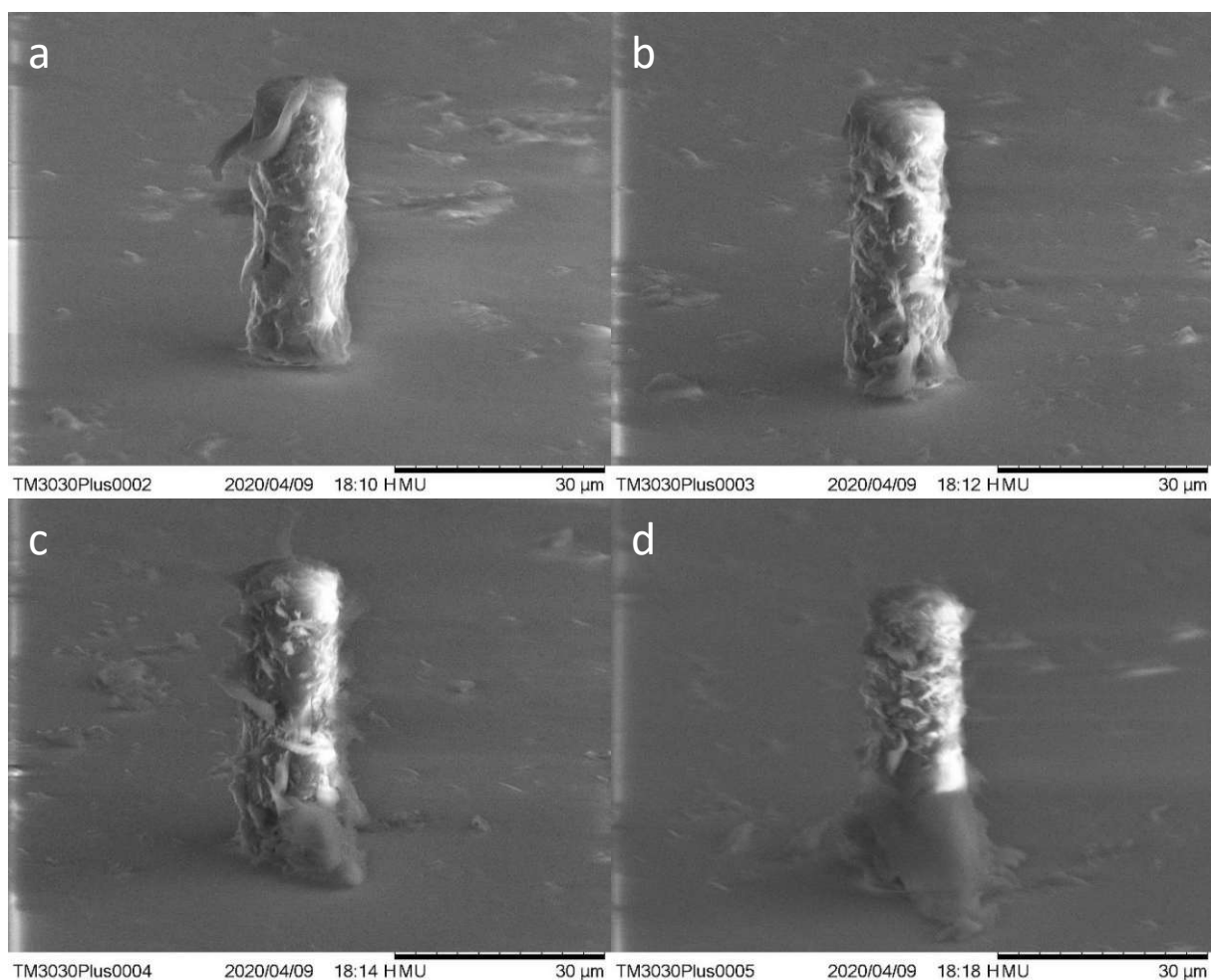


Figure 47: Pillars of 13 µm in diameter and 40 µm in height, printed with the IP-S/CNC/GBL mixture with 13.0 wt% CNC with different laser power: a, 12.5 mW, b, 17.5 mW, c, 22.5 mW, d, 27.5 mW

The real dimensions of the pillars differ up to 12 % in diameter and up to 5 % in height from the dimensions they should have. The stress-strain-curves (Figure 48) show typical elastic

deformation in the beginning, which transitions in plastic deformation with strain hardening of the material. The mechanical properties deviate quite much, especially the Young's moduli and the hardening moduli. This is most likely caused by inhomogeneities in the resist. As the CNC tends to agglomerate, the CNC concentration is locally different and thus the mechanical properties differ.

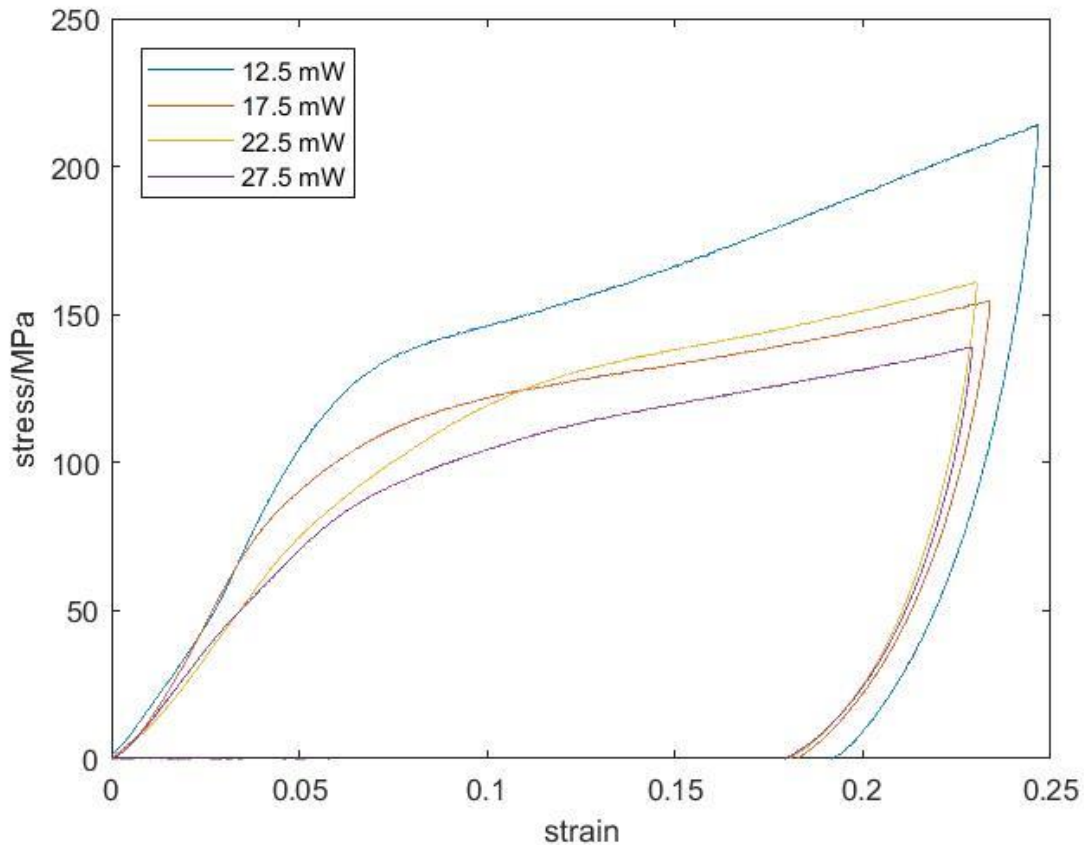


Figure 48: Stress-strain-curves of IP-S/CNC/GBL pillar compressions; 13.0 wt% CNC; printed with different laser power

Table 20: Dimensions and mechanical properties of the IP-S/CNC micropillars with 13.0 wt% CNC printed with different laser power; the dispersion is given for a confidence level of 95 %

Laser power, mW	Diameter, μm	Height, μm	Yield stress, MPa	Young's modulus, GPa	Hardening modulus, MPa	Number of samples
12.5	13.4	39.4	131 ± 33	2.68 ± 1.58	379 ± 227	8
17.5	14.1	41.0	113 ± 23	2.33 ± 1.00	301 ± 158	8
22.5	14.3	41.9	113 ± 34	1.91 ± 0.94	387 ± 438	7
27.5	14.6	42.1	96.2 ± 16.2	1.43 ± 0.51	282 ± 199	7

Figure 49 shows two hexagons from different perspectives. Their shape is good, the edges are quite sharp. As there is only a little bit of residue on the wafer and on the sidewalls inside and outside of the hexagons, the development worked quite well. The theoretical dimensions of the hexagons and their true dimensions are shown in Table 21. The theoretical width of the upper hexagon is $0.5\ \mu\text{m}$, which is only 1 laser beam. Its true width is $4.2\ \mu\text{m}$, which means that the maximum resolution achievable with this mixture is $4.2\ \mu\text{m}$ for 25 mW laser power.

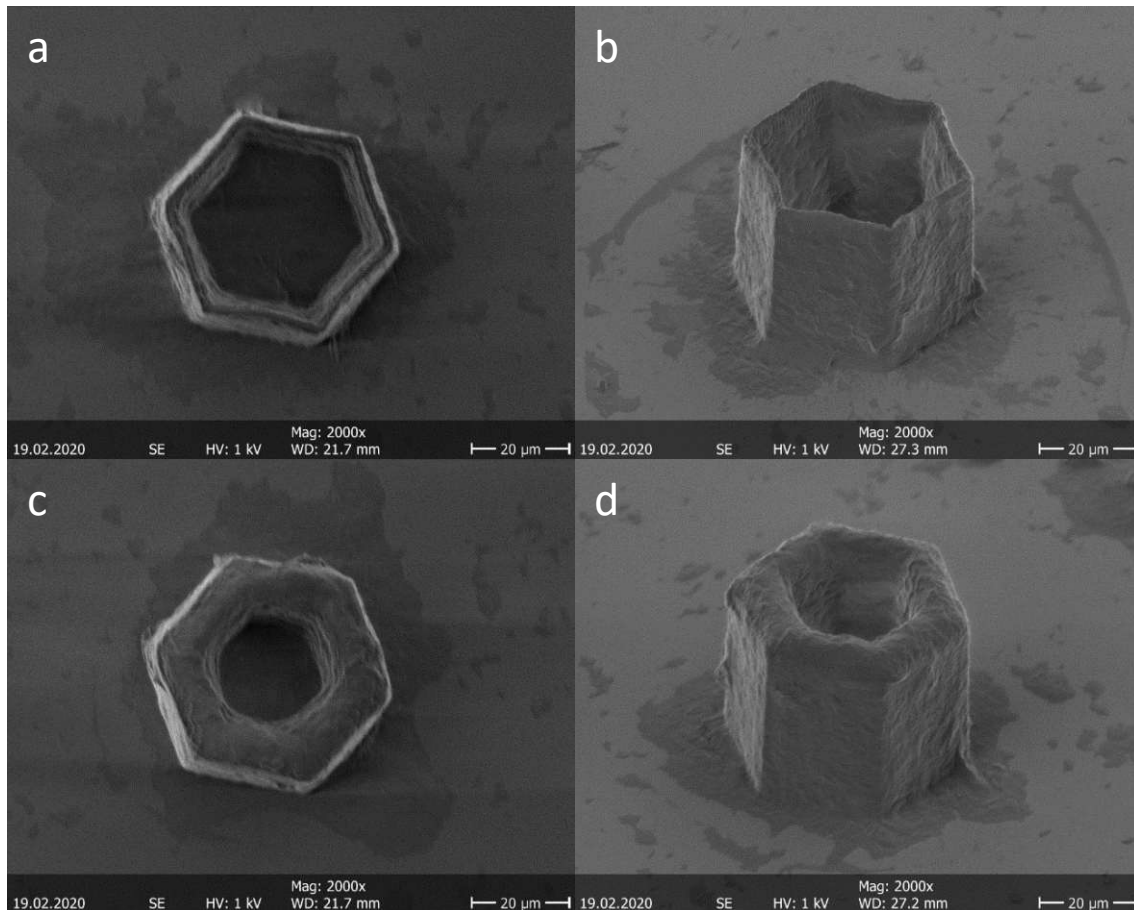


Figure 49: Hexagons printed with the IP-S/CNC/GBL mixture with 13.0 wt% CNC; the height is about $40\ \mu\text{m}$, the true wall width is: a, and b, $4.2\ \mu\text{m}$; c, and d, $10.6\ \mu\text{m}$; printed with 25 mW laser power

Table 21: Theoretical and true wall width of the hexagons in Figure 49

	Figure 49 a, and b,	Figure 49 c, and d,
Theoretical wall width	0.5	5.0
True wall width	4.2	10.6

Figure 50 shows tensile samples printed with different laser power. The shape of the upper left sample is good, the development worked quite well. With increasing laser power, the base of the sample gets more and more conical. The samples printed with 25 and 30 mW laser power are not testable anymore, but the samples printed with 15 mW laser power could be tested. Due to the SARS-CoV-2 pandemic in 2020, which happened during the time this thesis was carried out, the samples could not be tested. Nevertheless, it was proved that with this mixture tensile samples can be printed.

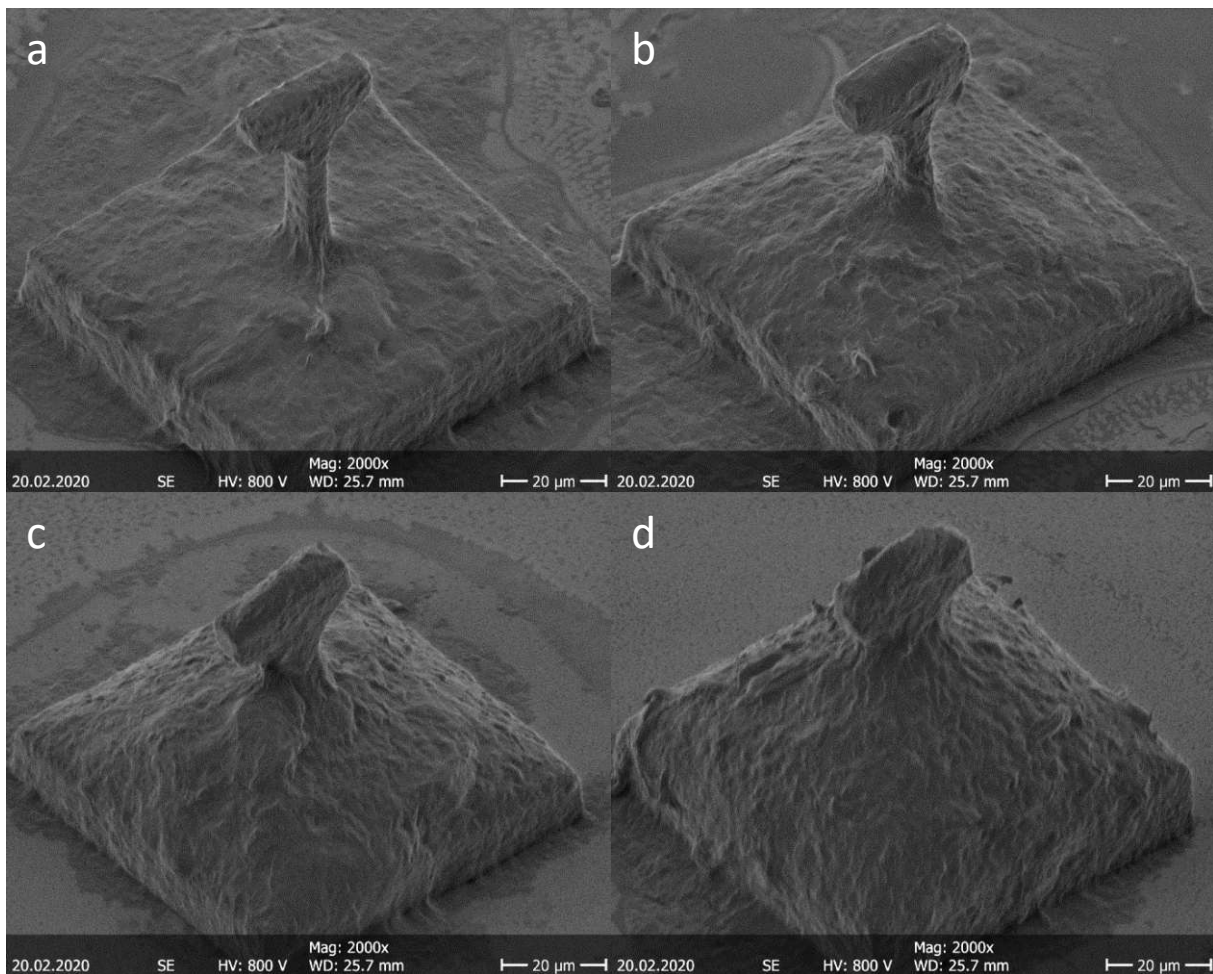


Figure 50: Tensile samples printed with the IP-S/CNC/GBL mixture with 13.0 wt% CNC and with different laser power: a, 15 mW; b, 20 mW; c, 25 mW, d, 30 mW

3.8.3 IP-S/CNC/HEMA

The pillars printed with this mixture, as well as hexagons printed with this mixture, are shown in Figure 51. The pillars are printed with the maximum laser power, which was possible (32.5 mW). The pillar should be 13 μm in diameter and 40 μm high, but the true dimensions

are $15.5\ \mu\text{m}$ in diameter and $24\ \mu\text{m}$ in height. The pillars printed with lower laser power were too soft, so that they buckled sideward. This suggests that the polymerization was insufficient. But as the laser power was already at its maximum intensity, an obvious conclusion would be that the concentration of photoinitiator is still too low. This would also explain the low height of the pillar.

The same problem is recognizable with the hexagons. The thickness of the walls should be $3\ \mu\text{m}$ and the height should be $40\ \mu\text{m}$. The true dimensions are $12.5\ \mu\text{m}$ in width and $33\ \mu\text{m}$ in height. The thickness of the structure is likely caused by radiation scattering, the low height could be explained in a lack of photoinitiator.

Nevertheless, this mixture was printable and the geometries of the structures are recognizable.

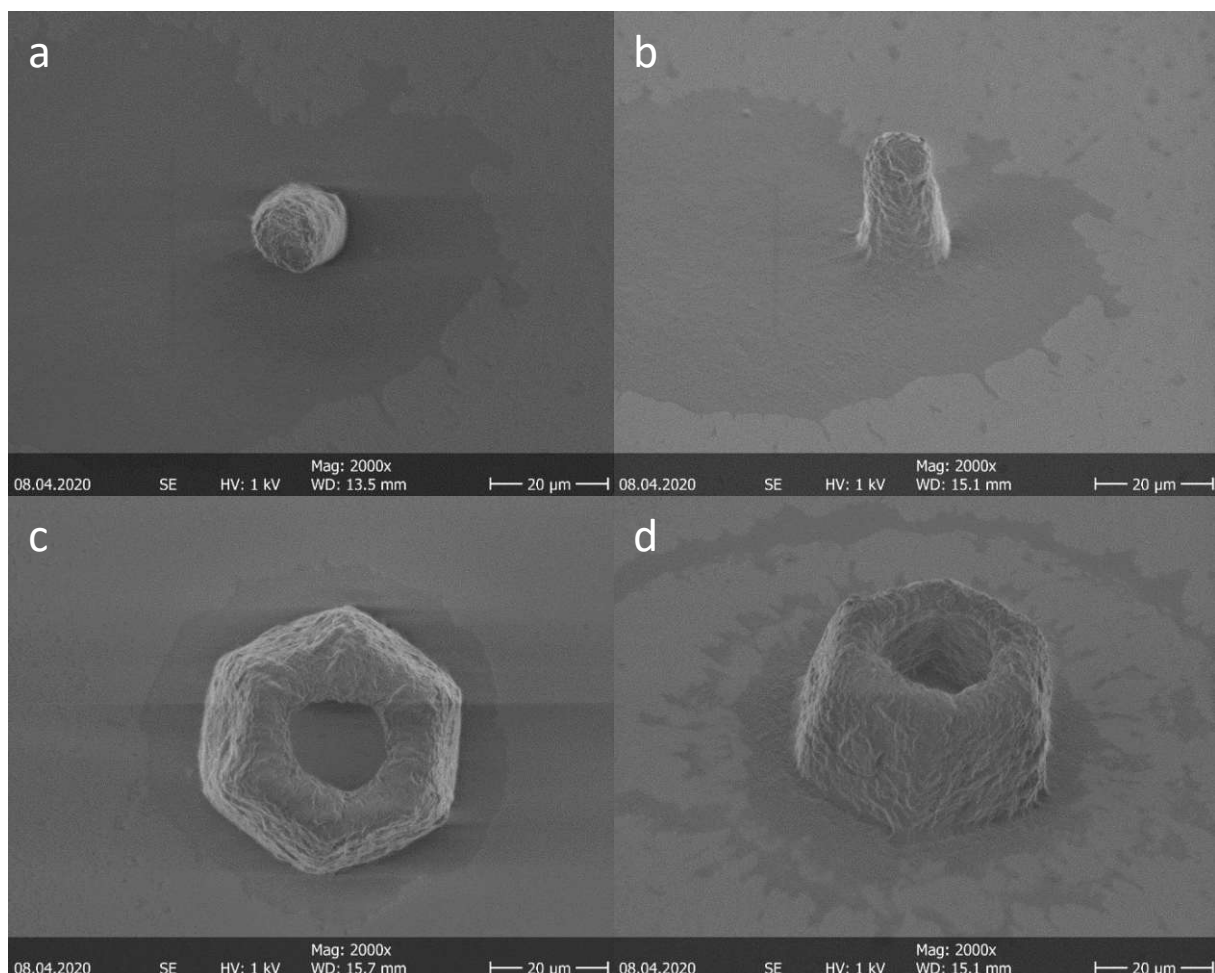


Figure 51: structures printed with the IP-S/CNC/HEMA mixture, true dimensions of the structures: a, and b, $15.5\ \mu\text{m}$ in diameter, $24\ \mu\text{m}$ in height; c, and d, wall thickness of $12.5\ \mu\text{m}$, height of $33\ \mu\text{m}$

3.9 General discussion

3.9.1 Process quality

As both neat photoresists have already been used for high resolution photolithography, the processes for these materials worked very well. The development was perfect, as no unpolymerized resist stayed on the wafers. The shape of the structures was exact and repeatable for the lower laser powers and the process was reproducible.

The development for the composite mixtures was not as good as for the neat photoresists, which is due to the insolubility of cellulose in the development solvents. The cellulose in the unpolymerized areas of the wafer was more suspended than dissolved during the development step, which was only achieved by magnetic stirring. The development was best for the IP-S/CNC/GBL composite with 4.5 wt% CNC. There was almost no residue on the wafer and on the structures. With increasing CNC amount the development got worse, but it still worked for the structures printed during this thesis, as they were comparatively simple. The structures for the 13.0 wt% mixture were well shaped, but on their surface there were some fibrous residues, which can be explained by the formation of CNC agglomerates, which jutted out of the structures and could not be removed during development. And in general, the development worked better for the 3D lithography process, which is likely due to the larger distance between the structures.

The development of the structures printed with the SU-8/CNC/GBL mixture worked not as well as the development for the IP-S composite with the same CNC content. As both of the neat resist are soluble in the developer and the CNC content is the same, a possible reason for this could be the fact that the dispersion of the cellulose was not that good in the SU-8 as in the IP-S, which led to bigger agglomerates. Another possible reason for this could be the post baking step, which was only performed with the SU-8 composites, but as the cellulose is stable at 90 °C, there should not be any reaction effecting the development step. The shape of the structures printed with this mixture was good, but there were some features on them too, which could be caused by CNC agglomerates, similar to what was observed for the IP-S composite with 13 wt% CNC.

The development of the IP-S composite with HEMA worked well, too, as there is no unpolymerized resist left on the wafer. Unfortunately, the process did not work properly

enough to print structures, which could be mechanically tested. The reason for this could be a lack of photoinitiator. There have already been added 1.5 wt% Irgacure 819 photoinitiator to this mixture, but as about 50 wt% of this mixture is HEMA, which does not contain any photoinitiator, this addition was maybe too little.

Another important aspect, which has to be discussed, is the failure quota of the mixtures. For the neat photoresists, all of the printed structures were usable. The lowest failure quota of the composites was achieved with the 4.5 wt% IP-S/CNC/GBL mixture. With this mixture, only about 10 % of the pillars had some features or were shaped in a way that they could not be tested. About the same amount of the tensile samples was not testable too due to a tilt of the sample head of due to some features on the surface. The failure quota increased with the cellulose content. For the IP-S/CNC/GBL mixture with 13 wt% CNC about 25 % of the pillars could not be tested due to some features on the top surface. A problem, which only occurred with the SU-8/CNC/GBL mixture, was that even with adhesion promoter about 40 % of the pillars detached during development. This is surely caused by the solvent flow during development with magnetic stirring and by the rinsing of the wafer with PGMEA, but these steps had to be performed to remove the cellulose of the unpolymerized parts. The failure quota of the IP-S/CNC/HEMA mixture can be seen as 100 %, as no testable pillars could be printed.

3.9.2 Mechanical properties

The mechanical properties gained by pillar compression are summarized in Figure 52 to Figure 54. Between both the yield stresses and Young's moduli of neat SU-8 printed by 2D and 3D lithography is no significant difference, which means that there is not influence on the mechanical properties by changing the exposure method. This is consistent with the fact that the main part of the polymerization happens during the post exposure baking. The properties drastically decrease by adding CNC, which is very likely caused by introduction of water into the mixture with the CNC. As already discussed in chapter 3.6 SU-8/CNC composite 3D Lithography, the water would lead to a decrease in reactive groups and thus the degree of cross-linking would decrease. If the mechanical properties of the SU-8/CNC composites are compared, one can see that they increase with the laser power used for printing. A reason for

this could be the higher amount of activated photoinitiator and thus reactive species, which can polymerize and cross-link in the post-exposure baking.

The yield stress of both IP-S/CNC/GBL mixtures tends to decrease with the laser power, which is the same for neat IP-S. This could be explained by the activation of more photoinitiator molecules and thus the creation of more radicals with higher laser power. This would lead to a higher number of polymer chains with a lower molecular weight and degree of polymerization (DP). This would explain the decrease in mechanical properties, as these are dependent on the DP [74]. This effect is more distinct for higher CNC content. A possible reason for this could be that the cellulose acts as a barrier for the polymerization and thus further decreases the DP and the molecular weight of the polymer chains.

While the Young's modulus is decreasing with the laser power for the mixture with 13.0 wt% CNC and for neat IP-S, the modulus of the mixture with 4.5 wt% CNC does not significantly change. But as the confidence intervals of the modulus of this mixture is quite high, maybe the trend is just not recognisable. The reason for the trend could be the same as for the decrease in yield stress. For the hardening modulus no significant trend is recognisable for the CNC composites as well as for neat IP-S.

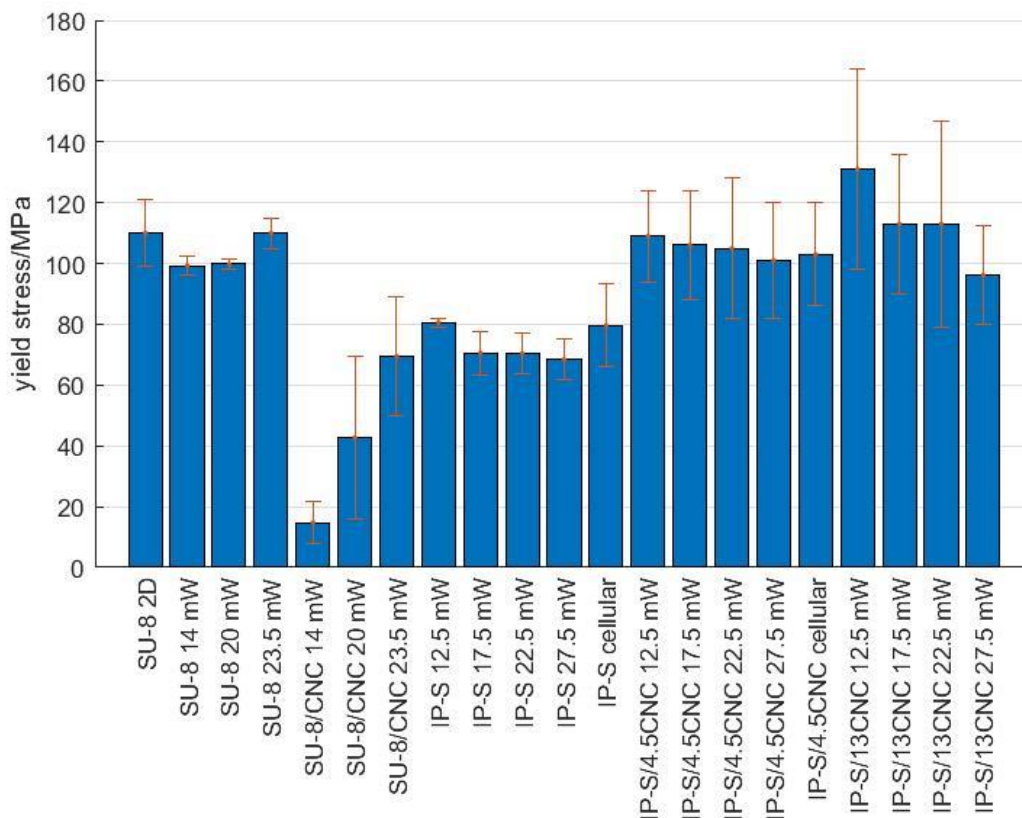


Figure 52: Yield stresses of the different resists and mixtures gained by pillar compression, error bar is calculated for a confidence level of 95 %

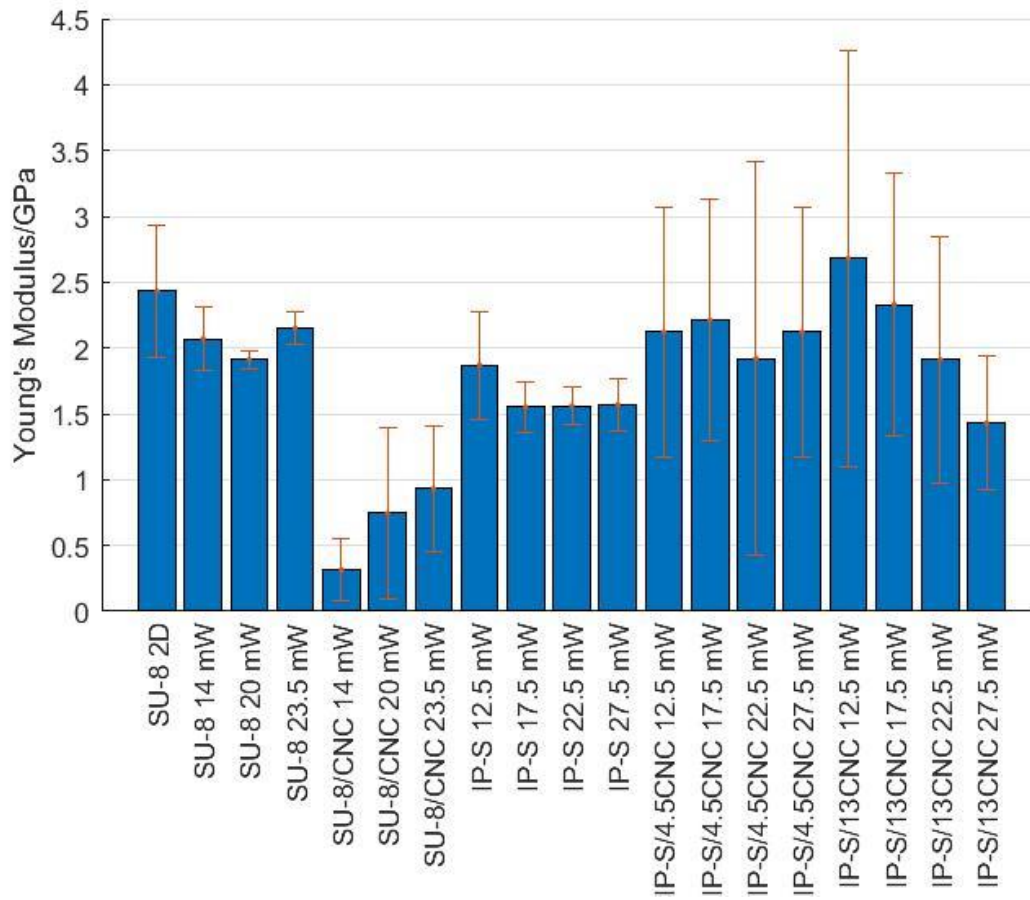


Figure 53: Young's moduli of the different resists and mixtures gained by pillar compression, error bar is calculated for a confidence level of 95 %

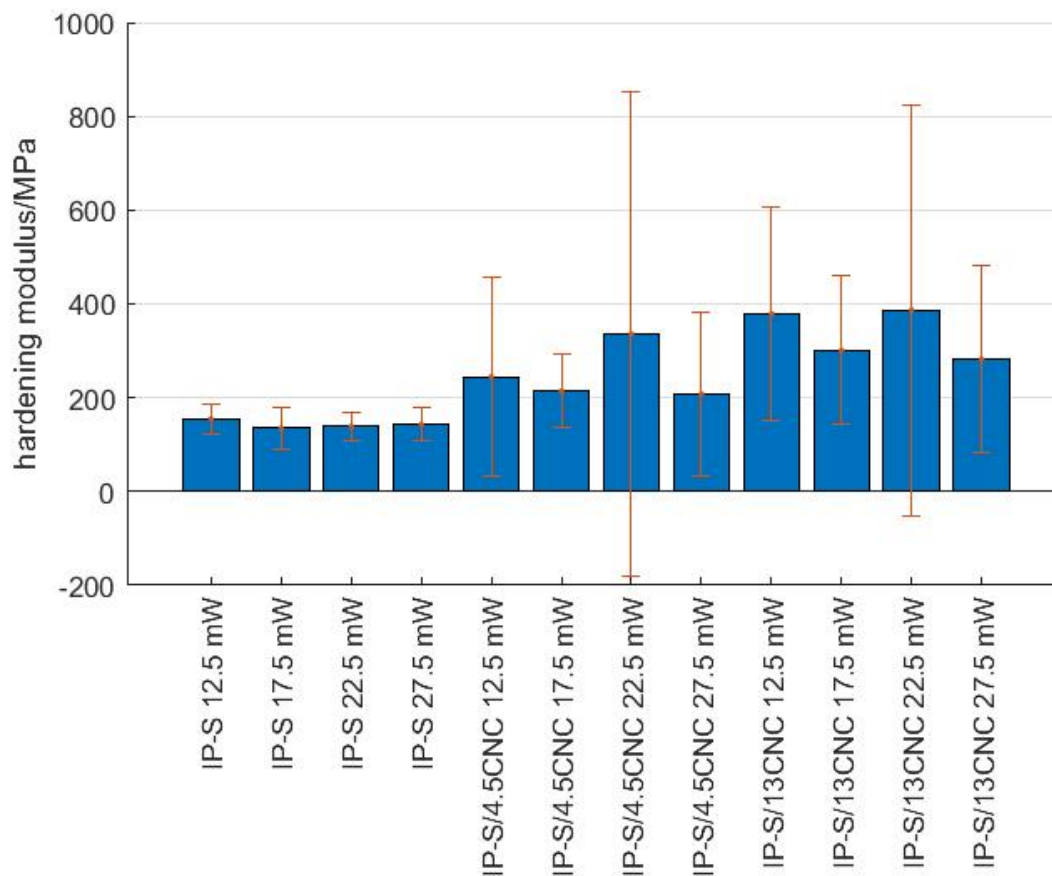


Figure 54: Hardening moduli of the different resists and mixtures gained by pillar compression, error bar is calculated for a confidence level of 95 %

If the mechanical properties of neat IP-S and the two IP-S/CNC/GBL composites gained from pillar compressions are compared (Figure 55), all of them increased remarkably with the amount of CNC in the photoresist, but only for the lowest laser power. For the series with 12.5 mW laser power, the yield stress increased by 35 % for the 4.5 wt% mixture and by 63 % for the 13.0 wt% mixture. The Young's modulus increased by 13 % for the 4.5 wt% mixture and by 43 % for the 13.0 wt% mixture, the hardening modulus by 58 % for the 4.5 wt% mixture and by 144 % for the 13 wt% mixture. If the properties of the mixtures printed with 27.5 mW laser power are compared, the yield stress increased by 48 % for the 4.5 wt% mixture and by 41 % for the 13.0 wt% mixture. The Young's modulus increased by 35 % for the 4.5 wt% mixture and even decreases by 9 % for the 13.0 wt% mixture, the hardening modulus increases by 45 % for the 4.5 wt% mixture and by 97 % for the 13 wt% mixture. This shows that the yield stress and the Young's modulus for the 13.0 wt% mixture are lower than for the 4.5 wt% mixture, which means that the weakening by increasing laser power exceeds the effect of strengthening by adding more CNC.

The peak strength gained by compression of the cellular structures is almost the same as the yield stress gained by pillar compression for both neat IP-S and for the 4.5 wt% IP-S/CNC/GBL mixture, which indicated, that the process is uniform.

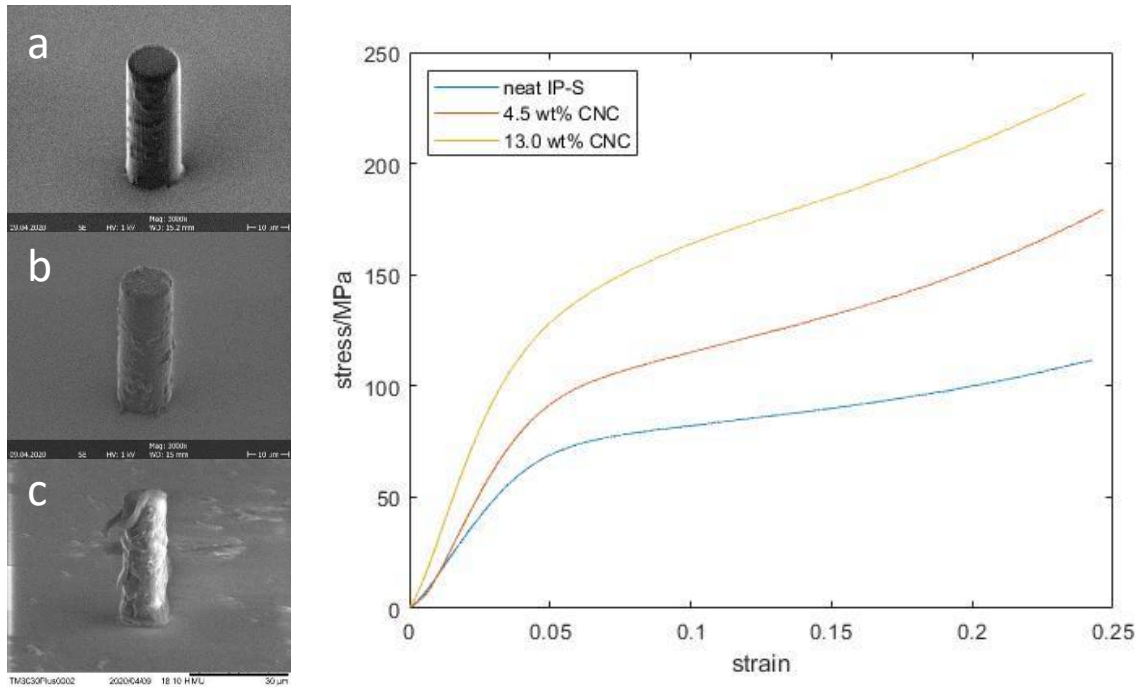


Figure 55: Stress-strain-curves of pillar compression of neat IP-S and the IP-S/CNC/GBL composites; a, neat IP-S; b, 4.5 wt% CNC; c, 13.0 wt% CNC

To evaluate the influence of the laser power and the CNC content on the yield stress and the Young's modulus, an analysis of variance (ANOVA) and a multiple linear regression was performed for both yield stress (Table 22 and Figure 56) and Young's modulus (Table 23 and Figure 57). The ANOVA showed that the probability of a significant dependency of the mechanical properties on these two parameters is higher than 99.5 %. The multiple linear regression model is significant with a p-value < 0.0001 for both properties. The scattering of the yield stress and Young's modulus is represented by quite high r^2 -values for the model, which are 0.6371 for the yield stress and 0.3604 for the Young's modulus.

Table 22: Results of the ANOVA for the dependency of the yield stress on the laser power and the CNC content

	p-value
Laser power	< 0.0001
CNC content	< 0.0001
Laser power * CNC content	0.003

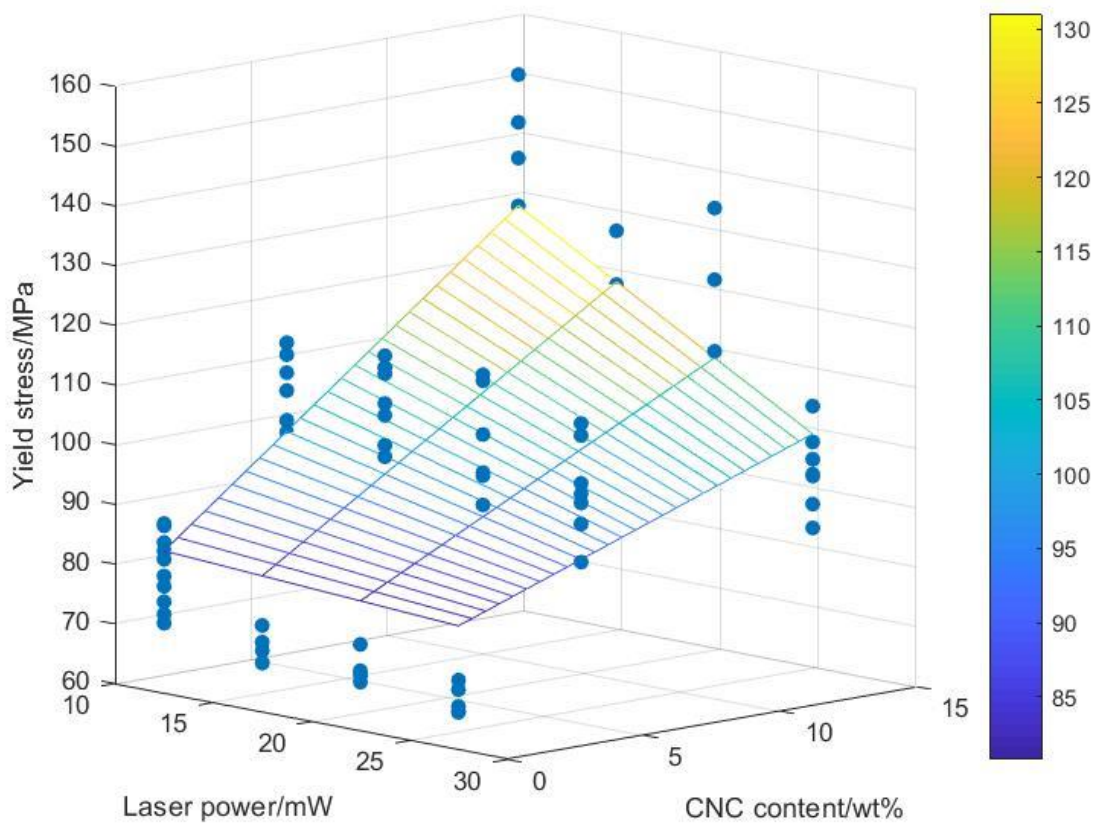


Figure 56: Dependency of the yield stress on laser power and CNC content by multiple linear regression

Table 23: Results of the ANOVA for the dependency of the Young's modulus on the laser power and the CNC content

	p-value
Laser power	0.0001
CNC content	0.0001
Laser power * CNC content	0.0018

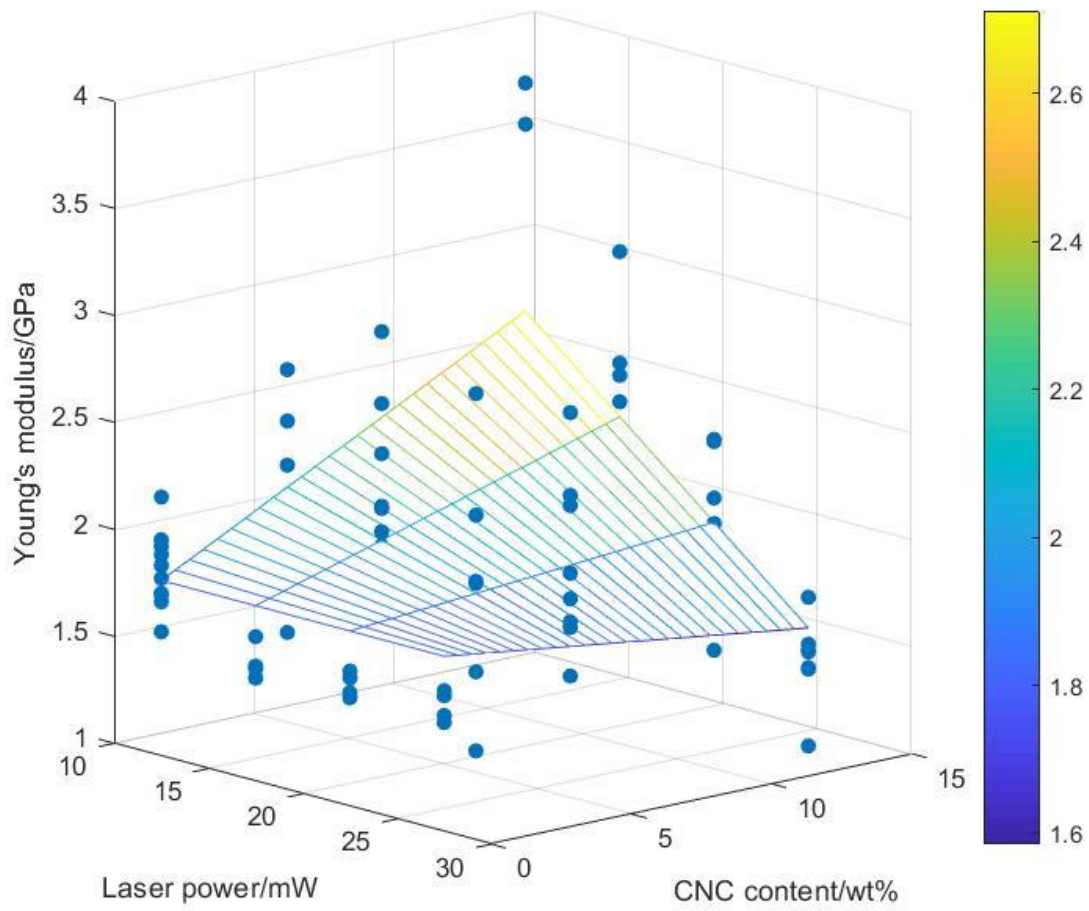


Figure 57: Dependency of the Young's modulus on laser power and CNC content by multiple linear regression

3.9.3 Process parameters

The dimensions of the printed structures increase with the laser power, which is true for the neat resists as well as for all the mixtures. This effect is the most distinct at the IP-S/CNC/GBL mixture with 13.0 wt%, which can be explained by the increasing radiation scattering on the cellulose. Another phenomenon, which was only observed with neat SU-8, is the formation of a convex shape of pillars with high laser power. The reason for this change in shape is most likely overexposure. As the voxel size of the focal spot of the laser increases with the laser power, the overlapping volume of the scanning laser beam is increasing too. This leads to more and more laser power in the middle section of the pillar compared to the top and the bottom of it resulting in convex shaped pillars. Due to all these reasons, the best laser power can be said to be the lowest laser power, which still causes sufficient polymerization. For which laser powers the best results were obtained in thesis are summarized in Table 24. This values only apply, if the other parameters are the same too. In this thesis, the scanning speed was set to 10 mm/s, the hatching and slicing distance was set to 0.5 μm .

Table 24: Summary of the laser powers, which the best results were obtained with

SU-8	SU-8/CNC	IP-S	IP-S/CNC/GBL 4.5 wt%	IP-S/CNC/GBL 13.0 wt%
14 mW	14 mW	12.5 mW	12.5 mW	12.5 mW

For neat IP-S, the recommended durations in PGMEA and isopropanol are between 10 and 20 min each. This worked very well. For the development of neat SU-8 and the different composites, no general durations can be recommended. The higher the cellulose content and the thicker the resist, the longer the development will take. For neat SU-8 and the SU-8 composite, the development had to be done very carefully, as the adhesion to the glass wafer was very poor. For the composite, the development was not possible without magnetic stirring and rinsing the wafer, but because of the solvent stream and the pressure, which was applied by rinsing the wafer, some structures detached too. As the adhesion of the IP-S composited to the wafer was much better, the development conditions did not have to be that gentle. Much more pressure was applicable on the wafer, which caused a better development.

4 Conclusions

Without photolithography, the modern world would not be the same as it is. As it is one of the main technologies used for the fabrication of semiconductor devices, photolithography was and is still an important tool towards a digital future. This thesis showed, that photolithography is also possible with a green and renewable component. As the society is more and more interested in sustainability and ecological material, the step of introducing CNC into photoresists to improve its properties is an important step towards green photolithography.

The best results were surely achieved with the IP-S systems. This thesis showed that in compression testing the yield stress increased by 35 % for 4.5 wt% CNC and 63 % for 3.0 wt% CNC, the Young's modulus increased by 13 % for 4.5 wt% CNC and by 43 % for 13.0 wt% CNC, and the hardening modulus increased by 58 % for 4.5 wt% CNC and by 144 % for 13.0 wt% CNC. These results are very remarkable, but the most impressive is that these improvements go hand in hand with a resolution which was still in the lower one-digit micrometre range. This great resolution was the main requirement for printing cellular structures, which is also possible for the mixture with 4.5 wt% CNC, as this thesis shows. These structures were well shaped and showed almost the same increase in mechanical properties as the results gained by micropillar compression. As the thickness of the struts decreased from the bottom to the top and the main deformation only occurred in the top and the middle layer, the top strut thickness was chosen for the calculations for the determination of the peak strength. As the peak strengths of both the neat IP-S and the composite are in the same range as the yield stresses of these materials, the analysis can be seen as correct.

The IP-S system with HEMA and 5.0 wt% CNC was printable too, but there were still some problems, as the polymerization seemed to be not sufficient. As there was not enough time to do further improvement on this mixture during the thesis, the shape of the structures printed with it was not perfect, but at least it was printable, which is already a good achievement.

The first try to introduce CNC into in SU-8 via acetone failed, but it was possible as GBL was used instead on acetone. The shape of the structures was clearly recognizable, but the resolution was worse compared to the mixtures with IP-S. The mechanical properties of the

composite showed a drastic decrease of 37 % in yield stress and 57 % in Young's modulus, which was likely caused by introducing water unwarily into the epoxy resist and thus decreased the ability to crosslink by reducing the amount of epoxy groups in the resist.

The main problem with all of the composites was the insolubility of cellulose in the developing solvent. This caused that the development was not perfect all the time, especially for the more complex structures and for the mixture with 13.0 wt% CNC. As cellulose is not soluble in almost all solvents, this problem is not easily solved. The simplest possibility to improve the development is to try another step with water as developing solvent. As CNC can be suspended in water quite well, this is definitely worth a try. Another possibility to dissolve cellulose are ionic liquids. It is proven that these very polar liquids can dissolve cellulose [76], [77], but it is also possible that ionic liquids dissolve the matrix polymer. Nevertheless, this would be a next step to increase the processability of these cellulose composites, and furthermore, it would also be a next step towards a more ecological process, as these ionic liquids can be regenerated [78].

Another possibility of increasing the solubility of cellulose is to chemically modify its surface. If methacrylate groups were introduced on the surface of the CNC, this would maybe increase its solubility in polar solvents like PGMEA. Furthermore, this would probably lead to an increase in mechanical properties, as the CNC could then also react with the polymer matrix during polymerization, which means that there will be covalent bonds between the filler and the polymer.

As the CNC are anisotropic particles, the mechanical properties can also be improved by aligning the CNC [79]. Research already showed that this is possible by shear stress [80], which was realized by extruding high concentrated inks through a nozzle during direct ink writing or by spin coating [81]. CNC have also been oriented by applying an electric field. Therefore, electrodes were patterned on a glass slide by photolithography. Then the glass surface was modified with aminopropyltrimethoxysilane to enhance the adhesion between the glass slide and the CNC. After applying the AC electric field, a drop of CNC suspension was placed between two electrodes and the CNC oriented parallel to the electric field [82].

In conclusion, this thesis showed that cellulose nanocrystal composites are suitable for high resolution 3D printing and there are still a lot of opportunities to improve the already impressive properties of these composites.

5 References

- [1] L. R. Meza and J. R. Greer, "Mechanical characterization of hollow ceramic nanolattices," *J. Mater. Sci.*, vol. 49, no. 6, pp. 2496–2508, Mar. 2014.
- [2] L. R. Meza, S. Das, and J. R. Greer, "Strong, lightweight, and recoverable three-dimensional ceramic nanolattices," *Science (80-.)*, vol. 345, pp. 1322–1326, 2014.
- [3] X. Zhang, Y. Wang, B. Ding, and X. Li, "Design, Fabrication, and Mechanics of 3D Micro-/Nanolattices," *Small*. Wiley-VCH Verlag, 2019.
- [4] S. Weiner and H. D. Wagner, "THE MATERIAL BONE: Structure-Mechanical Function Relations," *Annu. Rev. Mater. Sci.*, vol. 28, pp. 271–298, 1998.
- [5] J. Y. Rho, L. Kuhn-Spearing, and P. Zioupos, "Mechanical properties and the hierarchical structure of bone," *Med. Eng. Phys.*, vol. 20, pp. 92–102, 1998.
- [6] L. J. Gibson, "The hierarchical structure and mechanics of plant materials," *J. R. Soc. Interface*, vol. 9, pp. 2749–2766, Nov. 2012.
- [7] O. Sigmund and S. Torquato, "Design of materials with extreme thermal expansion using a three-phase topology optimization method," *J. Mech. Phys. Solids*, vol. 45, pp. 1037–1067, 1997.
- [8] C. A. Steeves, S. L. dos Santos e Lucato, M. He, E. Antinucci, J. W. Hutchinson, and A. G. Evans, "Concepts for structurally robust materials that combine low thermal expansion with high stiffness," *J. Mech. Phys. Solids*, vol. 55, pp. 1803–1822, 2007.
- [9] J. Bauer, A. Schroer, R. Schwaiger, and O. Kraft, "Approaching theoretical strength in glassy carbon nanolattices," *Nat. Mater.*, vol. 15, no. 4, pp. 438–443, Apr. 2016.
- [10] L. Valdevit, S. W. Godfrey, T. A. Schaedler, A. J. Jacobsen, and W. B. Carter, "Compressive strength of hollow microlattices: Experimental characterization, modeling, and optimal design," *J. Mater. Res.*, vol. 28, no. 17, pp. 2461–2473, Sep. 2013.
- [11] J. Bauer, S. Hengsbach, I. Tesari, R. Schwaiger, and O. Kraft, "High-strength cellular ceramic composites with 3D microarchitecture," *Proc. Natl. Acad. Sci. U. S. A.*, vol.

- 111, no. 7, pp. 2453–2458, Feb. 2014.
- [12] M. F. Ashby, “The properties of foams and lattices,” *Philos. Trans. R. Soc. A Math. Phys. Eng. Sci.*, vol. 364, no. 1838, pp. 15–30, Jan. 2006.
- [13] T. Bückmann *et al.*, “Tailored 3D mechanical metamaterials made by dip-in direct-laser-writing optical lithography,” *Adv. Mater.*, vol. 24, no. 20, pp. 2710–2714, May 2012.
- [14] S. Babaei, J. Shim, J. C. Weaver, E. R. Chen, N. Patel, and K. Bertoldi, “3D soft metamaterials with negative poisson’s ratio,” *Adv. Mater.*, vol. 25, no. 36, pp. 5044–5049, Sep. 2013.
- [15] H. Kargarzadeh *et al.*, “Recent developments on nanocellulose reinforced polymer nanocomposites: A review,” *Polymer (Guildf)*, vol. 132, pp. 368–393, Dec. 2017.
- [16] Y. Habibi, L. A. Lucia, and O. J. Rojas, “Cellulose nanocrystals: Chemistry, self-assembly, and applications,” *Chem. Rev.*, vol. 110, no. 6, pp. 3479–3500, Jun. 2010.
- [17] D. Klemm *et al.*, “Nanocellulose as a natural source for groundbreaking applications in materials science: Today’s state,” *Materials Today*, vol. 21, no. 7. Elsevier B.V., pp. 720–748, 01-Sep-2018.
- [18] A. Chakrabarty and Y. Teramoto, “Recent advances in nanocellulose composites with polymers: A guide for choosing partners and how to incorporate them,” *Polymers*, vol. 10, no. 5. MDPI AG, 10-May-2018.
- [19] D. Del Vescovo and I. Giorgio, “Dynamic problems for metamaterials: Review of existing models and ideas for further research,” *Int. J. Eng. Sci.*, vol. 80, pp. 153–172, 2014.
- [20] L. R. Meza, A. J. Zelhofer, N. Clarke, A. J. Mateos, D. M. Kochmann, and J. R. Greer, “Resilient 3D hierarchical architected metamaterials,” *Proc. Natl. Acad. Sci. U. S. A.*, vol. 112, no. 37, pp. 11502–11507, Sep. 2015.
- [21] P. Schürch, L. Pethö, J. Schwiedrzik, J. Michler, and L. Philippe, “Additive Manufacturing through Galvanofarming of 3D Nickel Microarchitectures: Simulation-Assisted Synthesis,” *Adv. Mater. Technol.*, vol. 3, no. 12, Dec. 2018.

- [22] W. K. Choi, T. H. Liew, M. K. Dawood, H. I. Smith, C. V. Thompson, and M. H. Hong, "Synthesis of silicon nanowires and nanofin arrays using interference lithography and catalytic etching," *Nano Lett.*, vol. 8, no. 11, pp. 3799–3802, 2008.
- [23] J. P. Hsu, S. H. Lin, W. C. Chen, and S. Tseng, "Mathematical analysis of soft baking in photolithography," *J. Appl. Phys.*, vol. 89, no. 3, pp. 1861–1865, Feb. 2001.
- [24] H. B. Sun and S. Kawata, "Two-photon Photopolymerization and 3D Lithographic Microfabrication," in *NMR • 3D Analysis • Photopolymerization. Advances in Polymer Science*, vol. 170, 2004, pp. 169–273.
- [25] M. G. Papadopoulos, A. J. Sadlej, and J. Leszczynski, *Non-Linear Optical Properties of Matter: From molecules to condensed phases*. Springer Science & Business Media, 2007.
- [26] S. Wu, J. Serbin, and M. Gu, "Two-photon polymerisation for three-dimensional micro-fabrication," *J. Photochem. Photobiol. A Chem.*, vol. 181, pp. 1–11, 2006.
- [27] S. Kawata, H.-B. Sun, T. Tanaka, and K. Takada, "Finer features for functional microdevices," *Nature*, vol. 412, no. 6848, pp. 697–698, 2001.
- [28] S. Juodkazis, V. Mizeikis, K. K. Seet, M. Miwa, and H. Misawa, "Two-photon lithography of nanorods in SU-8 photoresist," *Nanotechnology*, vol. 16, no. 6, pp. 846–849, 2005.
- [29] X. Zhou, Y. Hou, and J. Lin, "A review on the processing accuracy of two-photon polymerization," *AIP Adv.*, vol. 5, no. 3, Mar. 2015.
- [30] M. G. Guney and G. K. Fedder, "Estimation of line dimensions in 3D direct laser writing lithography," *J. Micromech. Microeng.*, vol. 26, 2016.
- [31] H. Lorenz, M. Despont, P. Vettiger, and P. Renaud, "Fabrication of photoplastic high-aspect ratio microparts and micromolds using SU-8 UV resist," *Microsyst. Technol.*, vol. 4, pp. 143–146, 1998.
- [32] H. S. Khoo, K.-K. Liu, F.-G. Tseng, X. Wang, J. Engel, and C. Liu, "SU-8 thick photoresist processing as a functional material for MEMS applications Liquid crystal polymer for MEMS: processes and applications," *J. Micromech. Microeng.*, vol. 12, pp. 368–374,

- 2002.
- [33] H. Lorenz Aq, M. Despont, N. Fahrni, J. Brugger, P. Vettiger, and P. Renaud, "High-aspect-ratio, ultrathick, negative-tone near-UV photoresist and its applications for MEMS," *Sensors Actuators A*, vol. 64, pp. 33–39, 1998.
- [34] H. Lorenz and et al, "SU-8: a low-cost negative resist for MEMS," *J. Micromech. Microeng*, vol. 7, pp. 121–124, 1997.
- [35] A. L. Bogdanov and S. S. Peredkov, "Use of SU-8 photoresist for very high aspect ratio x-ray lithography," *Microelectron. Eng.*, vol. 53, pp. 493–496, 2000.
- [36] B. Bilenberg *et al.*, "High resolution 100 kV electron beam lithography in SU-8," *Microelectron. Eng.*, vol. 83, pp. 1609–1612, 2006.
- [37] C. Liu *et al.*, "Diffusion of water into SU-8 microcantilevers," *Phys. Chem. Chem. Phys.*, vol. 12, no. 35, pp. 10577–10583, 2010.
- [38] A. Olziersky *et al.*, "Insight on the SU-8 resist as passivation layer for transparent Ga₂O₃ - In₂O₃-ZnO thin-film transistors," *J. Appl. Phys.*, vol. 108, no. 6, Sep. 2010.
- [39] O. Prakash Parida and N. Bhat, "CHARACTERIZATION OF OPTICAL PROPERTIES OF SU-8 AND FABRICATION OF OPTICAL COMPONENTS," in *ICOP 2009-International Conference on Optics and Photonics*, 2009.
- [40] M. Hopcroft *et al.*, "Micromechanical testing of SU-8 cantilevers," *Fatigue Fract. Eng. Mater. Struct.*, vol. 28, no. 8, pp. 735–742, Aug. 2005.
- [41] A. Mcleavey, G. Coles, R. L. Edwards, and W. N. Sharpe, "Mechanical properties of SU-8," in *Materials Research Society Symposium - Proceedings*, 1999, vol. 546, pp. 213–218.
- [42] N. J. Shirtcliffe *et al.*, "The use of high aspect ratio photoresist (SU-8) for super-hydrophobic pattern prototyping," *J. Micromechanics Microengineering*, vol. 14, no. 10, pp. 1384–1389, Oct. 2004.
- [43] J. P. Esquivel *et al.*, "A COMPACT AND FULLY-INTEGRATED SU-8 MICRO DIRECT METHANOL FUEL CELL," in *Power-MEMS*, 2010.
- [44] "www.nanoscribe.com," (Access: 2020.03.27).

- [45] S. Boufi, H. Kaddami, and A. Dufresne, "Mechanical performance and transparency of nanocellulose reinforced polymer nanocomposites," *Macromol. Mater. Eng.*, vol. 299, no. 5, pp. 560–568, 2014.
- [46] V. Favier, G. R. Canova, J. Y. Cavail  , H. Chanzy, A. Dufresne, and C. Gauthier, "Nanocomposite materials from latex and cellulose whiskers," *Polym. Adv. Technol.*, vol. 6, no. 5, pp. 351–355, 1995.
- [47] V. Favier, H. Chanzy, and J. Y. Cavaille, "Polymer Nanocomposites Reinforced by Cellulose Whiskers," *Macromolecules*, vol. 28, no. 18, pp. 6365–6367, 1995.
- [48] R. Kolakovic, T. Laaksonen, L. Peltonen, A. Laukkanen, and J. Hirvonen, "Spray-dried nanofibrillar cellulose microparticles for sustained drug release," *Int. J. Pharm.*, vol. 430, pp. 47–55, 2012.
- [49] A. Blanco, M. C. Monte, C. Campano, A. Balea, N. Merayo, and C. Negro, "Nanocellulose for Industrial Use," in *Handbook of Nanomaterials for Industrial Applications*, 2018, pp. 74–126.
- [50] W. Hamad, "ON THE DEVELOPMENT AND APPLICATIONS OF CELLULOSIC NANOFIBRILLAR AND NANOCRYSTALLINE MATERIALS," *Can. J. Chem. Eng.*, vol. 84, pp. 513–519, 2006.
- [51] A.   turcov , G. R. Davies, and S. J. Eichhorn, "Elastic modulus and stress-transfer properties of tunicate cellulose whiskers," *Biomacromolecules*, vol. 6, no. 2, pp. 1055–1061, Mar. 2005.
- [52] U. Karabiyik, M. Mao, M. Roman, T. Jaworek, G. Wegner, and A. R. Esker, "Optical Characterization of Cellulose Films via Multiple Incident Media Ellipsometry," in *ACS Symposium series*, 2009, pp. 137–155.
- [53] X. Sun, Q. Wu, S. Ren, and T. Lei, "Comparison of highly transparent all-cellulose nanopaper prepared using sulfuric acid and TEMPO-mediated oxidation methods," *Cellulose*, vol. 22, no. 2, pp. 1123–1133, 2015.
- [54] W. J. Wang, W. W. Wang, and Z. Q. Shao, "Surface modification of cellulose nanowhiskers for application in thermosetting epoxy polymers," *Cellulose*, vol. 21, no. 4, pp. 2529–2538, 2014.

- [55] V. Khoshkava and M. R. Kamal, "Effect of surface energy on dispersion and mechanical properties of polymer/nanocrystalline cellulose nanocomposites," *Biomacromolecules*, vol. 14, no. 9, pp. 3155–3163, Sep. 2013.
- [56] A. Leszczyńska, P. Radzik, E. Szefer, M. Mičušík, M. Omastová, and K. Pielichowski, "Surface modification of cellulose nanocrystals with succinic anhydride," *Polymers (Basel)*, vol. 11, no. 5, May 2019.
- [57] N. H. Inai, A. E. Lewandowska, O. R. Ghita, and S. J. Eichhorn, "Interfaces in polyethylene oxide modified cellulose nanocrystal - polyethylene matrix composites," *Compos. Sci. Technol.*, vol. 154, pp. 128–135, Jan. 2018.
- [58] C. L. Morelli, N. Belgacem, R. E. S. Bretas, and J. Bras, "Melt extruded nanocomposites of polybutylene adipate-co-terephthalate (PBAT) with phenylbutyl isocyanate modified cellulose nanocrystals," *J. Appl. Polym. Sci.*, vol. 133, no. 34, Sep. 2016.
- [59] D. D. da S. Parize *et al.*, "Solution blow spun nanocomposites of poly(lactic acid)/cellulose nanocrystals from Eucalyptus kraft pulp," *Carbohydr. Polym.*, vol. 174, pp. 923–932, Oct. 2017.
- [60] Y. Qin, *Micromanufacturing Engineering and Technology*. William Andrew, 2010.
- [61] D. Zhang, J. M. Breguet, R. Clavel, L. Phillippe, I. Utke, and J. Michler, "In situ tensile testing of individual Co nanowires inside a scanning electron microscope," *Nanotechnology*, vol. 20, no. 36, Sep. 2009.
- [62] G. Guillonneau *et al.*, "Nanomechanical testing at high strain rates: New instrumentation for nanoindentation and microcompression," *Mater. Des.*, vol. 148, pp. 39–48, Jun. 2018.
- [63] J. M. Wheeler and J. Michler, "Elevated temperature, nano-mechanical testing in situ in the scanning electron microscope," *Rev. Sci. Instrum.*, vol. 84, no. 4, Apr. 2013.
- [64] A. C. Fischer-Cripps, *The IBIS handbook of nanoindentation*. Fischer-Cripps Laboratories, 2009.
- [65] G. M. Pharr, "An improved technique for determining hardness and elastic modulus using load and displacement sensing indentation experiments," *J. Mater. Res.*, vol. 7,

- no. 6, pp. 1564–1583, 1992.
- [66] M. D. Uchic, D. M. Dimiduk, J. N. Florando, and W. D. Nix, “Sample Dimensions Influence Strength and Crystal Plasticity,” *Science (80-.)*, vol. 305, pp. 986–989, 2004.
- [67] D. S. Gianola and C. Eberl, “Micro- and nanoscale tensile testing of materials,” *JOM*, vol. 61, no. 3, pp. 24–35, 2009.
- [68] M. Smolka *et al.*, “Novel temperature dependent tensile test of freestanding copper thin film structures,” *Review of Scientific Instruments*, vol. 83, no. 6. Jun-2012.
- [69] L. Tian *et al.*, “Approaching the ideal elastic limit of metallic glasses,” *Nat. Commun.*, vol. 3, 2012.
- [70] J. H. Han and M. T. A. Saif, “In situ microtensile stage for electromechanical characterization of nanoscale freestanding films,” *Rev. Sci. Instrum.*, vol. 77, no. 4, 2006.
- [71] K. E. Johanns *et al.*, “In-situ tensile testing of single-crystal molybdenum-alloy fibers with various dislocation densities in a scanning electron microscope,” *J. Mater. Res.*, vol. 27, no. 3, pp. 508–520, Feb. 2012.
- [72] R. Liu, H. Wang, X. Li, G. Ding, and C. Yang, “A micro-tensile method for measuring mechanical properties of MEMS materials,” *J. Micromechanics Microengineering*, vol. 18, no. 6, Jun. 2008.
- [73] D. Casari *et al.*, “A self-aligning microtensile setup: Application to single-crystal GaAs microscale tension-compression asymmetry,” *J. Mater. Res.*, vol. 34, no. 14, pp. 2517–2534, Jul. 2019.
- [74] A. Rudin and P. Choi, *The Elements of Polymer Science & Engineering*. Elsevier, 2013.
- [75] M. Mieszala *et al.*, “Micromechanics of Amorphous Metal/Polymer Hybrid Structures with 3D Cellular Architectures: Size Effects, Buckling Behavior, and Energy Absorption Capability,” *Small*, vol. 13, no. 8, Feb. 2017.
- [76] R. P. Swatloski, S. K. Spear, J. D. Holbrey, and R. D. Rogers, “Dissolution of cellulose with ionic liquids,” *J. Am. Chem. Soc.*, vol. 124, no. 18, pp. 4974–4975, May 2002.
- [77] S. Zhu *et al.*, “Dissolution of cellulose with ionic liquids and its application: A mini-

- review,” *Green Chemistry*, vol. 8, no. 4. pp. 325–327, 2006.
- [78] N. L. Mai, K. Ahn, and Y. M. Koo, “Methods for recovery of ionic liquids - A review,” *Process Biochem.*, vol. 49, pp. 872–881, 2014.
- [79] A. B. Reising, R. J. Moon, and J. P. Youngblood, “EFFECT OF PARTICLE ALIGNMENT ON MECHANICAL PROPERTIES OF NEAT CELLULOSE NANOCRYSTAL FILMS,” *J-FOR J. Sci. Technol. For. Prod. Process.*, vol. 2, no. 6, pp. 32–41, 2012.
- [80] M. K. Hausmann *et al.*, “Dynamics of Cellulose Nanocrystal Alignment during 3D Printing,” *ACS Nano*, vol. 12, no. 7, pp. 6926–6937, Jul. 2018.
- [81] M. Jiang, S. N. Demass, D. R. Economy, T. Shackleton, and C. L. Kitchens, “Formation of highly oriented cellulose nanocrystal films by spin coating film from aqueous suspensions,” *J. Renew. Mater.*, vol. 4, no. 5, pp. 377–387, Oct. 2016.
- [82] Y. Habibi, T. Heim, and R. Douillard, “AC electric field-assisted assembly and alignment of cellulose nanocrystals,” *J. Polym. Sci.*, vol. 46, pp. 1430–1436, 2008.